Polarized Photofission Fragment Angular Distributions of ^{232}Th and ^{238}U

Jeromy Ryan Tompkins

A dissertation submitted to the faculty of the University of North Carolina at Chapel Hill in partial fulfillment of the requirements for the degree of Doctor of Philosophy in the Department of Physics and Astronomy.

Chapel Hill
2012

Approved by:

H. J. Karwowski

M. W. Ahmed

T. B. Clegg

J. Engel

F. Heitsch

ABSTRACT

JEROMY RYAN TOMPKINS: Polarized Photofission Fragment Angular Distributions of ^{232}Th and ^{238}U.
(Under the direction of H. J. Karwowski.)

A study of photofission fragment angular distributions on ^{232}Th and ^{238}U has been completed for the first time using linearly-polarized, quasi-monoenergetic photon beams of near-barrier energies. Large polarization asymmetries are observed in both nuclei. For ^{232}Th, fragments are emitted in the direction of beam polarization with more than fifteen times greater preference than perpendicular to it when the beam energy is 6.2 MeV. These asymmetries are roughly a factor of two times greater than are characteristic of ^{238}U. The large observed fragment asymmetries are responsible for asymmetries in the accompanying prompt-fission neutron angular distributions that have recently been measured [1]. A smooth decrease in the polarization asymmetry has also been observed as beam energies increase from 5.9 MeV to 7.6 MeV. The smooth variations reveal no resonant fission processes in the same energy range.

Contents

List of Tables

List of Figures

List of Abbreviations

ADC	Analog-to-digital converter
BPM	Beam pickoff monitor
CEBAF	Continuous Electron Beam Accelerator Facility
CODA	CEBAF Online Data Acquisition system
CFD	Constant-fraction discriminator
DAQ	Data acquisition system
FAD	Fragment angular distribution
FEL	Free electron laser
HPGe	High-purity germanium
HIγS	High Intensity γ-ray Source
GDR	Giant dipole resonance
GS	Ground state
JLAB	Thomas Jefferson National Accelerator Facility
LD	Liquid drop
LDM	Liquid drop model
LED	Leading-edge discriminator
LTF	Live time fraction
NAD	Neutron angular distribution
PFAD	Photofission fragment angular distribution

SSD	Silicon strip detector
TDC	Time-to-digital converter
TKE	Total kinetic energy
TOF	Time of flight
TUNL	Triangle Universities Nuclear Laboratory
UTR	Upstream target room

Chapter 1

Introduction

1.1 The Importance of Fission

Few people in the world have never heard the word "fission", and for good reason. Fission has shaped the twentieth and twenty-first centuries in ways that no other nuclear reaction has. It has influenced the world both politically and economically. It has ended wars and nearly begun others. In light of this, one might believe that fission is well understood. To say so, is to be partially correct. It is also to sweep under the rug lots of unsolved questions that have attracted the attention of subatomic physicists since the early days of its discovery. Fission is richly complicated. An understanding of observables resulting from fission requires information of both static nuclear properties, large-scale nuclear dynamics, understanding of nuclear configurations in extreme conditions, and the respective strengths of collective and single-particle degrees of freedom [2].

The importance of fission has recently been highlighted by the United States Deparment of Energy [3] because of increased computational power that has made a micro-

scopic description tenable. An improved understanding of fission not only is satisfying from a scientific perspective but also from a practical perspective. It is expected to improve future nuclear reactor designs and understand their performance characteristics; current reactors are operated well below maximum power output because the limits of safe operation are not well established. Such an improved understanding would directly impact the power output of existing reactors and increase their safety.

1.2 The Discovery of Fission

Fission was first observed by E. Fermi and coworkers in 1934 as they were seeking to create transuranic elements by β-decay that follows neutron capture [4, 5]. They observed that following activation by neutrons, radioactive species of 4 half-lives were produced, some of which were not identifiable with elements known at the time. For this reason, they claimed that elements beyond uranium had been discovered. Their results were questioned by many and a series of experiments followed by multiple independent research groups [6]. The culmination of these efforts was the experimental determination by Hahn and Strassman that elements of medium mass, such as Ba, were produced by neutron bombardment of uranium [7]. Otto Hahn was subsequently awarded the Nobel Prize in 1944 for the discovery of fission.

At the time, no mechanism was known in nuclear physics to account for the emission of medium-mass nuclei from a heavy nucleus. Meitner and Frisch predicted that if the nucleus broke into two parts, the Coulombic repulsion between the two would be enough

to release $\approx$ 200 MeV [8]. Frisch was able to detect these high energy fragments with a uranium-lined ionization chamber and a neutron source. This further corroborated the presence of a large scale splitting in the nucleus [9].

Following this striking evidence and other experiments that confirmed this new reaction, the ground work was laid for the understanding of fission in the viewpoint of the liquid drop model by Bohr and Wheeler [10]. The qualitative understanding that these scientists brought about has largely persisted to this day.

1.3 Overview of Contents

In the present work, the fission of ^{238}U and ^{232}Th following the absorption of linearly-polarized photons with energies, E_γ, between 5.7 MeV and 7.6 MeV was investigated. This document will motivate and discuss a measurement of the angular distributions of fission fragments from photon-induced fission reactions.

To provide a context for these studies, fission as a whole will be discussed in Ch. 2. Within this chapter, the general characteristics of fission and the present understanding will be presented. Also, fission induced by photons, photofission, is a subfield of fission research that is most relevant to this work. For this reason, its general features will be explained as well.

A more specific discussion on the angular distributions of fission fragments from photofission will follow in Ch. 3. Two paradigms by which fission fragment angular distributions are understood will be presented. A review of all the measurements of

^{238}U and ^{232}Th photofission fragment angular distributions (PFADs) is included as Ch. 4. Since measurements have focused on a large variety of topics, the discussion has been organized by major physics findings.

A related project seeking to understand prompt-fission neutron angular distributions has provided the ultimate impetus for these studies. Its findings are important to understand the reason the present project has been undertaken. Therefore, a concise description of the experiment and its results are included in Ch. 5. It will be followed by the detailed description of the experimental setup of the PFAD experiment that is the topic of this paper. With knowledge of the experimental setup, the reader will be introduced to the characteristics of the acquired data.

The analysis of the data will be elaborated on in Chs. 6 and 7. The former will detail the processing of the raw data into corrected fragment yields for each detector, whereas the latter will overview the modeling of the effects of the finite experimental geometry and other effects that altered the observed angular distribution of the fragment yields. Calculated results of these models were used together with the corrected fragment yields in a fitting routine to extract the parameters defining the fragment angular distribution, as measured in a point geometry. This too will be discussed in Ch. 7. A discussion of the obtained parameters from the fitting routine and its implications to fission will follow in Ch. 8. Finally, concluding remarks will be provided in Ch. 9.

Chapter 2

Fission Theory

2.1 General Fission Characteristics

Fission is the process by which a single nucleus splits into two nuclei, fragments, spontaneously or as the results of an external impetus. The former is a significant ground-state decay mode in heavier actinides; it is not so in ^{238}U and ^{232}Th. The latter occurs after the formation of an excited compound nucleus by an unspecific excitation mechanism. In either case, the nucleus "decays" into two fragments [10]. The nature of this latter step is quite complicated as it is collective in nature and involves large-scale deformations. During this process, the nucleus deforms to the extent that it ultimately splits. The splitting event is called scission. The nature of the splitting varies from fission event to fission event such that the masses of the fragments are best characterized by a probability distribution, the mass yield curve (see Fig. 2.1). Fission occurring at low excitation energies often is characterized by asymmetric splitting so that the mass yield curve is double peaked. Symmetric mass splitting does occur but is more prevalent when the initial compound nucleus is excited at high energies. An

energy release of up to 200 MeV accompanies each fission event that is largely the result of Coulomb energy release. The released energy is split between the total kinetic energy of the fragments and their internal excitation energies so that the fragments are highly excited following scission. Because they are also neutron rich, relaxation is most efficiently accomplished by the emission of neutrons and subsequently photons. More exotic fission events do occur, such as ternary fission when three particles result rather than two, but the remainder of this document will consider the binary fission process described above.

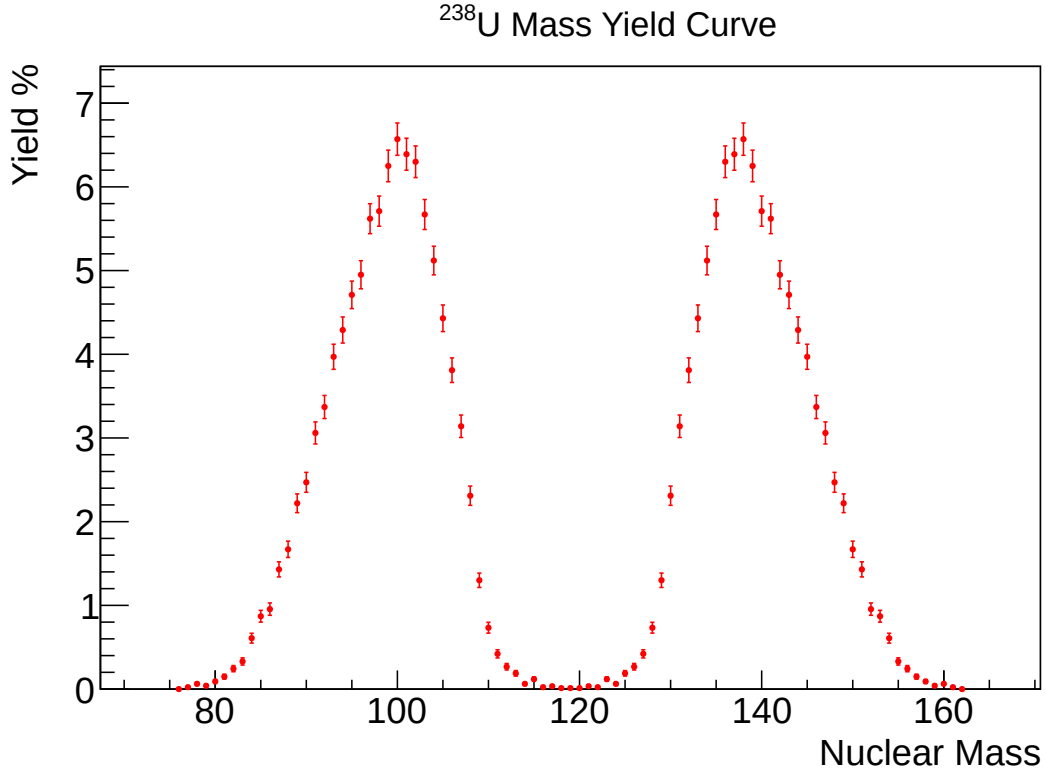

Figure 2.1: The asymmetric mass yield curve for ^{238}U [11]. The preference to fission into two fragments of unequal mass is true of most fissionable nuclei.

2.2 Photofission

Fission is believed to begin with the formation of a compound nucleus, that is, an excited nucleus for which the excitation energy has been shared between all single-particle states in a complex way. A compound nucleus can be produced through a variety of excitation mechanisms, each with its own peculiarities. Particle-bombardment is one such means and tends to produce an initial nucleus with high angular momentum and energy. For this reason, particle-induced fission is useful for studying a regime of fission that is either minimally sensitive to the shell structure of the nucleus or involves high angular momentum. The use of photons, on the other hand, preferentially produces low-spin configurations at all energies. The benefit of a low spin is that the complexity of the reaction is reduced. Extraction of information from the reaction is therefore less complicated and can be potentially understood better. Fission induced by photons, photofission, is therefore a useful method for investigating the low-energy regime, which is the most important for practical applications.

2.2.1 Key Characteristics of Photoabsorption

The interaction of electromagnetic fields, i.e. photons, and matter is considered the most well understood interaction in nuclear physics. Two of its main results are included here. A more detailed derivation is included in Appendix A for completeness. The first is a selection rule. It states that an electromagnetic field of multipolarity l can couple an initial state with angular momenta J_i to a final state with angular momentum

J_f if the triangle rule $|J_i - l| \leq J_f \leq J_i + l$ is satisfied. Further, the associated transition rate, T_{fi}, is given by [12]

$$T_{fi}(l;\Pi) = \frac{8\pi(l+1)}{l[(2l+1)!!]}\frac{k^{2l+1}}{\hbar}|\langle f|\hat{\Omega}_{l\mu}(\Pi)|i\rangle|^2, \tag{2.1}$$

where Π denotes whether the transition is electric or magnetic in nature and the matrix element contains all of the information regarding the nuclear wavefunctions.

With these results, it is possible to understand the benefits of photon absorption as the mechanism for inducing fission in even-even nuclei. Without considering the magnitude of the matrix element, Eq. 2.1 indicates that for a fixed k value, which is proportional to photon energy, the transition rate decreases rapidly as l increases. If this fact is coupled with the selection rules, an even-even nucleus in its ground state $J = 0$ will be excited to states of $J = 1$ or $J = 2$. Continuing to ignore the contribution of the nuclear matrix element, the energy dependence of these rates is weak as elicited by the fact that $k = E_\gamma/197$ MeV fm. As compared to other excitation mechanisms involving the bombardment by particles, the energy and angular momentum dependence of photoabsorption is expected to be relatively simple. Finally, crude approximations can be made of the nuclear wavefunction to evaluate the matrix elements. These Weisskopf estimates [13] predict that the ratio of the electric to the magnetic transition rate of the same multipole is $\approx 0.3A^{-2/3}$. The transitions of highest probability from the 0^+ ground state of an even-even nucleus are to $J^\pi = 1^-$ states.

2.3 Theoretical Overview

Though the ideas presented at the outset of fission research, such as the liquid drop model, are still integral to the manner in which fission is understood today, insights to the process have been provided by new approaches to study the process and the advent of modern computing power. Today, fission is better understood, but there are still fundamental observations, such as the mass yield distribution, that are not universally predictable.

The extent to which fission is understood is made clear by a survey of the theoretical calculations. There are two categories that all calculations fall into: those that treat fission as a dynamical process and those that do not. An excellent example of the static description of fission is the macroscopic-microscopic model that will be presented in Sect. 2.3.1. The original form of this hybrid model was able to predict a more complicated fission barrier structure, and variations of it have proven fruitful in understanding experimental observations. Another static approach uses the statistical model to calculate observables such as mass yields and angular distributions and will be discussed briefly in Sect. 2.3.2. Dynamical calculations require the most detail and will be summarized in section 2.3.3. The following discussion does not attempt to be exhaustive and merely serves to overview the current understanding of fission so the reader can grasp one simple point: fission is only partially understood and requires further theoretical and experimental effort.

2.3.1 Macroscopic-Microscopic Calculations

The first theoretical approach is an extended form of the original fission theory derived by Bohr and Wheeler [10]. It computes the energy of the nucleus for deformed shapes classically and then adds corrections to account for the quantum mechanical nature of the nucleus. This approach was successfully applied to fission first by Strutinsky [14] and its results were largely successful in removing the large discrepancies between the classical treatment and the observations.

The classical description of the nucleus is that of a uniformly-charged liquid drop (LD) with a sharp edge, as was first proposed by Bethe and Weizsacker [15, 16], extended by Meitner and Frisch [8], and then fleshed out by Bohr and Wheeler [10]. In such a description, the energy can be computed for a given nuclear shape which is parameterized by a polynomial expansion,

$$R(\theta, \phi) = \frac{R_0}{\lambda} \sum_{l} \sum_{m=-l}^{l} \beta_{lm} Y_{lm}(\theta, \phi), \tag{2.2}$$

where λ is a scale factor to ensure volume conservation, β_{lm} is the coefficient of the l^{th} multipole in the expansion, and Y_{lm} is a spherical harmonic. The energy of such a LD is made up of three contributing terms referring to the volume E_V, surface tension E_S, and Coulomb energy E_C [17],

$$E_{LDM}(\beta) = E_V + E_S(\beta) + E_C(\beta). \tag{2.3}$$

Since these calculations are concerned with deviations of the shape from a sphere, it is natural to discuss the difference in energy between the deformed nucleus and the spherical nucleus. Since only the E_S and E_C depend on the deformation, they alone contribute to this difference. For small deformations, the shape is sufficiently described by an expansion of the surface up to quadrupole terms and the restoring force F_r is obtained by the derivative of this energy, given as [17]

$$F_r = -\frac{dE}{d\beta_{lm}} = -E_S(0)\left[\frac{1}{4\pi}(l-1)(l+2) - x\frac{5}{\pi}\frac{l-1}{2l+1}\right]\beta_{lm}. \tag{2.4}$$

Here x is the fissility parameter defined as $x = E_C(0)/2E_S(0) \propto Z^2/A$ where $E_S(0)$ indicates the surface energy for zero deformation. The first term is the contribution of the surface energy and the second the Coulomb energy. Note that the surface term contributes a restoring force whereas the Coulomb term is a repulsive force. Equation (2.4) shows that for the case of small quadrupole deformations the force becomes repulsive when $x > 1$, and the LD becomes unstable to quadrupole deformations. The splitting of the drop is then energetically possible.

Further, the potential energy of the LD when plotted in parameter space β_{lm} contains a saddle point, see Fig. 2.2, which is referred to as the fission barrier. The model has been improved in recent years by considering additional terms to the energy [19] and is comparable, if not better than, microscopic calculations. However, such a model does not predict some known features of fission, such as fission isomers.

It is no surprise that the LD model fails to give an exact description of fission,

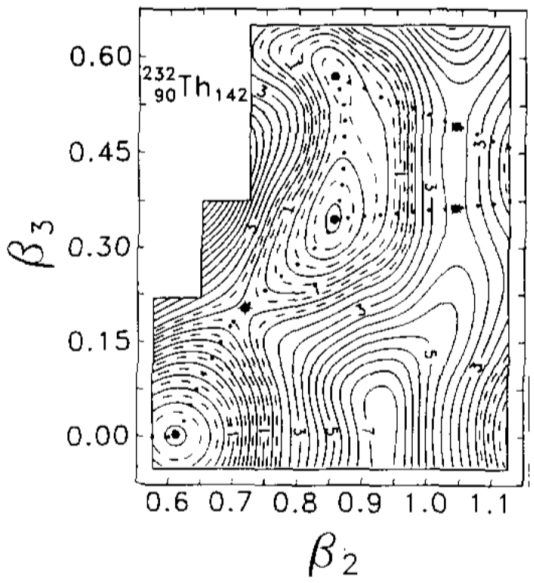

Figure 2.2: The potential energy landscape calculated for ^{232}Th. The potential energy is plotted as a function of the dipole, β_2, and quadrupole, β_3, deformation parameters. Three minima are present. The figure has been taken from Ref. [18].

because it does not account for the quantum nature of the nuclear system. Strutinsky devised a method to correct the liquid drop energies using shell-model calculations [14]. The corrections are computed by considering the energy difference between a system with uniformly distributed levels, such as the LD model, and that of a distribution calculated with a shell model. Since the shell structure varies strongly with deformation [20] and the barrier height is of the order of the energy spacing between major shells, this is a significant effect. Strutinsky's calculations also account for the pairing interaction.

In general, the addition of shell corrections to the LD potential energy produces a double-barrier structure, though sometimes there are multiple barriers predicted. These shift the ground state from a spherical shape to a permanently deformed shape. The multiple minima provide a possible explanation for experimentally observed [21] fission isomers.

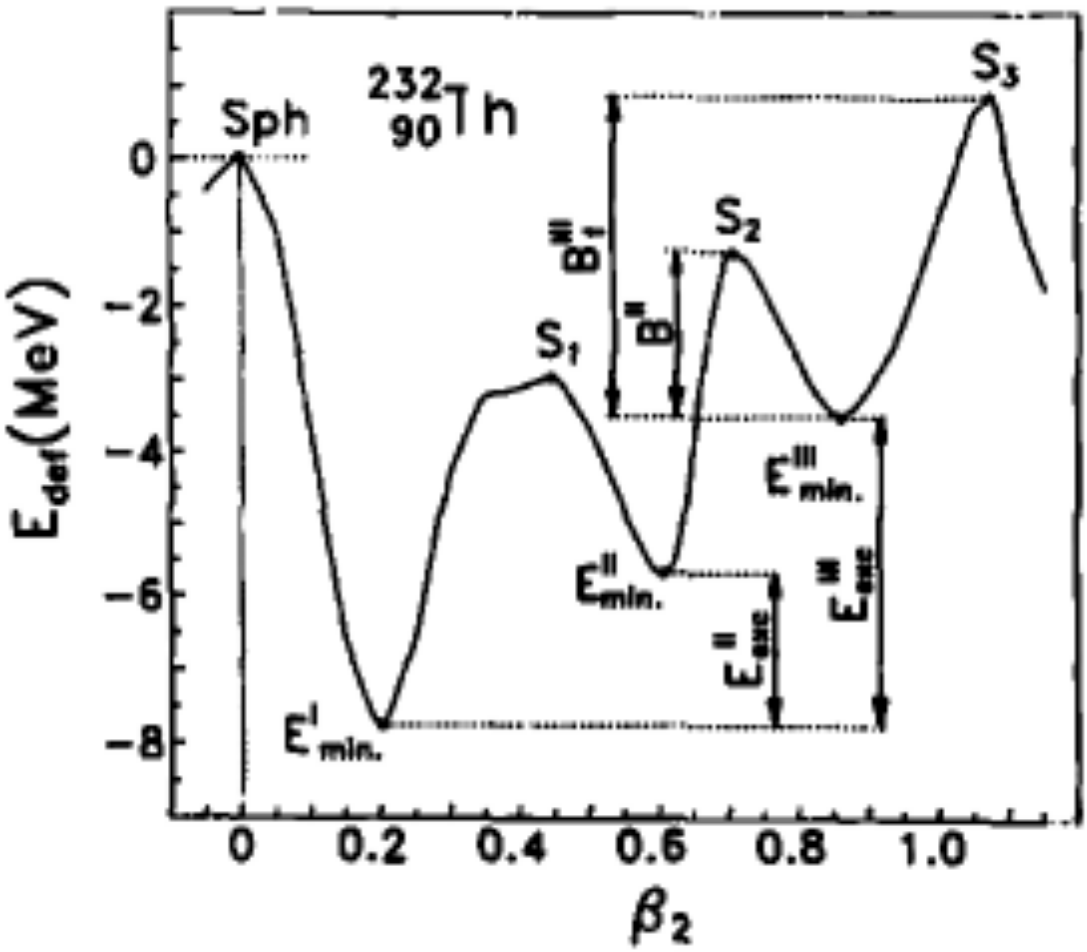

Figure 2.3: A schematic of the a multi-humped potential energy surface. Three saddle points are separated by two potential wells. Each of these has associated with it its own system of energy levels. Figure has been taken from Ref. [18].

2.3.2 Statistical Fission Calculations

The benefit of the dynamical fission calculations is their ability to calculate observables such as the mass distribution. The source of their power is the detail to which they treat the fission process. However, the detail comes at a cost. They rely upon knowledge of the transport parameters such as the inertial mass and friction tensors,

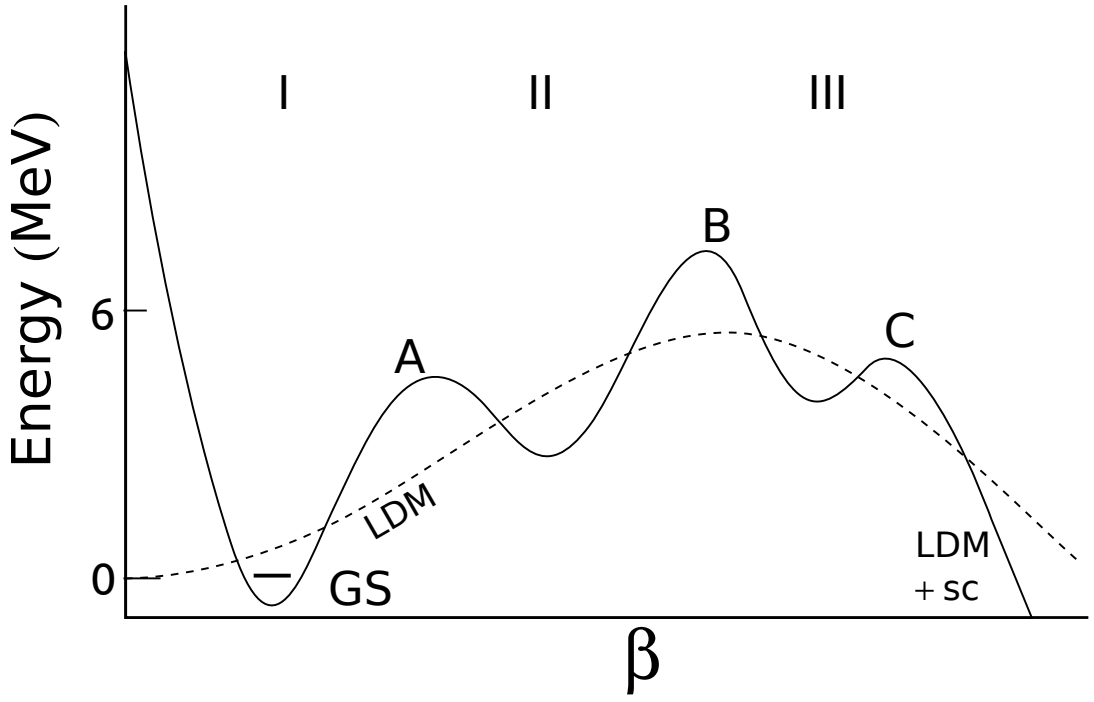

Figure 2.4: A schematic view of a triple-humped fission barrier. Three potential wells exist labeled I, II, and III that are separated from each other by three saddle points A, B, and C. The first well contains the true ground state GS. The potential energy calculated in the liquid drop model is drawn as a dashed curve. The solid curve is the barrier predicted by a macroscopic-microscopic calculation. It includes shell-model corrections to the liquid drop energy and is labeled LDM+sc. Since multiple deformation parameters describe the nuclear shape, often 5, the potential energy is a hypersurface. The above is representative of the potential energy along a "valley" in the hypersurface. The abscissa β represents the set of deformation parameters at any point along the fission path depicted.

that are model dependent. For this reason, an alternative means for computing the same observables is useful. These exist and are based on the treatment of the fission process statistically. A statistical treatment requires that the process depends only on level densities that are independent of time and also a well-defined nuclear temperature. In practice this has been considered at both the saddle point and the scission point. A detailed review of the variations of this approach and their results can be found in

Ref. [17] and will not be repeated here.

2.3.3 Fission Dynamics

Two general approaches to compute fission dynamics have been followed. The distinguishing assumptions of each are such that they apply to conditions that are orthogonal to each other. As a result, there is no potential for calculating the same observable reliably with both approaches. However, they both make the assumption that the shape of the nucleus can be parameterized when it transitions continuously from the initial compound nucleus into fission fragments. Interestingly, it has been pointed out that no conclusive evidence to support this exists in spectroscopic data [17]. Regardless of the accuracy of this approximation, the concept of continuous transitions between highly-deformed shapes is useful. Often the descent from saddle to scission is the subject of these calculations because it is expected to be the most important for determining quantities such as the sharing of the partition of the energy between kinetic and internal excitation and mass yields.

The first general approach treats the process adiabatically. It therefore assumes that such an extreme transition in the nucleus occurs in a manner that allows the nucleus to remain in the configuration defined by the lowest energy single particle levels. The energy of the system is, therefore, carried solely by the shape degrees of freedom. In fission calculations, this approximation is equivalent to the absence of frictional damping during deformation. The second general approach treats an alternative extreme. It assumes that the energies involved in the fission event are high enough that the process

can be treated in a classical sense.

The second approach is not well suited for calculating observables of low-energy fission for reasons that are obvious. However, the alternative is not a clear improvement. The accuracy of its description of the process from saddle to scission has been discussed by Fong [22]. In a concise argument he estimates that the energy spacing to the first single particle states must be greater than 8.4 MeV. Since at normal deformations the energy spacings are typically less than 1 MeV, this condition is not satisfied at the point of scission. An argument by Kadmensky is contrary [23]. He claims that if the transition is not adiabatic, then significant heating of the fissioning system will occur. Any anisotropy in the angular distribution characterizing the fragments will then be destroyed due to statistical mixing of angular momentum states. However, anisotropies have been measured repeatedly so that the adiabatic approximation must be valid [23].

As initially mentioned at beginning of this section, the understanding of fission has improved significantly since its discovery. The fact that calculations exist capable of reproducing many observables is remarkable. However, the validity of many approaches are questionable and many results are limited in scope. There is need for improvement.

Chapter 3

Fission Fragment Angular Distributions

One of the important subjects of photofission studies has been the fragment angular distributions, $W(\theta)$, that are associated with even-even nuclei. Anisotropies in the photofission of ^{232}Th were discovered by Winhold, Demos, and Halpern [24] in 1952. They were able to fit the angular distribution with the function

$$W(\theta) = a + b\sin^2\theta \tag{3.1}$$

and coefficients $b/a = 0.41 \pm 0.05$. The experiment was motivated by the Goldhaber-Teller model [25] that had then recently been formed to explain the giant dipole resonance (GDR). They believed that if the photon could induce an oscillation of the protons and neutrons in the nucleus, then the same excitation could lead to fission. If that occurred, the fragments would be preferentially emitted in the direction of the oscillation, which would be perpendicular to the beam at $\theta = 90°$. However, they were

puzzled to learn that the anisotropy disappeared as the photon energy was increased to energies of the GDR region, E_γ = 10 - 20 MeV. It was obvious then that the origin of the anisotropy was different than that of the GDR. It was not until 1956 that A. Bohr [26] presented a satisfactory explanation for their results.

Bohr's explanation has remained at the heart of the present understanding of fission fragment angular distributions (FADs), though it was extended to include fission induced by polarized photons. On the other hand, recent insights and a new approach to understanding the FADs, hereafter referred to as the Kadmensky approach, has been derived by Kadmensky and collaborators [27]. The form of the angular distribution derived by each of these models is nearly identical but the steps and assumptions employed to arrive at the result are sufficiently different to warrant separate discussions. The channel formalism based on Bohr's ideas in Sect. 3.1 will be followed by that of Kadmensky in Sect. 3.2. Both of these concern the angular distribution that might arise from a single transition state. Because a fission path typically involves the transition through at least two saddle points, some comments on the effect of multiple saddles to the presented theories will be given in Sect. 3.4. For completeness, an account of the previous measurements for photofission FADs (PFADs) will follow in Chapter 4.

3.1 The Bohr Channel Formalism

In the following, the extended channel formalism will be presented, which accounts for beams with a fractional linear polarization P_γ. It will be shown that the fragment

angular distribution, $W(\theta, \phi)$, can be described by

$$W(\theta, \phi) = a + b\sin^2\theta + c\sin^2 2\theta + \omega P_\gamma \left[d\sin^2\theta + c\sin^2 2\theta\right] \tag{3.2}$$

if dipole and quadrupole absorption are considered. In Eq. 3.2, the ω is +1(-1) for transitions that are electric(magnetic) in nature. It is important to understand that the formalism ignores the dynamics of the fission process prior to the saddle point except to assume that it is adiabatic.

Two crucial assumptions are made in the treatment. The first is that the transition states of the fissioning nucleus correspond to collective rotations, and the second is that the associated nuclear shape is axially symmetric. Given these, the wavefunction should be the same as that of the symmetric top, otherwise known as the symmetric rotor. The Hamiltonian for the symmetric rotor, in a purely collective model, is

$$\hat{H} = \frac{\hat{\mathbf{J}}'^2 - \hat{\mathbf{J}}'^2_z}{2\Omega}, \tag{3.3}$$

where the primed operators are the body-fixed angular momentum operators and Ω is the moment of inertia for rotations about the symmetry axis. Such a Hamiltonian is diagonalized by wavefunctions of the form

$$\phi^J_{MK}(\boldsymbol{\omega}) = \mathcal{D}^J_{MK}(\boldsymbol{\omega}), \tag{3.4}$$

where the $\mathcal{D}^J_{MK}(\boldsymbol{\omega})$ are rotation matrix elements corresponding to rotations about the

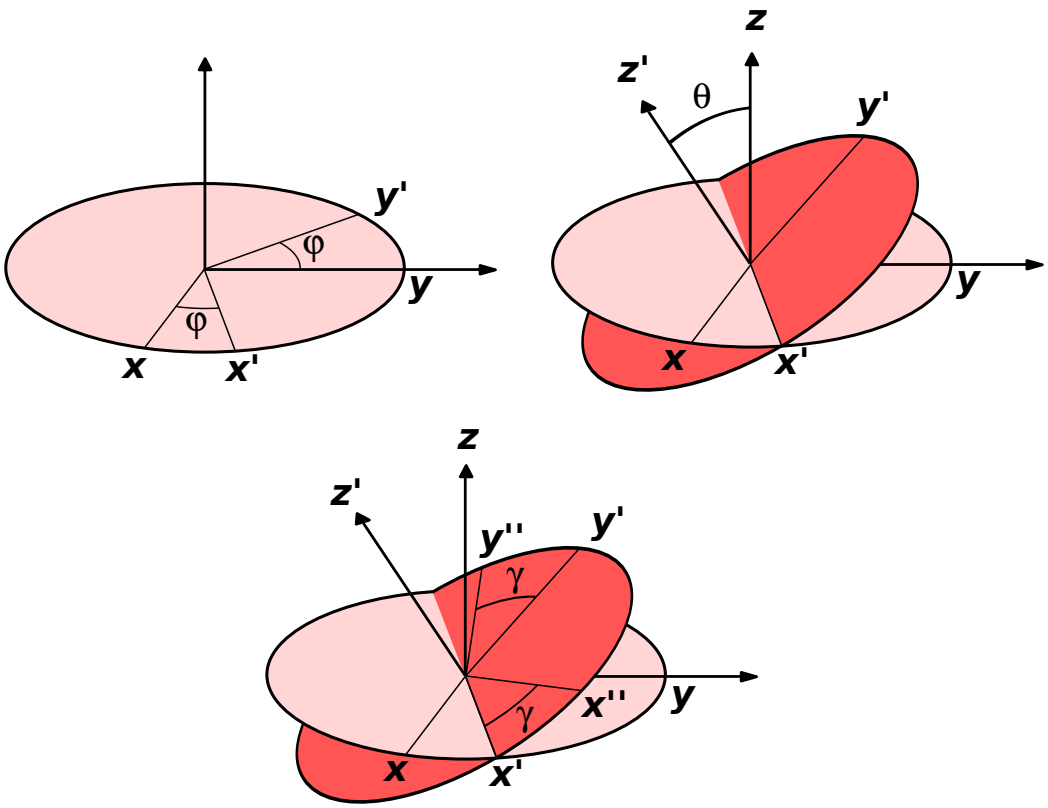

Figure 3.1: Diagram of the Euler angles that define the orientation of a body in three-dimensional space. The rotations are ordered as illustrated by proceeding clockwise from the top left. For an axially-symmetric nucleus, the first two rotations ϕ and θ define the orientation of the symmetry axis with respect to the laboratory frame.

three Euler angles $\boldsymbol{\omega} = (\phi, \theta, \gamma)$, see Fig. 3.1. These states are specified entirely by the three angular momentum quantum numbers J, K, and M and are, respectively, the total angular momentum and its projections onto the nuclear symmetry axis and the beam axis, see Fig. 3.2. It is possible to write Eq. 3.4 in a more explicit manner as

$$\phi^J_{MK}(\boldsymbol{\omega}) = e^{-iK\phi} d^J_{MK}(\theta) e^{-iM\gamma}, \tag{3.5}$$

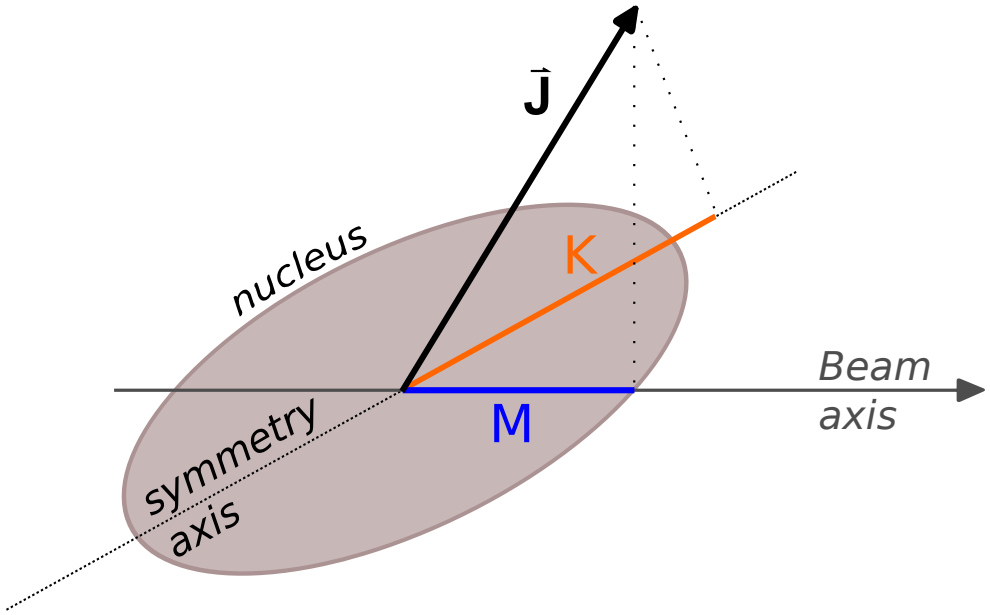

Figure 3.2: The J, K, and M quantum numbers that define the orientation of the body-fixed coordinate system of the axially-symmetric nucleus with respect to the laboratory coordinate system. This definition fixes the nuclear symmetry axis to the z-axis of the body-fixed frame and the beam axis to the z-axis of the laboratory.

where the $d^J_{M,K}$ functions are the Wigner rotational d-functions. The lowest order forms of these functions are listed in Section B.1. Their explicit form is [28]

$$\begin{aligned} d^J_{M,K}(\theta) =& \sqrt{(J+M)!(J-M)!(J+K)!(J-K)!} \\ & \times \sum_{M'} \frac{(-1)^{M'}[\sin(\theta/2)]^{2M'-M+K}[\cos(\theta/2)]^{2J-K+M-2M'}}{(J-K-M')!(J+M-M')!(M'+K-M)!(M')!}, \end{aligned} \tag{3.6}$$

where the summation is over all M' for which the terms in the denominator are greater than or equal to zero. If one further assumes that the transition of the system from saddle to scission is characterized by the separation of the fragments along the nuclear

symmetry axis and that the orientation of this axis is fixed in space, i.e., K is conserved, then the angular distribution for unpolarized photons should be simply the square of these matrix elements,

$$W^J_{MK}(\theta) \propto |d^J_{MK}(\theta)|^2. \tag{3.7}$$

The present experiment is unable to distinguish the helicity of the photon that caused the fission event. For this reason, the $M = \pm 1$ states are summed over to create a channel distribution dependent on J and K only,

$$W^J_K(\theta, \phi) = \frac{2J+1}{2}\left(\frac{1}{2}\left[|d^J_{1,K}(\theta)|^2 + |d^J_{-1,K}(\theta)|^2\right]\right). \tag{3.8}$$

If the photon beam is polarized to a fractional value, P_γ, the rotational symmetry about the beam axis is broken. The similar expression for Eq. 3.8 when polarization is present is [29]

$$W^J_K(\theta, \phi) = \frac{2J+1}{2}\left(\frac{1}{2}\left[|d^J_{1,K}(\theta)|^2 + |d^J_{-1,K}(\theta)|^2\right] - \omega P_\gamma \cos 2\phi d^J_{1,K}(\theta) d^J_{-1,K}(\theta)\right). \tag{3.9}$$

The value of ω is determined by the polarity of the absorption process, and its value is +1 or -1 when the process is electric (E1 and E2) or magnetic (M1) in character, respectively. A discrepancy exists between the angular distribution derived from Eq. 3.9, as it was originally published in Ref. [29], and that presented in Ref. [30]. The discrepancy can be associated with the sign preceding ω, where the results of Ref. [30] require the sign to be negative. The present work is based on the angular distribution presented

in Ref. [30].

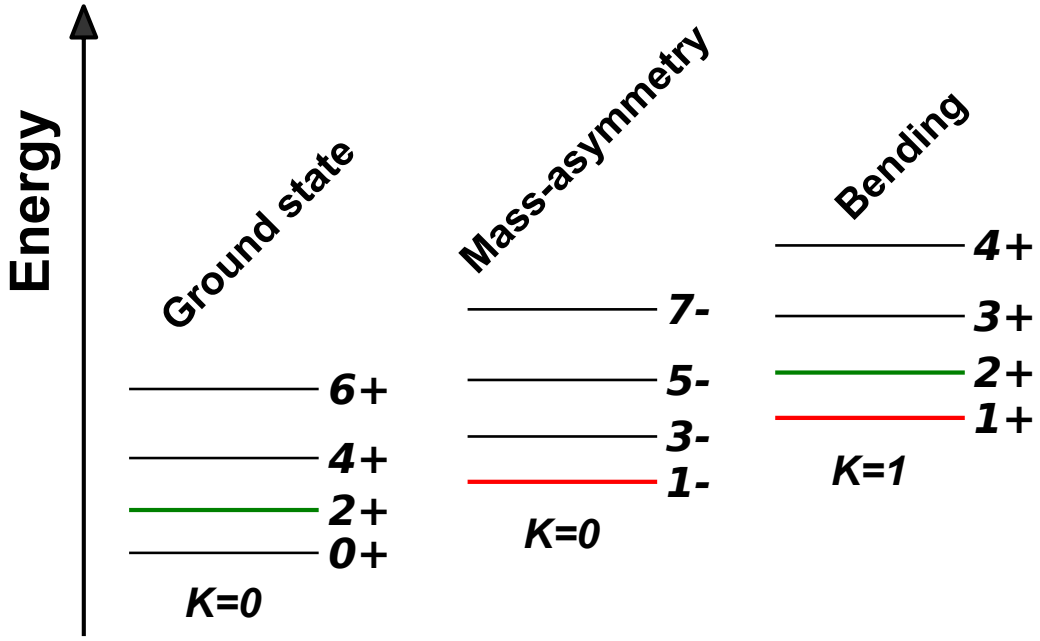

Figure 3.3: A schematic level scheme of a heavy nucleus as presented in Ref. [30]. States that are expected to contribute to dipole fission are colored red and those for quadrupole fission green.

The measured angular distribution is generated by the linear combination of these channel angular distributions. Recall that in Sect. 2.2.1 it was demonstrated that the absorption of a photon will excite an even-even nucleus in the ground state primarily to states of $J^\pi = 1^-$ and occasionally to $J^\pi = 1^+$ or 2^+, if the nuclear wavefunction does not bias the probability toward other states. Bohr argued that the excitation spectrum of the fissioning nucleus would be similar to the states in the first potential well despite the fact that the nucleus at the transition state should be sufficiently different. These are characterized by rotational and vibrational bands with different

K values and parities, see Fig. 3.3. If this assumption is correct, the minimum energy level at the saddle point would likely be a 0^+ state followed by a 2^+ state in the same rotational band with $K = 0$. The next state would then be the 1^- state of a $K = 0$ band with negative parity. If the fissioning nucleus has an excitation spectrum of this form, then the nucleus will preferentially absorb the photon through E1, M1, and E2 transitions. The measured angular distribution would then be reasonably well modeled by the combined channel distributions of all dipole and quadrupole terms.

J	K	Channel Coeff	$W_K^J(\theta)$
1	0	x	$\frac{3}{4}\sin^2\theta + \frac{3}{4}\omega P_\gamma \cos 2\phi \sin^2\theta$
1	± 1	y	$\frac{3}{4}\left(1 - \frac{1}{2}\sin^2\theta\right) - \frac{3}{8}\omega P_\gamma \cos 2\phi \sin^2\theta$
2	0	u	$\frac{15}{16}\sin^2 2\theta + \frac{15}{16}\omega P_\gamma \cos 2\phi \sin^2 2\theta$
2	± 1	v	$\frac{5}{8}\left(2 - \sin^2\theta - \sin^2 2\theta\right) + \frac{5}{8}\omega P_\gamma \cos 2\phi \left(\sin^2\theta - \sin^2 2\theta\right)$
2	± 2	w	$\frac{5}{8}\left(\sin^2\theta + \frac{1}{4}\sin^2 2\theta\right) - \frac{5}{8}\omega P_\gamma \cos 2\phi \left(\sin^2\theta - \frac{1}{4}\sin^2 2\theta\right)$

Table 3.1: The angular distributions of specific fission channels derived from Eq. 3.9. It is implied that $M = \pm 1$ has been averaged over.

The channel wave functions for the contributing dipole and quadrupole terms are listed in Table 3.1. If one includes all dipole and quadrupole channels and then collects like terms, the total angular distribution becomes [29, 30]

$$W(\theta, \phi) = a + b\sin^2\theta + c\sin^2 2\theta + \omega P_\gamma \left[d\sin^2\theta + c\sin^2 2\theta\right]). \tag{3.10}$$

The a, b, c, and d coefficients result from the relative contributions of fission channels to the angular distribution. Using the convention of Ref. [30], the dipole channel strengths are labeled x and y for the $(J = 1, K = 0)$ and $(J = 1, K = \pm 1)$, respectively, and the quadrupole channel strengths are labeled u, v, and w for $(J = 2, K = \pm 1)$, $(J = 2, K =$

± 1), and ($J = 2, K = \pm 2$). The a, b, c, and d coefficients can be decomposed into these channels clearly by defining a matrix A that combines the channel contributions $\boldsymbol{\zeta} = (x, y, u, v, w)$ into the angular distribution parameters $\mathbf{p} = (a, b, c, d)$ by $\mathbf{p} = A\boldsymbol{\zeta}$. The conversion matrix is

$$A = \begin{pmatrix} 0 & 3/2 & 0 & 5/2 & 0 \\ 3/4 & -3/4 & 0 & -5/4 & 5/4 \\ 0 & 0 & 15/16 & -5/4 & 5/16 \\ -3/4 & 3/4 & 0 & -5/4 & 5/4 \end{pmatrix}. \tag{3.11}$$

In the literature, there is little agreement as to the proper way to represent the angular distribution. Equation 3.10 is the convention chosen for the present work because of the consistency of the c terms. Another common form for the polarized angular distribution is presented by Ratzek and collaborators [30] as

$$W(\theta, \phi) = a + b \sin^2\theta + c \sin^2 2\theta + \omega P_\gamma \cos 2\phi \left[d \sin^2\theta - 4c \sin^4\theta \right]. \tag{3.12}$$

Their preferred form of the angular distribution differs from Eq. 3.10 by the definition of d. One can convert from Eq. 3.10 to Eq. 3.12 by defining the d parameter of Eq. 3.12 in terms of the coefficients of Eq. 3.11 such that $d_{Ratzek} \rightarrow d + 4c$.

3.2 The Kadmensky Fragment Angular Distribution

The approach of Kadmensky and collaborators, developed in a series of papers [23, 27, 31, 32], is based on similar concepts to Bohr's theory but addresses the uncertainty between orbital angular momentum and orientation. Bohr assumed that the axis of symmetry entirely defines the angle at which the fragments run away from each other. However, complete knowledge of the fragment orientation requires ignorance of the relative orbital angular momentum. Ignorance implies that values of l approaching infinity contribute to the wave function, which cannot be realized.

Kadmensky begins his investigation of PFADs assuming that fission is adiabatic and further that it involves an axially-symmetric nucleus splitting into two axially symmetric fragments. In order for the fission process to be adiabatic, four conditions must be satisfied [31]. The first is that the transition from saddle to scission must be much shorter than the rotational period of the nucleus. This establishes that the orientation of the symmetry axis remains fixed in space between a transition state and scission. Second, the rotation energy of the proto-fragments must be much less than the kinetic energy of their relative motion. Thirdly, the detection system should be incapable of fixing or distinguishing the total angular momenta of the fragments. Finally, the centrifugal potential must always be less than the kinetic energy of the fragments.

The coupling of fission fragments to good angular momentum is carried out in the

channel approach. The total orbital angular momenta of each fission fragment, J_i, are coupled together to a channel spin, I, which is subsequently coupled to their relative orbital angular momentum, l. The set of quantum numbers that characterizes this channel coupling is denoted by $cIl = \sigma_1 J_1 \sigma_2 J_2 Il$, where other quantum numbers not explicitly accounted for are included as σ. It can be derived from quantum mechanical principles that the angular distribution of these two particles is given by [31]

$$W(\theta,\phi) = \frac{1}{\Gamma^J_{\sigma c}} \sum_M S(M) \sum_{I=|J_1-J_2|}^{J_1+J_2} \sum_{M_I} \left| \sum_{lm_l} C^{JM}_{IlM_I m_l} Y_{lm_l}(\theta,\phi) e^{i\bar{\delta}_{cl}} \sqrt{\Gamma^J_{\sigma cIl}} \right|^2 , \qquad (3.13)$$

where $S(M)$ is a normalized distribution function for M; $\Gamma^J_{\sigma c}$ is the partial width for fission resulting in the channel defined by J and the quantum numbers σc; $C^{JM}_{IlM_I m_l}$ is a Clebsch-Gordan coefficient; $Y_{lm_l}(\theta,\phi)$ is a spherical harmonic; and $\Gamma^J_{\sigma cIl}$ is the partial width for the channel defined by the listed quantum numbers. The angular distribution is then intrinsically dependent upon the partial widths. Evaluation of these partial widths involves the computation of the matrix elements of the interaction between the initial transition state wave function and the wave function of the fragments when their relative distance is large. It is at this point that the concept of the uncertainty principle is introduced to the derivation.

The calculation of these partial widths involves integrations over the sets of Euler angles defining the orientation of the individual fragments in the laboratory frame, the orientation of the parent-nucleus axis in the laboratory frame, and the relative orientation of the fragment symmetry axes to each other. It is found that the partial

width is maximal when the fragment symmetry axes are aligned with the symmetry axis of the parent nucleus. Deviations from this alignment decrease the value of the partial width rapidly enough that calculation can be well approximated by multiplying the result for the case that they are completely aligned by a "smeared" delta function, F_{l_m}. This is a reflection of the uncertainty principle between the squared orbital angular momentum operator and the position operator [32]. It is naturally expressed in the form

$$F_{l_m}(\theta') = b(l_m) \sum_{l=0}^{l_m} Y_{l0}(\cos\theta')\Pi_l, \tag{3.14}$$

where l_m is the maximum relative orbital angular momentum between the two fragments, θ' denotes the relative angle between the two fragment axes, $b(l_m)$ is a normalization factor, and $\Pi_l = 1 + \pi\pi_1\pi_2(-1)^l$. Here π is the parity of the parent nucleus, and π_1 and π_2 are the parities of the fission fragments. This result is integral to Kadmensky's approach.

The differential cross section for axially-symmetric nuclei can be expressed as [27]

$$\frac{d\sigma_f}{d\Omega}(\theta,\phi) = \sum_{JK} P(JK) T_{JK}(\theta,\phi), \tag{3.15}$$

where

$$P(JK) = \frac{\Gamma_f(JK)}{\Gamma(J)} \sigma_\gamma(EJ) \tag{3.16}$$

are factors that weight the channel angular distributions T_{JK}. These are expressed as

$$T_{JK}(\theta,\phi) = \frac{2J+1}{16\pi^2}\int d\omega \sum_{M=\pm1}\frac{1}{2}\Big\{\left|\mathcal{D}^{J}_{MK}(\omega)\right|^2 + \left|\mathcal{D}^{J}_{M-K}(\omega)\right|^2 \\ -P_\gamma\left[\mathcal{D}^{J*}_{MK}(\omega)\mathcal{D}^{J*}_{-MK}(\omega) + \mathcal{D}^{J*}_{M-K}(\omega)\mathcal{D}^{J*}_{-M-K}(\omega)\right]\Big\} F^2_{l_m}(\theta'). \tag{3.17}$$

The above equation is simplified through significant algebraic manipulation relying the properties of the rotational matrix elements. It ultimately becomes

$$T_{JK}(\theta,\phi) = \sum_L B_{JKL}Y_{L0}(\Omega) + P_\gamma\sum_L D_{JKL}(Y_{L2}(\Omega) + Y_{L-2}(\Omega)). \tag{3.18}$$

The B_{JKL} values are defined to be

$$B_{JKL} = \frac{2J+1}{16\pi}\left|b(l_m)\right|^2 \\ \times\sum_{l=0}^{l_m}\sum_{l'=0}^{l_m} C^{L0}_{JJ1-1}C^{L0}_{JJK-K}\left(C^{L0}_{ll'00}\right)^2\frac{(-1)^{1+K}(2l+1)(2l'+1)}{(2L+1)\sqrt{4\pi(2L+1)}}(1+(-1)^L)\Pi_l\Pi_{l'}, \tag{3.19}$$

and D_{JKL} is

$$D_{JKL} = \frac{2J+1}{16\pi}|b(l_m)|^2 \\ \times\sum_{l=0}^{l_m}\sum_{l'=0}^{l_m} C^{L2}_{JJ11}C^{L0}_{JJK-K}\left(C^{L0}_{ll'00}\right)^2\frac{(-1)^{1+K}(2l+1)(2l'+1)}{(2L+1)\sqrt{4\pi(2L+1)}}(1+(-1)^L)\Pi_l\Pi_{l'}. \tag{3.20}$$

One can reduce Eq. 3.18 to an angular distribution of the form Eq. 3.10 by collecting like terms.

The uniqueness of this result lies in the B_{JKL} and D_{JKL} values. These are implicitly dependent upon the value of l_m and lead to deviations from Bohr's result when l_m is not allowed to become exceedingly large. The a, b, c, and d parameters are also able to be expressed as

$$a = \sum_{JK} \alpha_{JK} P(JK) \quad b = \sum_{JK} \beta_{JK} P(JK)$$
$$c = \sum_{JK} \gamma_{JK} P(JK) \quad d = \sum_{JK} \delta_{JK} P(JK)$$

The $P(JK)$ functions have already been defined in Eq. 3.16 and are analogous to the x, y, u, v, and w channel coefficients. The coefficients α, β, γ, and δ define the conversion to the a, b, c, and d parameters of Eq. 3.10. They are expressed as

$$\alpha_{JK} = \frac{2\pi}{\sqrt{4\pi}} \left(B_{JK0} + \sqrt{5} B_{JK2} + 3 B_{JK4} \right) \tag{3.21}$$
$$\beta_{JK} = \frac{2\pi}{\sqrt{4\pi}} \left(-\frac{3\sqrt{5}}{2} B_{JK2} - \frac{15}{8} B_{JK4} \right) \tag{3.22}$$
$$\gamma_{JK} = -\frac{105}{32} \frac{2\pi}{\sqrt{4\pi}} B_{JK4} \tag{3.23}$$
$$\delta_{JK} = \frac{2\pi}{\sqrt{4\pi}} \sqrt{\frac{5}{2}} \left(\sqrt{3} D_{JK2} + 18 D_{JK4} \right) \tag{3.24}$$

Interestingly, the exact channel decomposition as Eq. 3.11 is reproduced if l is allowed to go to infinity. If instead, the cutoff is chosen to be $l_m = 30$, as is consistent with the

conclusions of Ref. [32], then the conversion will become

$$A = \begin{pmatrix} 0.024 & 0.74 & 0.06 & 1.2 & 0.03 \\ 0.714 & -0.357 & -0.022 & -0.58 & 0.592 \\ 0 & 0 & 0.854 & -0.569 & 0.142 \\ 0.714 & -0.357 & 3.43 & -1.69 & -0.023 \end{pmatrix}. \tag{3.25}$$

3.3 Comparison of Approaches

The two approaches presented in Sections 3.1 and 3.2 differ only by the presence, or lack, of constraints placed on the relative orbital angular momentum of fission fragments. If no constraint is provided, the results are equivalent. Otherwise, small differences could arise that would lead to discrepancies in extracted channel coefficients for the same measured a, b, c, and d parameters. The degree to which an interpretation based on the Bohr approach would differ from the Kadmensky approach is dependent upon the l_m value. Intuition would suggest that the limitation of orbital angular momentum is a better representation of the physical reality. Unfortunately, the smaller this value is, the more the deduced channel contributions differ. An estimate for the value of l_m has been provided by Kadmensky and Rodionova [32]. They argued that its value should be $20 < l_m < 40$ based on the data of Ref. [33]. As such they conclude that deviations from the Bohr result should be modest.

Based on these considerations, the experimenter is thus forced to interpret data based on some assumption regarding the extent to which fragment axes are aligned.

Fortunately, the deviations from the Bohr results are not large if $l_m > 20$ [32].

3.4 Effect of a Multiple-Humped Fission Barrier

All previous discussion in this chapter has assumed the existence of a transition state associated with a single saddle point. However, it is well established that more than one barrier exists in actinide nuclei [34] as discussed in Chapter 2. The multiplicity of these introduces additional complexity to the interpration of the PFADs, because the influence of each local maximum and minimum through which the fissioning nucleus evolves must be considered. Ultimately, the varied potential energy creates a complicated system of states through which fission can proceed such that resonances and other interesting energy dependencies are potentially observable [34, 35]. As a corrolary to this, there is little reason to suspect that the characteristics of the angular distribution would trend smoothly with increasing photon energy if the energy width of the photon beam is narrow, such as in this work. The evidence and some explanations offered will be discussed in Sect. 4.5.

Chapter 4

Previous Measurements of Photofission Fragment Angular Distributions

Many experiments have been undertaken to measure photofission fragment angular distributions in the past 70 years. These have focused mostly on actinide nuclei and have included those with even neutron and proton numbers as well as odd masses. The following will concern the subset of these measurements related to ^{232}Th and ^{238}U. Within this collection of independent measurements, the characteristics of the photon sources and detection methods varied. The implications of the various photon beam characteristics on the measurements will be discussed in Sect. 4.1. Though the intricacies of each measurement are informative, they will not be detailed since this work does not aim to evaluate the existing data. Instead, the results of each data set are given equal credibility and no position is taken on whether one is superior or inferior

to the others. A table has been included, see Table 4.1, that lists the measurements to be discussed and some of their distinguishing characteristics.

The major findings of this body of measurements will be explored in a topical manner beginning with Sect. 4.2 where the impact that these results have on the understanding of dipole fission will be presented. This is followed up by the findings related to quadrupole fission in Sect. 4.4. Both of these sections focus on the trends specific to their topic. However, since their results are both intimately connected with and shed light on the systematics of the fission barrier, Sect. 4.5 is devoted to explicating their combined impact. Finally, a motivator of this project was to understand the results of recent measurements of the prompt fission neutron angular distributions. These measurements will be presented in Sect. 4.6.

4.1 Implications of Photon Beam Characteristics on Results

One essential component of all the photofission measurements that will be discussed is the photon beam. A handful of techniques have been used to produce a beam with ≈6 MeV, and the measurements of ^{232}Th and ^{238}U have employed many of them. Two major distinguishing factors of the utilized beams have been the energy distribution of the photons, whether monoenergetic or not, and the degree of linear polarization. The majority of these experiments relied on bremsstrahlung beams to induce fission and have reported data as a function of the endpoint energy, E_{max}. Because bremsstrahlung is

Reference	Target	Energy (MeV)	Photon Source	Polarization (%)
Winhold *et al.* [24, 36]	^{232}Th, ^{238}U	6.5 - 14.0	Brem	0
Baz *et al.* [37]	^{238}U	6.5 - 26.5	Brem	0
Katz *et al.* [38]	^{232}Th, ^{238}U	6.5 -	Brem	0
Baerg *et al.* [39]	^{232}Th, ^{238}U	6.0 - 20.0	Brem	0
Forkman *et al.* [40]	^{238}U	10.0 - 20.0	Brem	0
	^{238}U	6.1 - 6.7	(n,γ)	0
Carvalho *et al.* [41]	^{238}U	6.9 - 20.0	Brem	0
Soldatov *et al.* [42]	^{238}U	5.2 - 9.2	Brem	0
Rabotnov *et al.* [43]	^{232}Th, ^{238}U	5.0 - 10.0	Brem	0
Manfredini *et al.* [44]	^{238}U	5.6 - 9.0	(n,γ)	0
Dowdy *et al.* [45]	^{238}U	5.6 - 9.0	(n,γ)	0
Nair *et al.* [46]	^{232}Th, ^{238}U	5.7 - 7.1	Brem	0
Lindgren *et al.* [47]	^{238}U	5.2 - 6.4	Brem	0
Ratzek *et al.* [30]	^{232}Th	10.0 - 12.0	Off-axis Brem	20 - 30
Rudnikov *et al.* [48]	^{238}U	6.5 - 10.3	Brem	0
Steiper *et al.* [49]	^{232}Th	9.0 - 12.0	Off-axis Brem	30
Khvastunov *et al.* [50]	^{232}Th	18.0	e^- - Si crystal	≈80
Khvastunov *et al.* [51]	^{238}U	15.5 - 20.25	e^- - Si crystal	≈80

Table 4.1: The previous measurements to date for the study of PFADs from ^{238}U and ^{232}Th.

characterized by a continuum of photons from $0 < E_\gamma < E_{max}$, a single beam can induce excitations at any photon energy below E_{max}. As a result, multiple fission channels contribute to the final angular distribution, which makes interpretation of results with the model of Sect. 3.1 more difficult. Some, however, have employed monoenergetic beams that are less subject to this difficulty. Care is taken to state that they are less subject, rather than exempt, because the problem persists, albeit in a more localized sense, if nuclear level spacing is less than the energy spread of the photon beam. At energies closer to the barrier height, the number of levels that actually contribute is believed to be small and the bremsstrahlung and monoenergetic data should agree. There have been very few measurements to date of PFADs using monoenergetic photon

sources. In fact, no measurements of ^{232}Th have been carried out prior to the work presented in this thesis.

The fractional polarization of the beam is also an important defining characteristic. With the exception of four, all experiments have used unpolarized photons. Of the four measurements that do employ polarized beams, two are polarized to less than 30% and the others are polarized to approximately 80%. No data have been obtained with fully-polarized photon beams.

Polarization is a tool that can be used to increase the sensitivity of a measurement to the underlying physics of the fission event. It provides two additional pieces of information that are unattainable with unpolarized beams. First, the parity of the photon absorption reaction can potentially be determined by investigating the ϕ-dependent, polarization asymmetry, $\Sigma(\theta)$. Second, polarization provides more insight into the relative contributions of each channel to the angular distribution. The models of Sects. 3.1 and 3.2 indicate that five independent transition states produce an angular distribution described by four parameters, see Eq. 3.10. The use of experimental data to extract the contributions is an under-determined problem that polarization improves by the introduction of the d parameter. Its addition reduces the surplus of unknowns to measurable parameters in the problem from two to one. Together it is clear that the use of monoenergetic, fully-polarized photon beams to study fission provides a unique contribution to the existing body of data.

4.2 Dipole Photofission

The clearest result of all the studies of PFADs from even-even nuclei is the dominance of the dipole fission for excitation energies greater than 6 MeV. Reports of this fact have historically used the ratio of b to a, that is, the ratio of the coefficients of the $\sin^2\theta$ term to the isotropic term in Eq. 3.10. Many of the experiments, in fact, have only reported on this value. The interest in this ratio is primarily historic because it does not clearly communicate the underlying physics on its own. Both the a and b coefficients are formed with dipole and quadrupole channel contributions

$$\begin{aligned} a &= \frac{3}{2}y + \frac{5}{2}v \\ b &= \frac{3}{4}x - \frac{3}{4}y - \frac{5}{4}v + \frac{5}{4}w, \end{aligned} \tag{4.1}$$

see Eq. 3.11. As such, a nonzero b/a ratio could theoretically result if the fission involves no contribution of dipole channels and all quadrupole channels. On the other hand, a clear interpretation of this ratio is given by Eq. 3.10 as

$$\frac{b}{a} = \frac{W(\theta = 90^\circ)}{W(\theta = 0^\circ)} - 1. \tag{4.2}$$

The above equation has assumed that either the polarization is zero or that the ϕ value considered is 45°, 135°, 225°, or 315°.

The b/a ratio of ^{238}U is plotted as a function of endpoint energy, E_{max}, for all previous bremsstrahlung measurements in Fig. 4.1. The data sets for ^{232}Th are included in Fig. 4.2. The general trend of decreasing b/a with photon energy is consistent for

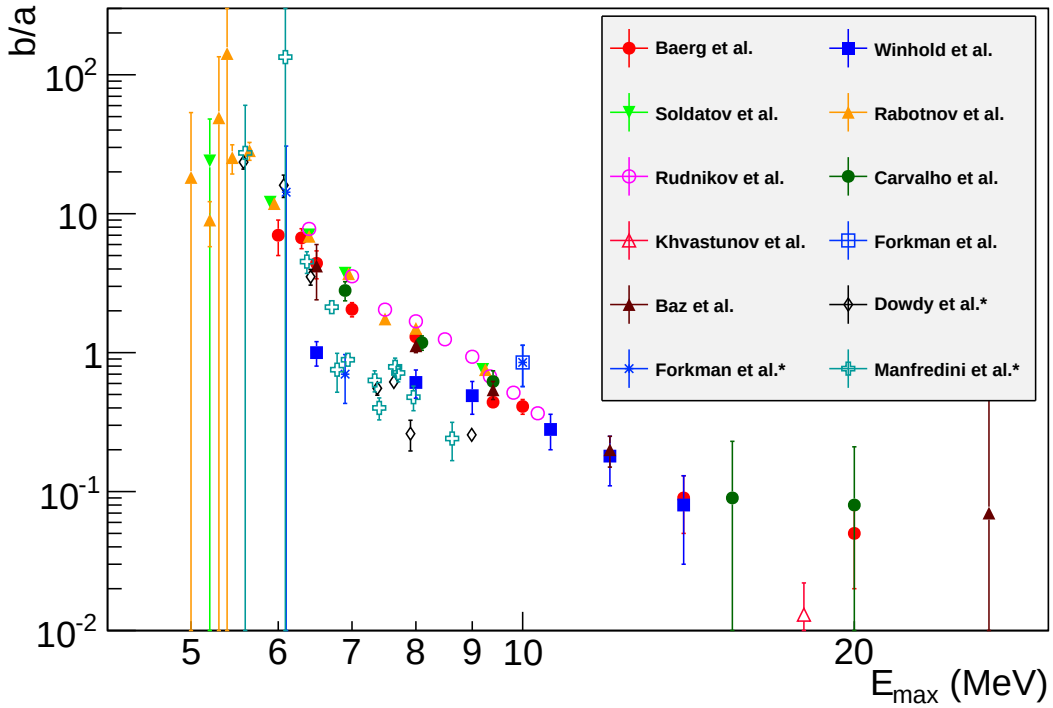

Figure 4.1: The b/a ratios for the photofission of ^{238}U have been plotted for all previous measurements to date. There is a clear trend toward decreasing anisotropy with increased E_{max}. The data sets are taken from [24, 36, 39, 40, 42–45, 48]. The three entries in the legend marked with an asterisk employed capture gamma rays whereas all other measurements used a bremsstrahlung photon beam. The monoenergetic data sets have been plotted such that $E_{max} = E_\gamma$.

all. Despite this qualitative agreement, there are yet discrepancies. Data sets that are noticeably deviant from the majority are those produced with monoenergetic photon sources as well as the data of Winhold and collaborators. It is not obvious why this is the case but it could be the result of the different beam characteristics. Given that the anisotropy increases with decreasing E_γ, it would be expected that the bremsstrahlung measurements corresponding to a specific E_{max} would produce a larger anistropy than a measurement with a monoenergetic beam centered at E_{max}. The bremsstrahlung beam consists of photons of all energies below E_{max} so that the resulting b/a value is

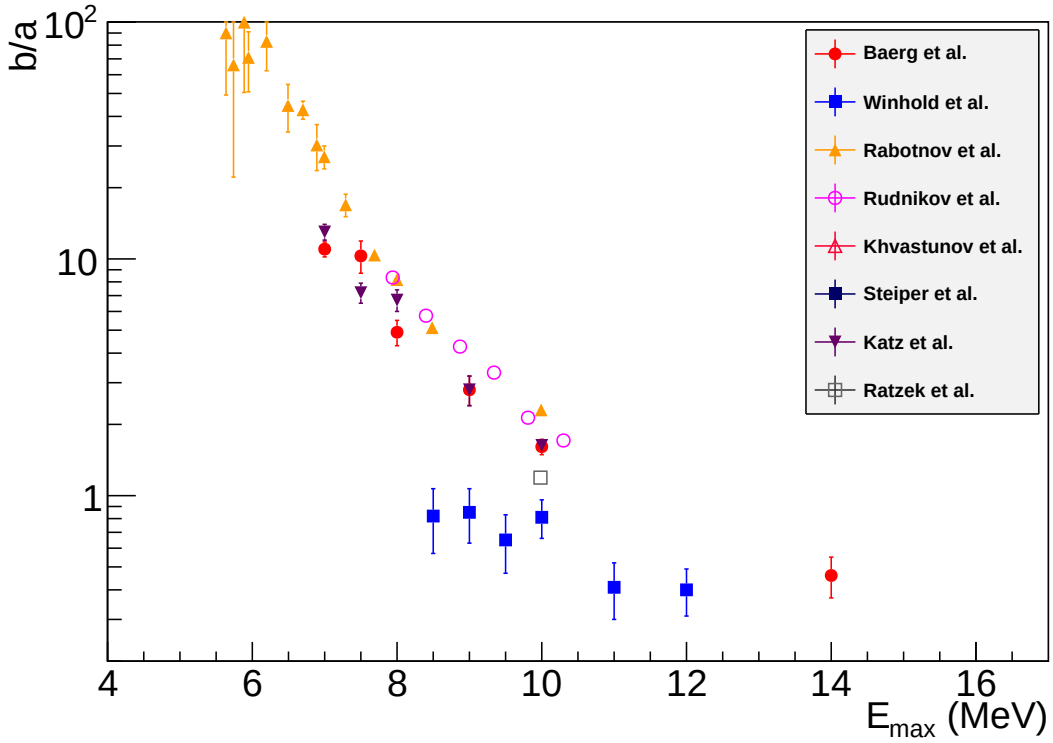

Figure 4.2: The b/a ratios from ^{232}Th measured with bremsstrahlung beams. The data sets are taken from Refs. [24, 36, 39, 43, 48].

the averaged value of all contributing states lower in energy. The measurements using monoenergetic beams, on the other hand, probe only the states within the energy width of the gamma ray beam incident on the target.

Another clear result is that the anisotropy associated with ^{232}Th is much larger than that with ^{238}U, see Fig. 4.3. One perspective on the issue could be that it is the result of a difference in barrier structures. It is known that the inner barrier is higher than the outer barrier in ^{238}U whereas it is opposite in ^{232}Th [52]. This difference has large implications to sub-barrier fission, as will be discussed in Sect. 4.5, and could potentially be the source of this above-barrier observation as well. Another applicable consideration

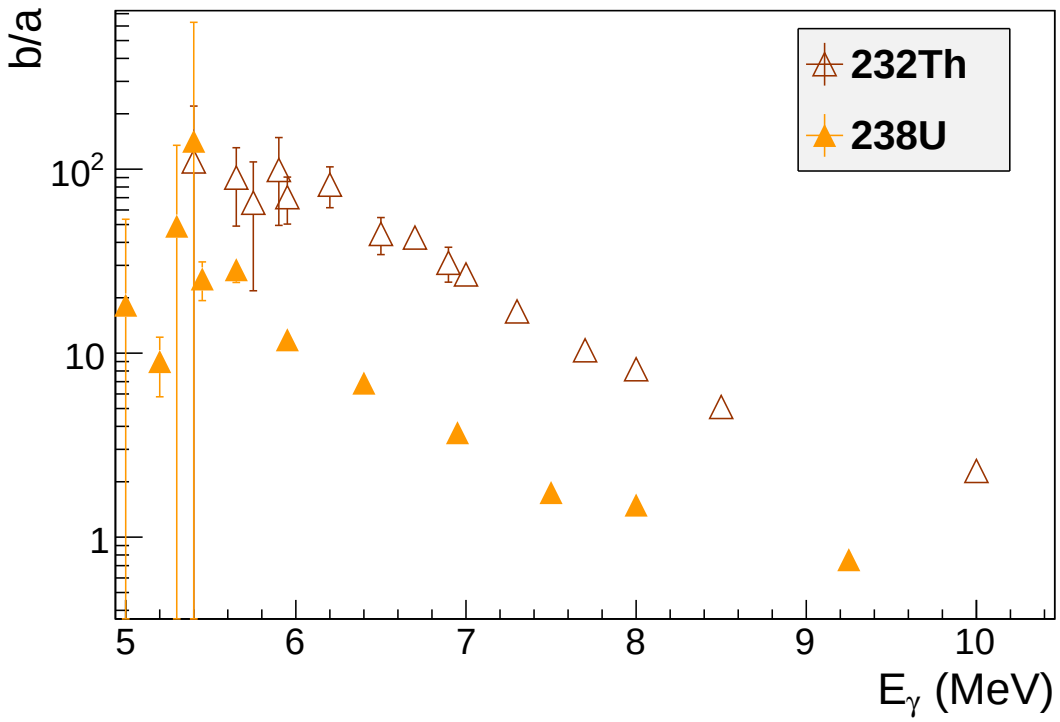

Figure 4.3: The b/a ratios for the photofission of ^{238}U and ^{232}Th are plotted. The ^{232}Th displays a significantly larger anisotropy than ^{238}U. Data are taken from Ref. [43].

provided by Schmitt and Duffield [53], is the absence of yields corresponding to mass-symmetric splits for ^{232}Th below 7 MeV; the same is not true of ^{238}U. Symmetric fission would proceed through an even parity state and would thus favor a quadrupole-type fission event. On the other hand, asymmetric fission would involve states of odd parity and thereby favor dipole fission.

4.3 Correlation of Angular Anisotropy and Mass-Asymmetry

Since the discovery of PFADs, it has also been known that, in ^{232}Th, the fragment mass asymmetry is correlated with the anisotropy. Using bremsstrahlung beams of $E_{max} = 16$ MeV, a nearly-linear relationship was observed between the mass asymmetry of the fragments, presented as the ratio of their masses, and the b/a quantity [36, 54]. In a more recent experiment, Steiper and coworkers [49] have observed the same general phenomenon using bremsstrahlung beams of E_{max} between 10 and 12 MeV. Their results corroborate the fact that the anisotropy is increased for fission events characterized by greater mass asymmetry.

4.4 Quadrupole Photofission

Fission proceeding through $J^{\pi} = 2^{+}$ states has gained much attention for energies at or below the fission barrier, 5 to 6 MeV, though many measurements up to 10 MeV have also been made. According to Bohr's theory, this is expected to proceed through the first excited state of the even-parity, $K = 0$ rotation band, see Fig. 3.3. The reporting of "quadrupole" fission has concentrated on the ratio of the c parameter to the b parameter in Eq. 3.10. The c parameter carries the most significant information because it is nonzero only if there are transition states of $J = 2^{+}$ involved in the fission event. The converse is not true because the c term is composed of the three quadrupole

channels, see Eq. 3.11, as

$$c = \frac{15}{16}u - \frac{5}{4}v + \frac{5}{16}w. \tag{4.3}$$

There are many combinations of these parameters that will cause c to be zero. The ratio of the c to b terms provides a little more information but still limited.

Knowing these facts, it is now possible to consider the results of previous experiments. At first glance, the data sets for ^{238}U are, with exception of the data of Baz *et al.* [37], coherent with one another, see Fig. 4.4. However, it is unclear whether the results of Ref. [42] and Ref. [43] are completely independent or are merely the reanalysis of the same data set. If the same data set has been used by both, then the data points below 6 MeV are the only measurements of that energy range. This would mean that the data sets are only in agreement when $E_{max} \approx 6.5$ MeV. At higher energies the results of separate measurements are in great disagreement so that little can be concluded.

As regards ^{232}Th, there are two data sets published that overlap slightly. Together these data sets indicate that the c/b ratio does not change magnitude as significantly as the b/a ratio does for E_{max} between 6 MeV and 10 MeV. However, within this range lots of interesting energy dependencies exist. The large error bars make it difficult to assign great meaning to these fluctuations but they are statistically significant variations given the reported error bars.

For energies greater than 6 MeV, the majority of the measurements indicate that c is between 10 and 100 times smaller than the b parameter. Its smallness has caused many experimenters to assume its value to be zero, which is convenient because doing

so subsequently reduces the number of free parameters in the unpolarized angular distribution by one. There is some ambiguity in doing this however, because the c parameter can be small or zero when contributions of 2^+ transition states to the cross section are actually large, see Eq. 4.3. Regardless, there have been many conclusions formed with c fixed at zero.

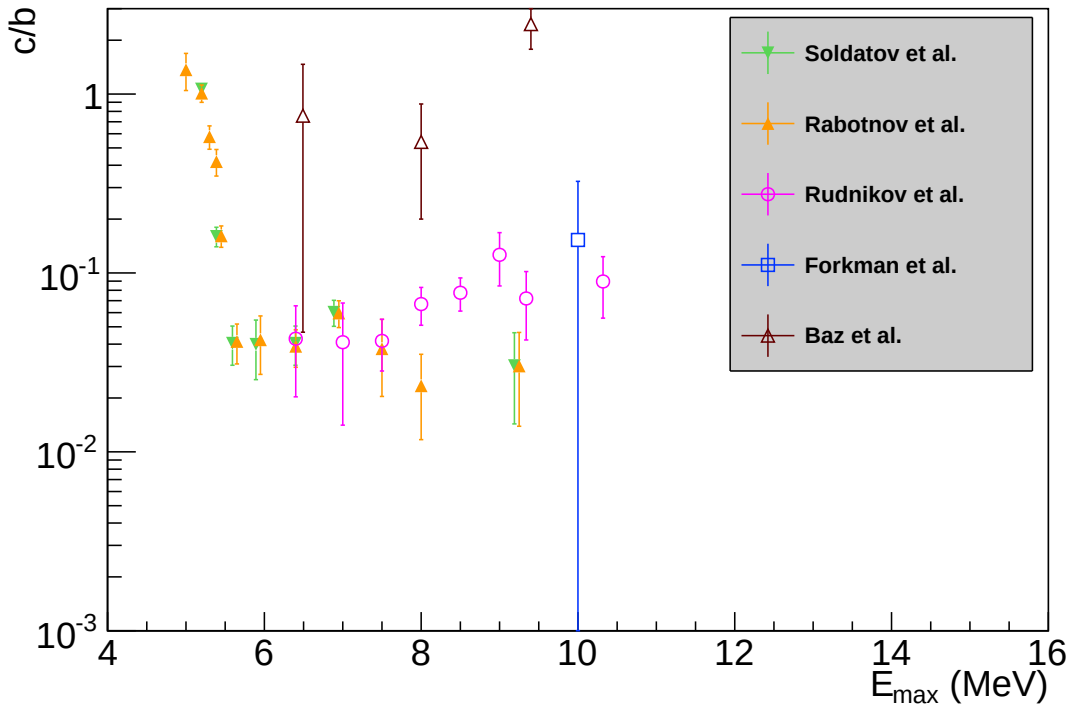

Figure 4.4: The c/b ratios from $^{238}\mathrm{U}(\gamma, f)$ measured using bremsstrahlung beams are plotted for all measurements to date. The data sets are taken from Refs. [37, 40, 42, 43, 48].

4.5 Barrier Systematics

The understanding of the potential energy surface has improved dramatically since the first experiments were carried out seventy years ago. The channel formalism of

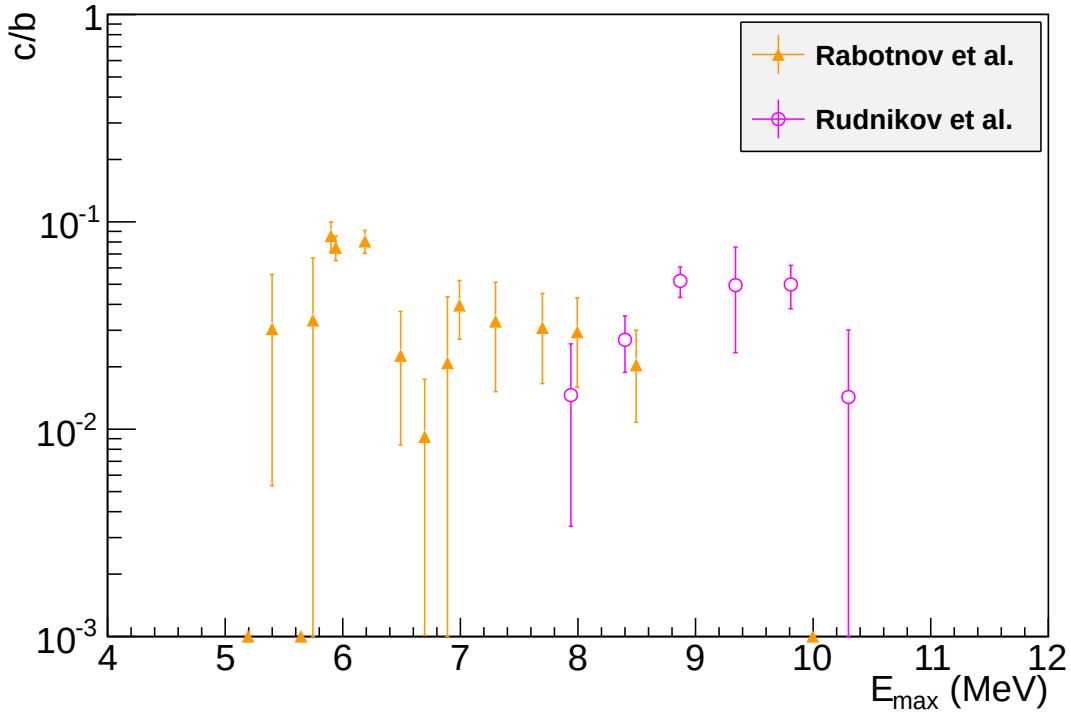

Figure 4.5: The c/b values from ^{232}Th measured using bremsstrahlung beams are plotted for all measurements to date. The data sets are taken from Refs. [43, 48].

Bohr was created with the single-humped barrier predicted by the liquid drop model in mind. Today, it is believed that most of the actinides, including ^{232}Th and ^{238}U, have a potential energy surface characterized by a triple-humped structure, see Fig. 2.3. Given the parameterization of the nuclear shape in Eq. 2.2, this corresponds to a quadrupole deformation with value $\beta_2 \approx 0.9$ and an octupole deformation of $\beta_3 \approx 0.35$ [18], see Fig. 2.2. In ^{232}Th, the third well is about 3 MeV deep whereas it is about 1.5 MeV deep in ^{238}U [34]. The relative heights and shapes of the various saddle points along the fission path are important in determining the nature of that fission event, including the angular distribution.

Even in the absence of a multihumped potential, the relative energies of the $J = 2^+$

and $J = 1^-$ states lead to structure in the energy dependence of the angular distribution. Griffin was the first to consider the importance of this by considering the relative penetrations associated with each transition state [55]. The penetration $p(E)$ is equivalent to the probability for tunneling through a barrier and was estimated by Hill and Wheeler [56] to be

$$p(E) = \{1 + \exp\left[2\pi(E_f - E)/\hbar\omega_f\right]\}^-1 \tag{4.4}$$

for a barrier with the shape of an inverted parabola. The height of the fission barrier with respect to the ground state is given by E_f, $\hbar\omega_f$ is a value indicative of the shape of the barrier, and E is the excitation energy. If each transition state is considered to be a unique barrier, then this penetration factor is proportional to the probability for fissioning through specific transition states. Using this line of thinking, Griffin suggested that if the dipole fission barrier is greater than the height of the quadrupole barrier, as is consistent with the ideas of Bohr, then the energy difference between the barrier penetration would diminish the natural preference for E1 absorption considerably more than for E2. An increased importance of quadrupole fission would become pronounced in the angular distribution. The data of Refs. [42, 43] provide some evidence for this fact in ^{238}U because the c/b ratio rises sharply as the energy decreases. Their interpretation began with the ideas of Griffin and concluded with a predicted energy dependence for the b/a and c/b ratios. It was stated in Ref. [43] that the interplay of the relative penetration through each of the barriers would cause both ratios to peak slightly below the point at which the energy dependence of the cross section is no longer determined

by the penetration factor. The ^{238}U data alone do not support this beyond a doubt. However, the consideration of the ^{232}Th data with the remaining collection of actinide data sets provides a more impressive body of corroborating evidence [35].

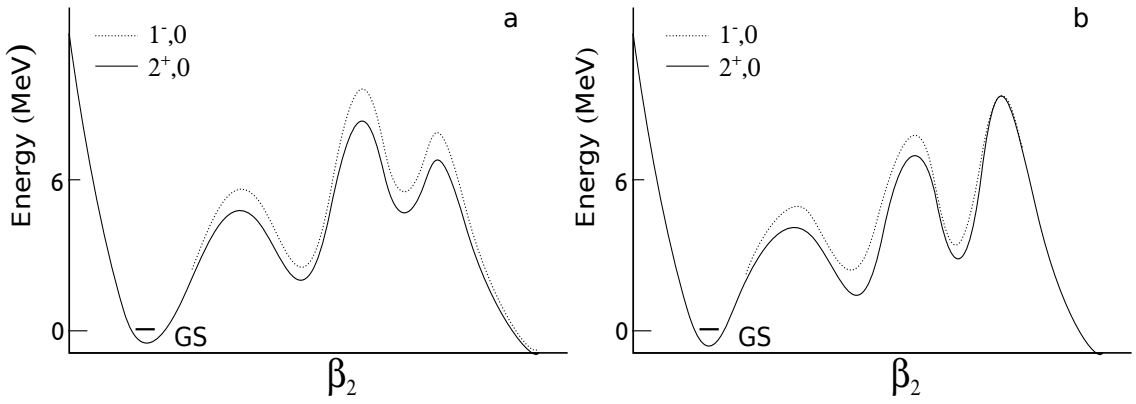

Figure 4.6: A diagram of the different fission barrier heights assumed by Rabotnov *et al.* [43] and Vandenbosch [57] and generalized to a triple-humped barrier. A schematic triple-humped barrier is shown for the different energy $(J^\pi, K) = (2^+, 0)$ and $(1^-, 0)$ transition states. The argument of Rabotnov *et al.* assumed the ordering of the states depicted in (a), which is in accord with Bohr's hypothesis. Vandenbosch assumed that the the states became degenerate at the outermost barrier as shown in (b). Figure (a) also serves to illustrate his argument about the b/a ratio.

There has been little discussion of the effect of a triple-humped fission barrier on the angular distribution. On the other hand, much has been written with regard to the double-humped fission barrier. The arguments presented by Rabotnov *et al.* included an account of the effect that a double-humped barrier would have on the angular distribution. It was concluded that the presence of a double-humped fission barrier ultimately shifted the above-mentioned peaks downward in energy with respect to the leveling off of the cross section [43]. The arguments were somewhat specific though, because they addressed the case that the dipole barrier is always higher than the quadrupole barrier, see Fig. 4.6. They also fail to account for ^{232}Th because the

data exhibit no significant rise in the c/b ratio with decreasing energy.

A suitable explanation has been presented by Vandenbosch [57] and is based on three assumptions. They are that the inner barrier is lower than the outer barrier, the outer barrier corresponds to a reflection-asymmetric state, and the angular distribution is determined at the outermost barrier. According to recent calculations, see Fig. 2.3, the first two of these are well satisfied. The third assumption is well justified because a deep potential well separating the two barriers could destroy angular distribution because of K-mixing [43]. A reflection-asymmetric nucleus has an excitation spectrum containing a 1^- state comparable in energy to the 2^+ state in the "ground-state" band, see Fig. 4.6. Because of this fact, greater inhibition of the dipole channel by barrier penetration is not present in ^{232}Th. The explanation of Vandenbosch also addresses the much smaller b/a ratio for ^{238}U as compared to ^{232}Th. In ^{238}U, the outer barrier is lower than the inner barrier. The energy required to overcome the inner barrier will result in a greater excitation energy at the outer barrier. As such, enough energy will exist to excite nonzero K states, which will wash out the angular anisotropy. The situation is opposite in ^{232}Th, because the outer barrier is highest. The nucleus will be colder at the point critical for determining the angular distribution so that only the lowest energy states will be able to contribute. Only $K = 0$ states will contribute, and the anisotropy will arise almost purely from the $K = 0$ state.

4.6 Prompt-fission neutrons

Recent efforts at TUNL that I have been involved with have led to first observations of anisotropies in prompt fission *neutron* angular distributions (NADs) [1]. Photofission was induced in ^{238}U, ^{232}Th, ^{235}U, and ^{239}Pu using 100% linearly-polarized photon beams with energies between 6 and 10 MeV. Neutrons were detected in the plane of polarization and perpendicular to it. The anisotropy with respect to rotations about the beam axis has been characterized by the asymmetry, Σ, which is defined as

$$\Sigma(\theta) = \frac{Y(\theta)_{\parallel} - Y(\theta)_{\perp}}{Y(\theta)_{\parallel} + Y(\theta)_{\perp}}. \tag{4.5}$$

The quantity $Y(\theta)_{\perp}$ is the yield measured at angle θ. The subscript $\perp$ indicates that the detector was positioned at $\phi = 90^{\circ}$ or $\phi = 270^{\circ}$, whereas $\parallel$ indicates $\phi = 0^{\circ}$ or $\phi = 180^{\circ}$. A few observations are worth making about these data. First is that the neutron asymmetries are nonzero for even-even nuclei whereas they are nearly zero for odd-A nuclei. The reason for this is believed to be related to the number of K states involved in the reaction. An even-even nucleus that absorbs a photon is only excited to a 1^-, 2^+, or 1^+ state with any noticeable probability. Because the odd-A nuclei shown in Fig. 4.7 have half-integer ground state spins, the absorption of the photon can excite the nucleus to more states than are excited in even-even nuclei. When more states are involved in defining the angular distribution, the unique characteristics of any individual state will be washed out. Another interesting characteristic of this data is that the asymmetry decreases with increasing photon energy analogously to the FADs.

Since the majority of prompt fission neutrons are evaporated from already accelerated fragments, this gives a reason to believe that the neutron asymmetry is largely the result of an underlying fission fragment asymmetry. As such, a complete understanding of the prompt neutron angular distributions would benefit from understanding the FAD produced with nearly-monoenergetic, 100% linearly-polarized photon beams. Since no measurements of this sort have been carried out in the past, this need will be addressed by the present thesis work.

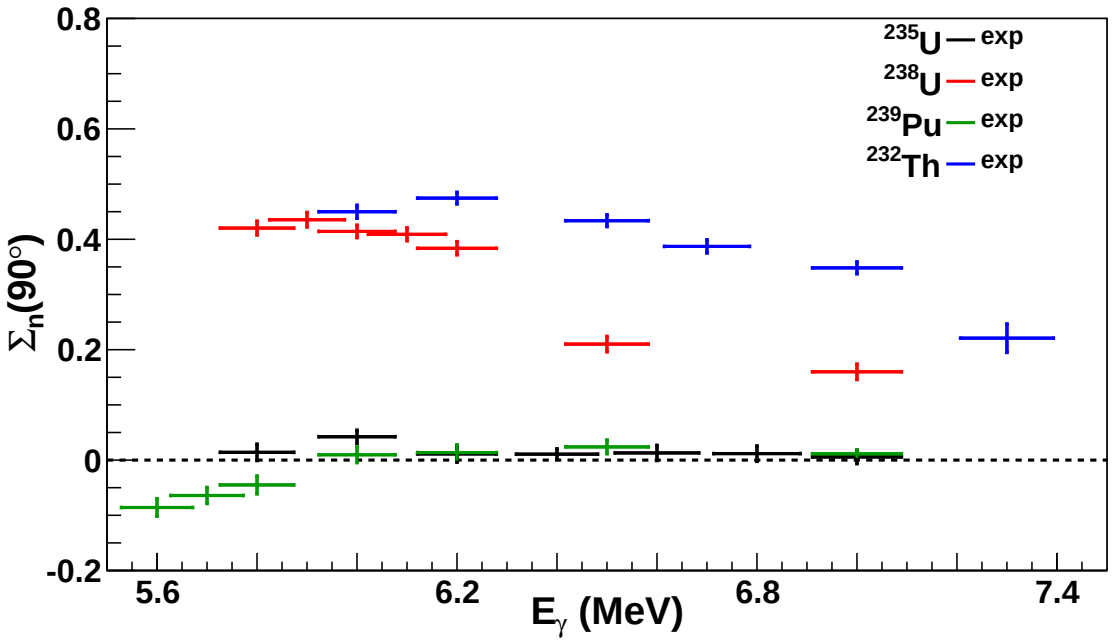

Figure 4.7: The nonzero prompt fission neutron asymmetries measured using 100% linearly-polarized beams at HIγS [1]. The asymmetries, Σ_n, defined as $\Sigma_n(\theta) = [\mathcal{Y}_n(\theta, \phi = 0) - \mathcal{Y}_n(\theta, \phi = 90°)]/[\mathcal{Y}_n(\theta, \phi = 0) + \mathcal{Y}_n(\theta, \phi = 90°)]$ where $\mathcal{Y}_n$ is the neutron yield.

Chapter 5

The Experiment

5.1 Description of the Experiment

Two distinct data collection efforts were conducted to measure polarized-photofission angular distributions. A measurement of this type requires a number of key components: a beam of incident polarized gamma rays, a target, charged-particle detection system, and data-readout system. The first of these was readily produced at Triangle Universities Nuclear Laboratory (TUNL) by the HIγS facility, which produces high-intensity and high-resolution photon beams with 100% polarization. The beams it produced were incident on either a ^{232}Th or ^{nat}U target where photofission was possibly induced. Silicon strip detectors (SSDs) were used to detect fission fragments and alpha particles produced in the target. Finally, signals resulting from the successful detection of a particle were processed by a VME-based CODA data acquisition system (DAQ) [58]. In both runs, the scattering chamber was positioned in the upstream target room (UTR) at HIγS. The experimental setup will be described in more detail in Section 5.2, the targets and measurements related to them will be discussed in Sec-

tion 5.3, the relevant details of detector operation will be described in Section 5.4, and the data-readout system will be explained in Section 5.5.

5.2 Experimental setup

The HIγS facility produced nearly-monoenergetic photon beams by means of Compton backscattering inside the optical cavity of a storage ring based free-electron laser (FEL). These had a pulsed temporal structure with frequency of 5.58 MHz that resulted directly from the periodicity of the electron bunches from which the FEL light backscattered. During this project, the beams were produced with energies between 5.7 and 7.6 MeV and fluxes-on-target between 1 x 10^7 γ/s and 2 x 10^7 γ/s, see Table 5.1. The HIγS facility is capable of producing either 100% linearly-polarized or circularly-polarized beams. Circularly-polarized beams were used to measure systematic differences between detectors at the same polar angle that are attributable to geometry, strip functionality, and signal processing. Prior to reaching the target, the beams were collimated to a diameter of 1.91 cm using a Pb collimator. In order to monitor the flux while the beam was incident upon the target, two separate plastic scintillator systems, one in each experimental effort, were used. The energies of these beams were measured using a high-purity germanium (HPGe) detector that was positioned in the beam during energy measurements, see Fig. 5.1.

The collimated photon beams passed through the center of an evacuated scattering chamber that contained the target and the detectors, see Fig. 5.2. The scattering cham-

Energy MeV	Polarization	Flux-on-target γ/s	$\Delta E_\gamma/E_\gamma$ %	Target
5.9	Linear	2.2×10^7	3.4	^{232}Th
6.2	Linear	1.8×10^7	$\approx$2	^{238}U
6.2	Linear	1.1×10^7	3.3	^{232}Th
6.7	Linear	2.5×10^7	≈ 3	^{232}Th
7.2	Linear	2.7×10^7	3.4	^{232}Th
7.6	Linear	2.6×10^7	3.0	^{232}Th
7.6	Circular	2.5×10^7	3.0	^{232}Th

Table 5.1: The list of photon beam energies and characteristics to measure a particular target. No beam profiles were measured for the 6.7 MeV ^{232}Th and 6.2 MeV ^{238}U data sets, so no measured energy spreads are included. However, in both cases, beam characteristics were measured for photons beams nearby in energy and collimated with the same collimator. Inferred values based on these representative measurements are included as approximate values.

ber pressure was maintained at approximately 10^{-5} Torr to ensure that the fragments were able to traverse the distance between the target and the detectors unhindered. Each target was rotated for the purpose of avoiding geometry-related detection bias between paired detectors. The rotation was defined by the set of Euler angles $\phi = 42°$, $\theta = 59°$, and $\psi = 30°$. This rotation assumes that the surface normal of the target's largest area side is oriented parallel to the positive z-axis defined by the downstream beam axis prior to rotation.

The target was surrounded by two pairs of 16-element silicon strip detectors (SSDs) in both runs, see Fig. 5.2. The SSDs were tilted by 22.5° to optimize the solid angle coverage afforded by their trapezoidal shape, see Fig. 5.3. With the tilt, the active area of the SSDs covered nearly 2π steradians when considering the straggling of charged particles within the target and the finite target geometry. One pair of detectors was positioned to detect fragments emitted at θ angles greater than 90° and the other to

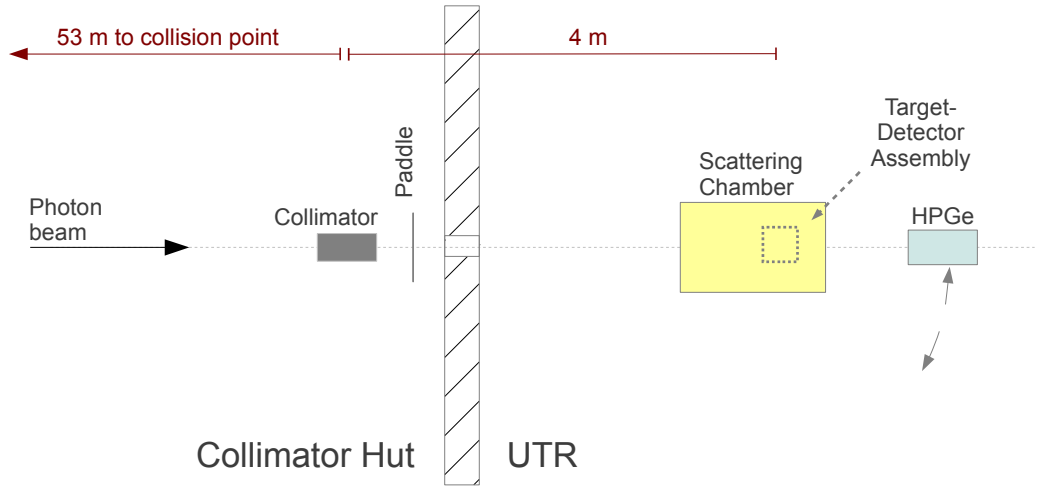

Figure 5.1: The layout of the experiment in the UTR. The photon beam is collimated first and then subsequently encounters the paddle system, the scattering chamber, and finally the HPGe detector. The HPGe detector was positioned out of the beam when not measuring the beam energy. The target and detector assembly reside inside the scattering chamber.

detect those at primarily less than 90°. The target was positioned over the downstream pair of detectors so that fragments emitted at $\theta = 90°$ could be detected, which is the angle corresponding to the largest predicted asymmetries. The polarization dependent term of Eqs. 3.10 and 3.18 has a minimum at $\phi = 90°$ and $\phi = 270°$, whereas it peaks at $\phi = 0°$ and $\phi = 180°$. To be sensitive to this ϕ dependence, paired detectors were positioned differently in the ϕ direction by 90°. One was positioned at either $\phi = 0°, 180°$ and the other was at $\phi = 270°, 90°$, respectively. In this way, a single pair of detectors was sensitive to the extreme values of the polarization dependent term of the angular distribution.

The detector-target assembly was designed to minimize shadowing effects. Shadowing is the inhibition of a fragment from being detected due to the presence of material

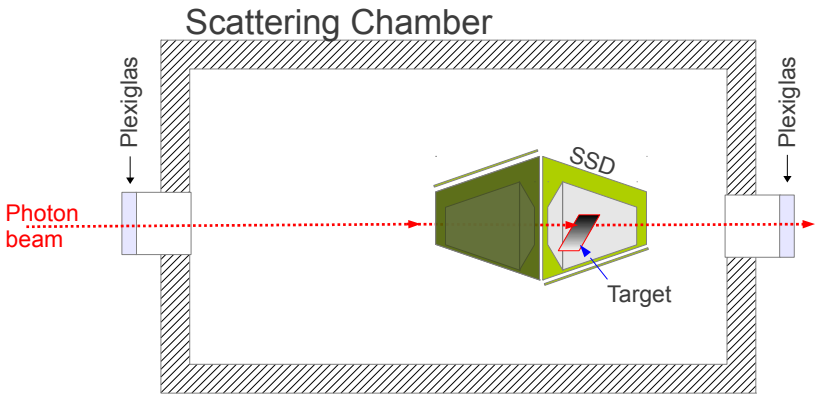

Figure 5.2: The layout of the interior of the scattering chamber. The upstream detectors measure fragments with trajectories around $\phi = 90°$ and $\phi = 180°$ whereas the downstream detectors measure those around $\phi = 0°$ and $\phi = 270°$.

in its path. It was not possible to completely eliminate all shadowing, and the detector most affected by shadowing was the downstream-bottom detector, because it resided directly beneath the target and its mount.

5.3 Targets

Two targets were used during this project, ^{232}Th and ^{nat}U, whose characteristics are provided in Table 5.2. The isotopic ratio of ^{235}U to ^{238}U in the ^{nat}U target was measured following the method of Ref. [59]. Though these targets are not significantly thick in terms of absolute physical dimensions, they are infinitely thick from the perspective of a fission fragment. Fission fragments are charged particles that necessarily interact with the medium in which they travel by means of the Coulomb interaction. Ultimately, this interaction will cause them to surrender the entirety of their energy over a distance

shorter than the smallest dimension of the target. Heavier fragments have shorter ranges than lighter fragments in the same material because of their higher charge and less initial kinetic energy. A fission fragment traveling through either of the ^{232}Th or ^{238}U target has a maximum range of about 10 μm.

Three effects must be considered that result from the thick nature of the targets. First, the fragments can only escape from a thin surface layer so that each face of the target is effectively an independent target. Second, despite the fact that two fragments are produced during a fission event, only one of them can potentially be detected. If one fragment has momentum toward the nearest surface of the target, momentum conservation requires that the other fragment would be directed opposite so that both are not simultaneously detectable. Finally, the interaction of the fragments with the target material causes them to scatter and thereby alter their initial momentum direction. For heavy ions scattering on the electrons in the material, the momentum change is small. However, the continuous nature of the interaction and the occasional scattering from a target nucleus causes this change to become sizeable. Straggling is a random process that becomes more pronounced when the fragment energy approaches zero. The net result is that the angular distribution of the photofission reaction is altered substantially by the straggling process prior to detection in such a way to smear the angular distribution.

	^{nat}U	^{232}Th
Nominal length (cm)	3.34(1)	5.01(1)
Nominal width (cm)	2.35(1)	28.0(1)
Nominal thickness (cm)	0.09(1)	0.1(1)
Isotopic composition	^{238}U - 99.991% ^{235}U - 0.009%	^{232}Th - 100.0%

Table 5.2: A comparison of the characteristics of the two targets employed in this project.

5.4 Silicon Strip Detectors

Four Micron Semiconductor YY1 SSDs were used during this work, see Fig. 5.3. The depleted silicon layer in these detectors was 300 ± 15 μm thick. Though full depletion is achieved with a -10 V bias, a slightly greater -30 V bias was applied to improve their response to heavy ions. Each SSD had 16 strip contacts that shared a common ground. These were arcs of a 0.5 cm radial width and a common center of curvature located 5.39 cm from the inner edge of the innermost strip.

The charge of the output signal from an SSD yields information about the energy of the fragment that caused it. It was possible to calibrate the detectors to low energy alpha particles to provide some coarse energy calibration for the response of the detector to incident fragments. Regardless of the ability to calibrate the detector, the fragment energy will have been degraded by a random amount prior to detection. The reason for this is the energy straggling of the fragments in the thick targets that was discussed in Sect. 5.3. There is, therefore, little information recovered with respect to the initial energy of the detected fragments.

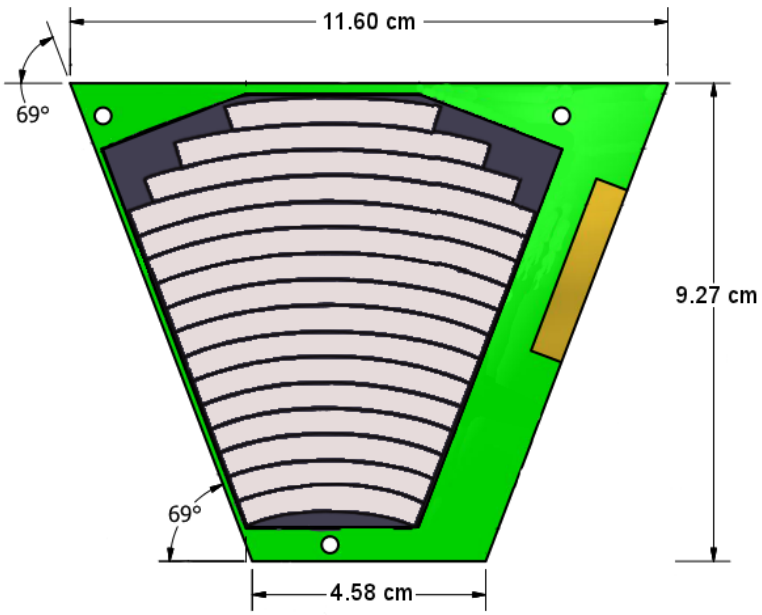

Figure 5.3: A diagram of a SSD used in the experiment. The strips are each 0.5 cm wide. The first twelve strips span 40.0° and the remaining strips cover 35.1°, 28.1°, and 18.3°, respectively.

5.5 Signal Processing and Readout

The signal processing was accomplished with a set of electronics located inside the UTR. The close proximity decreased signal attenuation, which occurs when signals drive long stretches of cable, and minimized the complexity of the cabling for 64 Si strips.

Signals produced by the SSDs were processed in an event-wise fashion by a circuit that was replicated for all 64 strips, see Fig. 5.4. To simplify explanation, the circuit

will be described in the order that a signal would have traveled through it. The signals produced in the Si strips were first processed by one of four 16 channel preamplifiers developed at Argonne National Laboratory [60]. These produced two outputs for one input signal: one was the solely preamplified version of the input signal and the other was the result of processing by a fast amplifier for timing purposes. The first of these was integrated and shaped by a Caen N568B 16 channel spectroscopy amplifier. The analog signal it produced became the input to a Caen V785 peak-sensing analog-to-digital converter (ADC). The timing output from the preamplifier was processed by either a constant-fraction discriminator (CFD) or a leading-edge discriminator (LED) to produce a differential ECL logic signal. The CFDs and LEDs were Caen 812b and 895 modules, respectively. Both initially lacked software drivers that enabled them to be used with CODA. Existing drivers were modified and implemented to make these functional. These logic signals were used in a variety of ways. First, they were combined with a logical-OR to produce the common gate for the ADC and secondly as a common start for a Caen V775 time-to-digital converter (TDC). Finally, a copy of these signals was delayed by 100 ns and used as the stop for the corresponding TDC channel.

During the time data were digitized or read from the ADCs, TDCs, and the Struck SIS3600 readout controller, the DAQ was prevented from acquiring new data signals by means of a global busy veto. The global busy was formed by the overlap of the individual busy signals from the digitizers and the controller. The veto of signals not only prevented a lockup of the DAQ but was also used to measure the live time fraction, the fraction of time during which the system accepted new signals. The live time

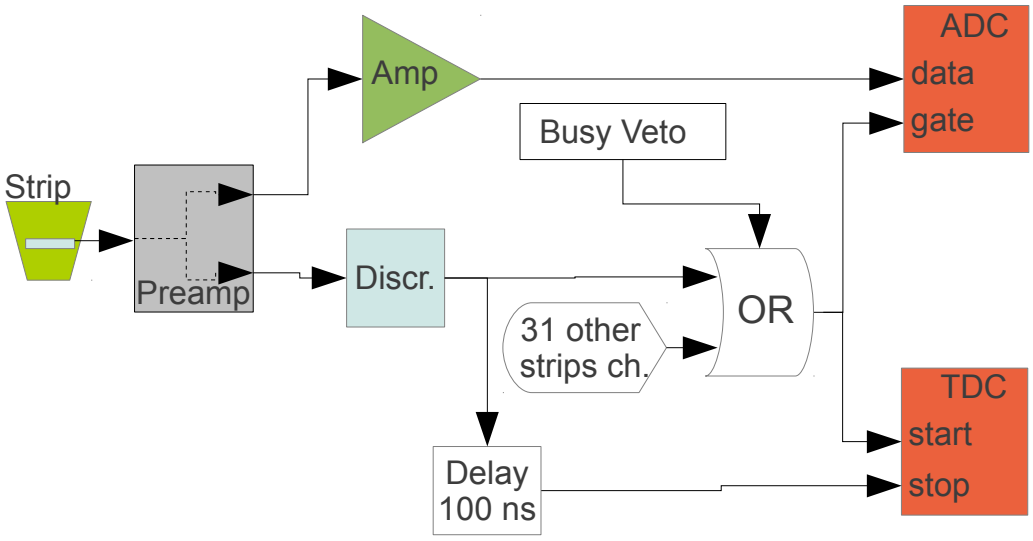

Figure 5.4: A block diagram of the signal processing circuit used for each of the 64 strips. There were two ADC-TDC pairs employed and each pair received a unique common gate formed by the logic signals of the associated 32 strips.

fraction (LTF) was determined for each strip independently using the integrated alpha yields. The procedure will be discussed in more detail in Sect. 6.4. The discriminator thresholds were adjusted to prevent the digitization of electronic noise and thereby maximize the live time fraction.

Altogether, circuits for four of the SSDs were successfully implemented, which corresponded to 64 data channels. The shear number of data channels necessarily complicated the system of electronics. The circuit for an individual detector, diagrammed in Fig. 5.4, was replicated 64 times. Fortunately, the VME electronics used in this circuit typically had high-density inputs grouped by units of 8 or 16. This feature alleviated

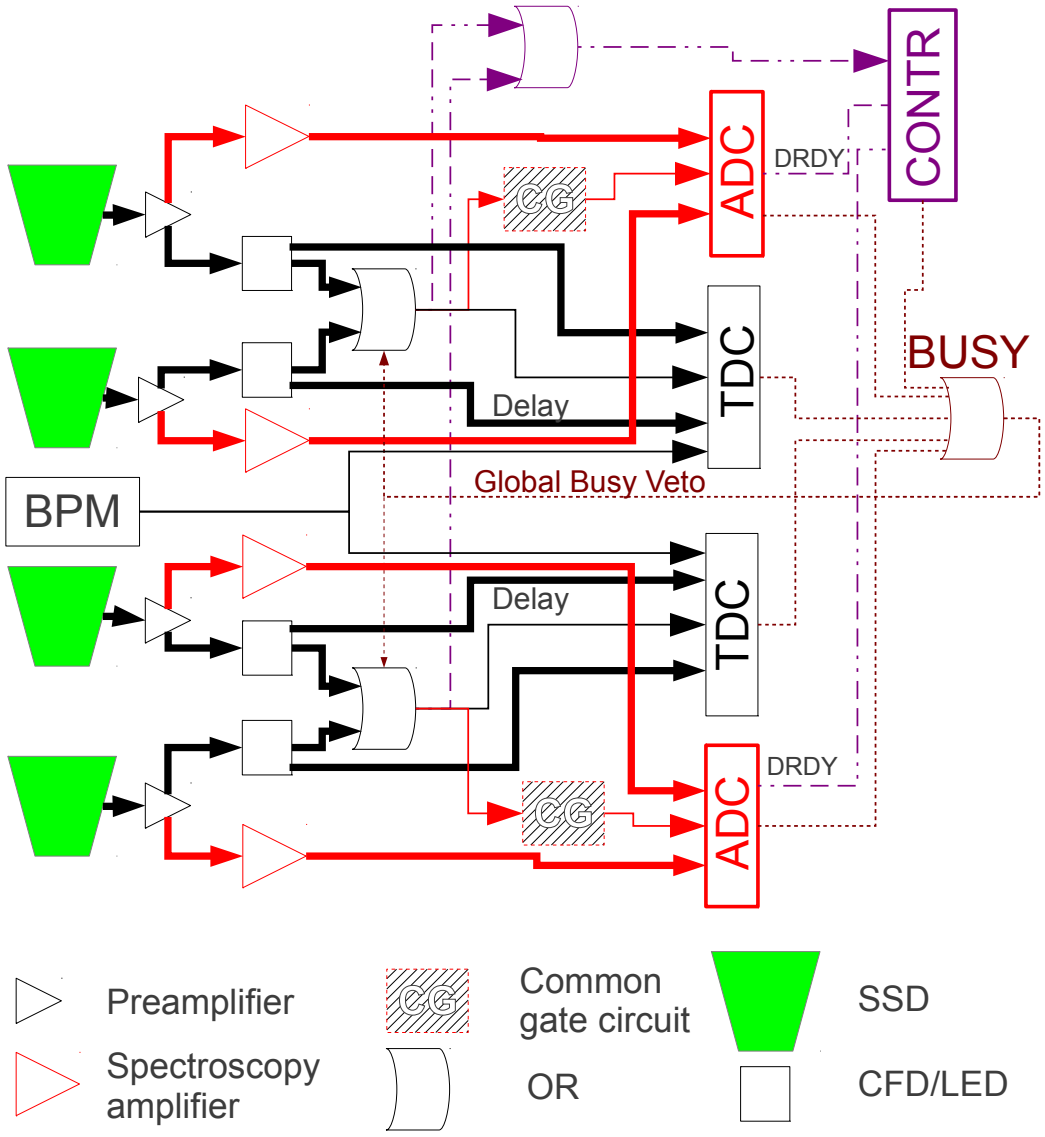

Figure 5.5: A block diagram of the signal processing circuit used during the experiment. With the exception of the global busy veto, the data flow is from left to right. Thickened lines represent 16 data channels and thin lines represent single data elements. The ADC circuit (red) and the TDC circuit (black) begin together and split following the preamplifier. The data ready (DRDY) signals lead to the controller (CONTR, purple). All of the important aspects of the circuit are shown explicitly. Components such as converters from ribbon connectors to lemo connectors were located throughout the circuit and are not shown. Also not depicted is the circuit associated with the scaler.

some of the challenges that resulted from wiring together large numbers of independent signal processing modules. The sixty-four chains of signal processing elements were grouped into four sets of 16, analogous to the grouping of the SSDs. These were further subdivided into two groups that each contained 32 data channels. This was done because the ADCs and TDCs were capable of processing 32 channels each. Therefore, to digitize all sixty-four channels, two ADC-TDC pairs were used. It was unlikely that both of these would have data at the same time so an intelligent readout of these digitizers was used. Each individual ADC-TDC pair used an independent common gate and common start and were only read out if the associated ADC had processed data ready for reading. It was unecessary to store incremented data for every channel and so a single Struck SIS3800 scaler module was used.

To run all of the VME modules in this experiment, the ADCs, TDCs, scaler, controller, and four discriminators, more than one VME crate was necessary. All of the modules except for the discriminators were powered by a single VME crate so that CODA could read data from a single source. This was not completely necessary but reduced the complexity of the system. The discriminators were run in an independent VME crate from the other modules since they are "dummy" modules that only rely on the VME crate for power and remote control purposes. The ORCA data acquisition system [61] was used to communicate with these modules.

The SSDs were very sensitive to the presence of electronic noise in the experimental hall and in the common ground such that efforts to reduce it were necessary. The noise was reduced through a trial-and-error process that ultimately improved grounding

within the system. Multiple steel and copper braids were used to connect all electronics crates to each other and to the scattering chamber. In addition, the entire electronics system was run through a single isolation transformer, though little difference was found between isolation and no isolation.

5.6 Photon Beam Measurements

The photon beam energy and width were measured by moving a 110% efficient, as measured with respect to a 3"x3" NaI(Tl) detector, HPGe detector into the beam line. To prevent damage to the detector from high rate operation, precision-machined copper attenuators were inserted into the beam upstream of the UTR. These reduced the flux by a factor of approximately 10^5. The ADC spectra from the HPGe was calibrated using natural background lines from the decay ^{208}Tl and ^{40}K, see Fig. 5.6.

The flux of the photon beam was measured using either a single plastic scintillator paddle or a system of five plastic scintillator paddles while collecting data. The data taken for ^{232}Th used the former and the data for ^{238}U used the latter. The number of detection events by these paddle systems were stored as a scaler value. A value for the flux was then obtained with a measured conversion factor, determined as the inverse of the detection efficiency. In both cases, calibration of the paddles used a 100%-efficient NaI detector and precision copper attenuators that were used to attenuate the photon beam by known amounts. Because this project did not aim to measure total cross sections, the measurement of the flux was primarily a diagnostic measurement and

the calibration was only done at a single energy. The conversion factors are energy dependent so that the measured value is nominal for the energies at which it was applied. The conversion factor for the single-paddle system was measured to be 225 γ/count whereas the five-paddle system had a conversion factor of 75 γ/count.

5.7 Geant4

To compute the effect that charged particle interactions have on the measured angular distribution as well to understand the experimental geometry, version 4.9.5.p01 of the GEANT4 simulation tool-kit [62] was used. GEANT4 is an object-oriented simulation package that computes particle transport through a user-defined geometry in an event-by-event manner. It was chosen as the computational tool, because it is readily customized to store any information along the track of a particle. This was crucial because the correction of the angular distribution for the charge straggling effect required detailed knowledge of correlations between the energy, initial momentum direction, and detection probability.

The GEANT4 simulation required the definition of a physics list, an event generator, and an experimental geometry. The physics list is a list of physical processes that comprise models for the computation of quantities such as energy loss as the simulated particle interacts with the geometry. The simulation used in this project made use of the GEANT4-included G4EmStandardPhysics_option3 class. Within this physics list, the continual loss of energy due to Coulomb interaction, multiple scattering, and nuclear

stopping processes is accounted for using modern stopping power theory. The energy loss calculations are founded on the tabulation of stopping powers for ions heavier than helium by the International Commission on Radiation Units (ICRU) Report 73 [63]. A further process was added that imposed a maximum distance interval of 0.3 μm between calculated interactions. Its presence removed computational inaccuracies inherent in the transport process.

For the results of the simulation to be applicable to the experiment, the detector geometry must be created as close to the real geometry as possible. In order to reflect the precise locations of the targets, two simulations of the experiment were written. The two are identical in all respects except the target placements. The construction of the geometry was simplified for the current project, and future projects, by the definition of a YY1-design Si strip detector builder class, see Appendix D.

The final requirement of the simulation was the definition of the event generator. The event generator, otherwise known as the primary source generator, was written to produce particles within the volume of the target. To reduce the number of simulated events that failed to escape the target, the particles were randomly generated within a specified depth of the target surface. Each simulation used either a single fragment or a distribution of randomly-sampled fragments from an experimentally-measured mass yield spectra [11, 64]. In the latter case, the energy given the fragment corresponded to the experimentally measured average total kinetic energy (TKE). The average TKE for a specific mass split was used, see Refs. [11, 64]. From the average TKE and the

chosen fragment mass, the energy could be determined to be

$$E_1 = TKE\frac{A_2}{A_f}, \tag{5.1}$$

using momentum and energy conservation. In Eq. 5.1, only two fragments are assumed to share the energy. In that sense, neutron emission and tertiary fission events are not considered in the model. The E_1 is the kinetic energy of one fragment, A_2 is the mass of the other fragment, and A_f is the mass of the fissioning nucleus. In order for GEANT4 to transport any particle through the geometry, a proton number must be assigned to it. In the present model, this assignment was based upon a simple rule that required the Z/A ratio of the simulated ion to be equal to that of the original fissioning nucleus. All simulated fragments were therefore very neutron rich. The rule is not rigorous but is instead a simple tool to generate ions near to the physical reality. This ambiguity is afforded by the reality of the reaction, because soon after the fragments have been fully formed, they change their mass by neutron evaporation. The technique for proton number assignments is modeled after other fission codes [65].

The GEANT4 simulations were developed to account for the finite-geometry and charge-straggling effects that are present in the raw fragment yields. To gain insight into the nature of the fission process, these effects must be removed. A detailed account of methods by which these simulations were used and the results can be found in Chapters 7 and 8.

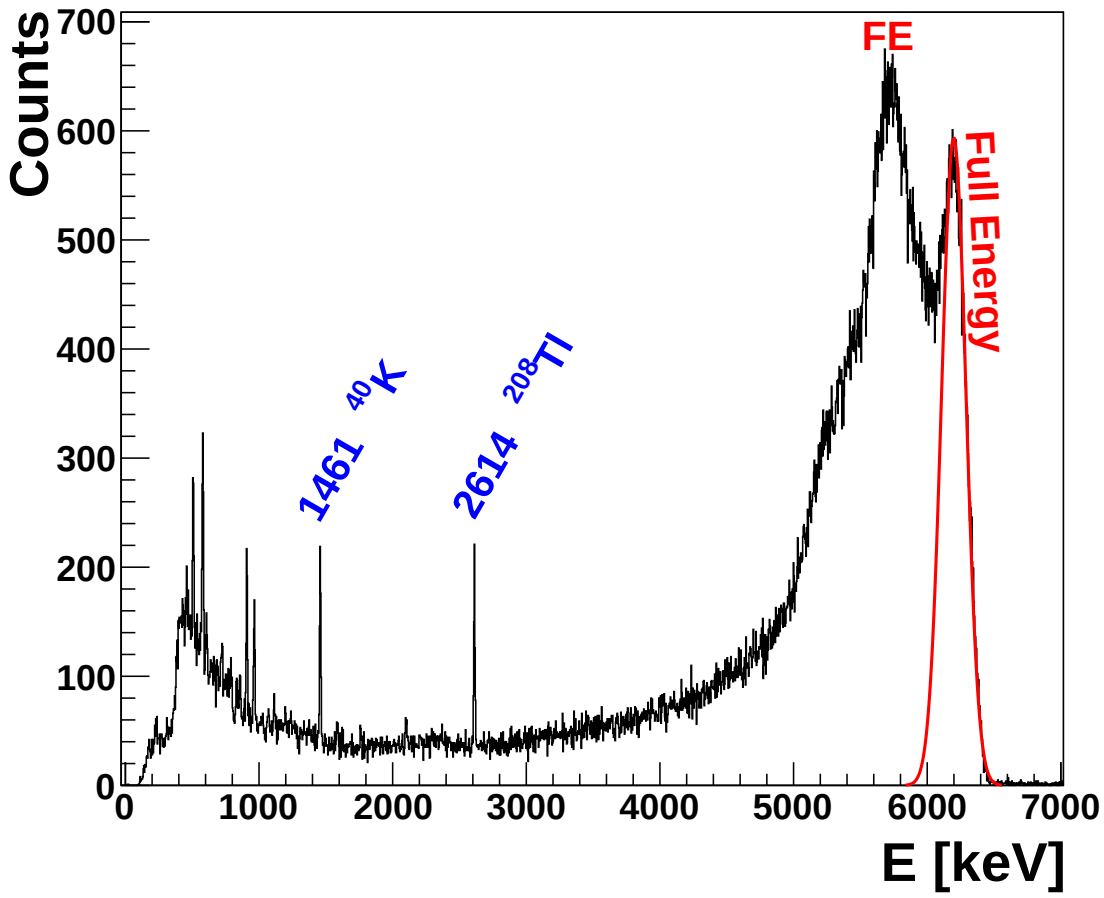

Figure 5.6: The HPGe spectrum of a 6.2 MeV photon beam. The natural lines used to calibrate the spectrum are labeled as well as the full energy and first escape peak (FE). The solid red line at the full energy peak is a Gaussian fit. It is indicative of the true beam profile without the detector response. The spectrum shown corresponds to a photon beam of energy 6200 $\pm$ 90 keV.

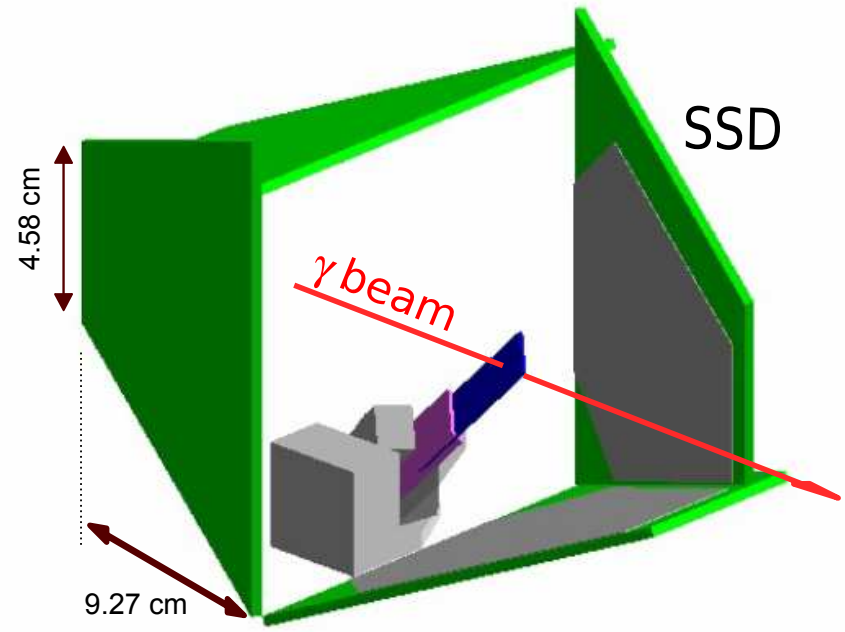

Figure 5.7: The GEANT4 simulated geometry. Geometry differences between geometries of the ^{232}Th and ^{238}U simulations were only slight variations in the target orientation. The green objects in the image are the four SSDs that surround the target, which itself is depicted in blue. The photon beam travels through the geometry along the red line from left to right.

Chapter 6

Analysis I

6.1 Overview of the Analysis

The process extracting the angular distributions from the raw data can be broken into two different stages, see Fig. 6.1. The first stage was data-centric in nature. During this process, the data were combined, calibrated, background subtracted, integrated, and corrected for the live-time fraction. The culmination of this work was the production of corrected yields for each strip of the SSDs, Y_i. The second stage was devoted to the modeling of the experiment for the purpose of calculating corrections of the effects caused by fragment straggling within the target. Ultimately, these corrections were combined with the parameterized angular distributions to fit the results of the first stage. In the remainder of the present chapter, the first stage will be described. The second stage pertaining to simulations will be described in detail in Chapter 7.

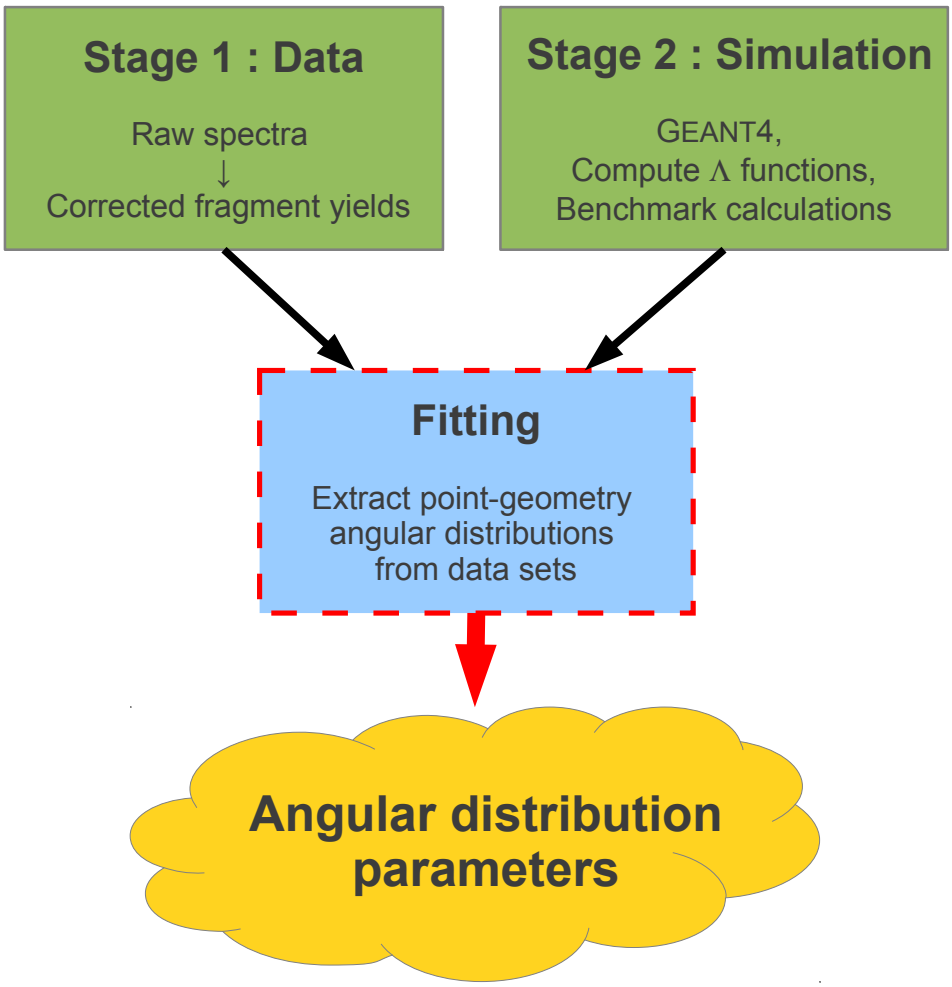

Figure 6.1: The flow chart of the full analysis procedure. The results of two separate analysis stages (green) are requisite for the execution of a fitting procedure. The fit results are parameter values with errors that define the angular distribution.

6.2 The Data

It is informative to expound on the format and information that the data comprise prior to discussion of the analysis details. The digitized signals following signal processing are stored event-wise in the CODA evio file format and then subsequently

converted into a ROOT tree data structure by the TUNL-developed CODA2ROOT program. The ROOT format was chosen, because it enabled the use of powerful analysis tools included in the ROOT framework [66] and improved the data-storage economy.

Each event contains data from at least the ADC and TDC associated with the strip responsible for triggering the event acquisition. The ADC data directly represents the peak-height of the detector signals, which for Si detectors is related to the energy of the incident particle. In addition to the ADC data, the TDC was used to produce self-timing peaks. These are structures in the TDC spectra that ideally should be characterized by a single sharp peak whose location in the spectrum is determined by a fixed delay. The self-timing peaks were used to generate time-of-flight (TOF) data when the beam pickoff monitor (BPM) was in the data stream, which was not true for all the data. The TOF for the i^{th} Si strip was generated by

$$\Delta t_i = t_{bpm} - t_i, \tag{6.1}$$

where t_{bpm} and t_i are the elapsed times for the BPM and self-timing peak of the i^{th} strip from the common start.

6.3 Data Reduction

The structures within each ADC spectrum, see Figs. 6.2 and 6.3, are the result of a few primary processes: alpha decay, Compton scattering, and photofission. Both of the targets are unstable to alpha decay and thus are intrinsic sources of radiation. In fact,

these targets contain products of their own respective decay chains that contribute both alpha particles and beta-emitted electrons. The most energetic radiation produced in the ^{238}U target are 7.88 MeV alpha particles from the decay of ^{214}Po. The ^{232}Th target emitted radiation from the thorium decay chain with energies up to 8.96 MeV from ^{212}Po. Though the energies of the alpha decays are fixed, the energies of the alpha particles upon reaching the SSDs can range down to zero. This results from the fact that the entire target volume is a potential location for decay to occur. Because the ranges of the alpha particles are less than the thickness of the target, they can lose up to their full energy depending upon the depth at which they originated. The Compton-scattered electrons were produced in the irradiated target with energies at or below the γ-ray beam energy. The strips at forward angles are more affected by these background counts, because the cross section is forward peaked, as described by the Klein-Nishina equation. The fragments produced in photofission had energies up to nearly 100 MeV. However, regardless of the kinetic energy of the fragment, the energy it deposited in the SSD was dependent upon the distance it had to travel prior to escaping the target. For this reason, the fission fragments span the entire range of the ADC spectra, see Fig. 6.2.

The fragment events were isolated from background by one primary energy threshold. It is just above the energy of the most energetic alpha group from the respective decay chains. In the case of ^{232}Th, the alpha decays produced a clean set of plateaus that were used to calibrate the spectra, see Fig. 6.3. A four point calibration, see Table 6.1, aligned the ^{232}Th spectra such that an energy threshold could be applied

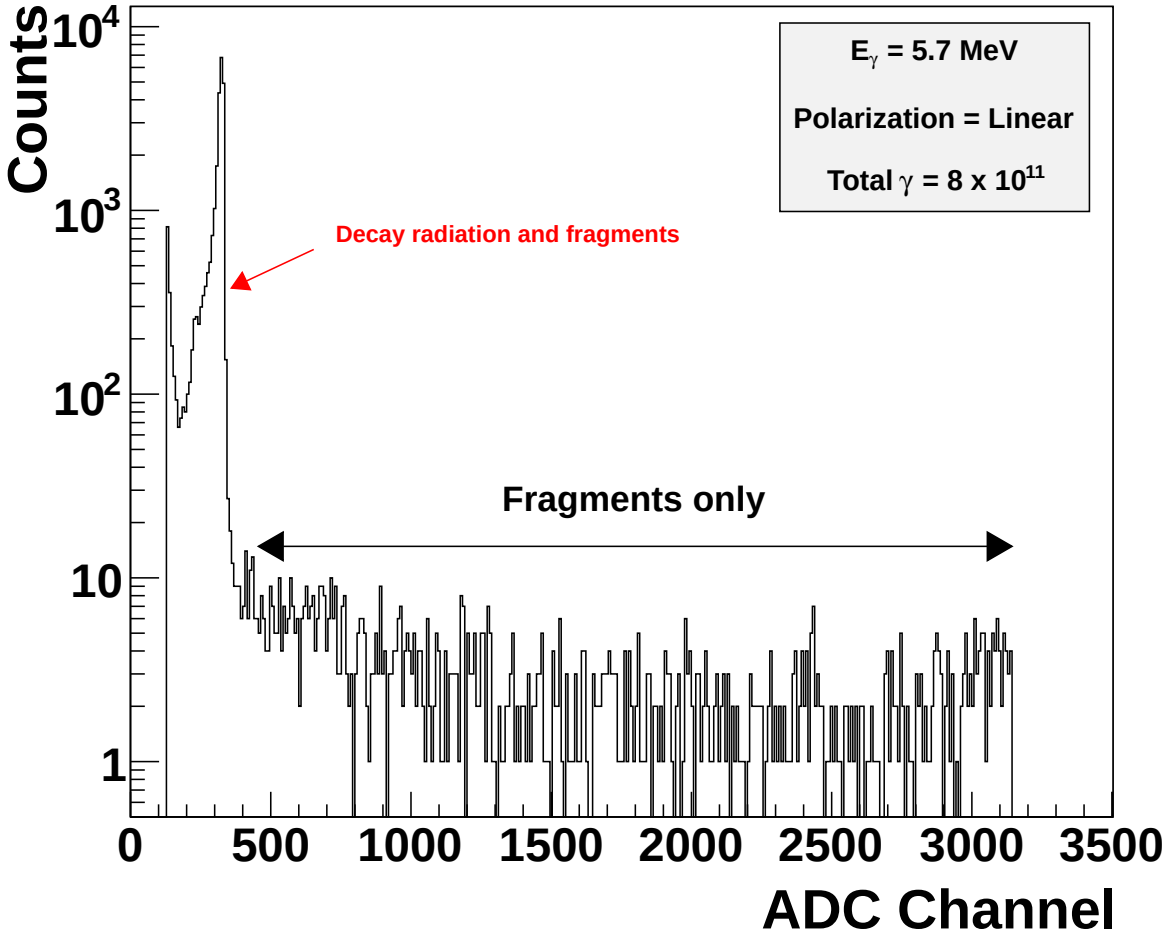

Figure 6.2: A sample ADC spectrum showing the presence of low energy structures that are the result of detected alpha particles, electrons from Compton scattering, and the fragments.

consistently. To ensure that the yields were purely the result of fission fragments, a conservative threshold was used such that only fragments depositing over 14.3 MeV alpha-particle equivalent energy were integrated. The alpha decays included in the ^{238}U decay chain are not as well spaced in energy as those in the ^{232}Th decay chain, and are therefore unsuitable for use as a set of calibration points. Instead, the abrupt end of the alpha-decay spectrum in the ^{238}U data served as a suitable threshold. It

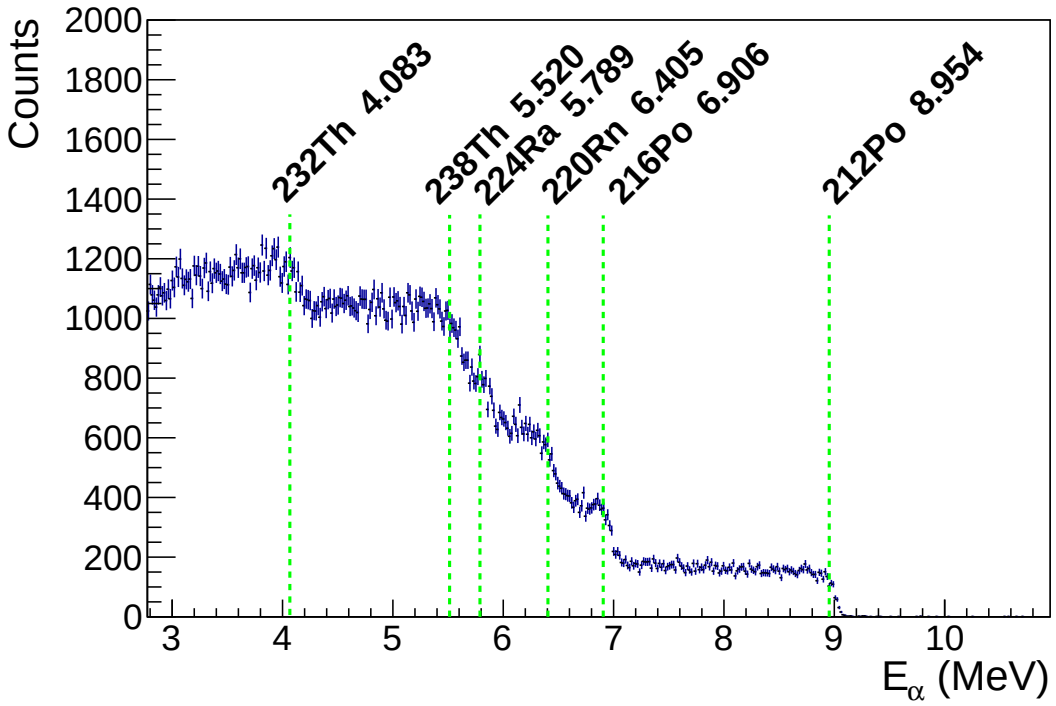

Figure 6.3: The alpha-decay spectrum of the ^{232}Th decay chain measured in the absence of the photon beam. Select alpha decays have been labeled by their parent nucleus and the energy of the emitted alpha particle in units of MeV. The abscissa has been calibrated using the four lines at 4.083 MeV, 6.405 MeV, 6.906 MeV, and 8.954 MeV. The spectrum consists of a series of plateaus because the alpha-particle energy degrades while it travels through the target before detection.

Table 6.1: The four alpha decays used to calibrate the low energy ^{232}Th spectra. Each of these energies corresponds to a plateau in the ADC spectrum.

Energy (MeV)	Parent Nucleus	Decay Mode	Half Life (s)
4.083	^{232}Th	α	4.43×10^{17}
6.404	^{220}Rn	α	55.6
6.906	^{216}Po	α	0.145
8.955	^{212}Po	α	2.99×10^{-7}

is estimated that the uncertainty introduced by the location in the threshold in each detector is less than 5%.

Because of the high energies of the detected fission fragments, the treatment of signals beyond the maximum range of the ADC was a concern. ADC spectra produced by three out of four SSDs contained events whose maximum nonzero channels were near the end of the ADC range, while one was well below, see Fig. 6.2. The Caen V785 was set to store over-range events in an overflow bin for a subset of these runs and no events were ever stored in it. A worst-case-scenario estimation of unstored ADC overflow events has been made using the simulation discussed in Sect. 5.7. The simulated energy spectrum for each strip was used to determine the number of fragments that could potentially have exceeded the range of the ADC. The lower limit for the integration region was determined as the upper limit of the calibrated ADC spectra in terms of the alpha-equivalent energy. It is estimated in this way that the average fraction of events that could have exceeded the upper limit of the ADC range was 22% for the worst detector. The effect is likely smaller than 22%, because the calibration of the ADC was in alpha-equivalent energy. It is known that fission fragments of equivalent energies to alpha particles impinging on a Si detector produce signals that are reduced in magnitude

in comparison to the alpha particles. The consequence is that the upper end of the calibrated ADC spectrum corresponds to a fragment energy greater than was used in these estimations. Therefore, the effect is expected to contribute at the level of at most 10%.

6.4 Live Time Fraction Correction

Inherent in any DAQ that digitizes analog signals for storage on a computer is a potential dead time. Because this introduces the possibility for a fragment to impinge on a strip and the DAQ ignore it, it is important to normalize the number of detected fission events for the time fraction that the system was actually accepting data, the live time fraction (LTF). The alpha particle spectrum of the target was used to correct for this since it is a constant source of events regardless of the beam characteristics or the energy. A key ingredient to this procedure is the calculation of the alpha-particle detection efficiency for each of the strips. GEANT4 simulations were used for this purpose and will be discussed in greater detail in Sect. 7.4.

The LTF was calculated for any given ^{232}Th spectrum using the following form

$$\mathrm{LTF} = \frac{\mathcal{Y}^{\alpha}}{A\Delta t \int_{4\pi} \Lambda^{\alpha} d\Omega}, \tag{6.2}$$

where $\mathcal{Y}^{\alpha}$ is the number of experimentally detected alpha particles between 7.1 and 9.0 MeV, A is the alpha activity of the target, Δt is the duration that the associated data were collected, and Λ^{α} is the probability that an alpha particle deposits an energy

between 7.1 and 9.0 MeV in a strip. In this equation, the integral of Λ^{α} over all solid angles was computed by GEANT4 following geometrical optimizations. The target activity was never used because it is absorbed into the normalization of the parameters resulting from the fitting process to be discussed in Sect. 7.2. These corrections were completed prior to combining all data runs that share the same beam configuration. Ultimately, the corrections are strip-specific and correspond to the quality of agreement between the GEANT4-simulated yields in each strip and those measured. An optimization carried out to ensure the accurate reproduction of these alpha particle yields by the simulation is described in Sect. 7.4. The largest LTF values were at backward angles and were approximately 30%. These were associated with strips that were hardest to reproduce with the simulation. The LTF values for strip yields around $\theta = 90^{\circ}$ were less than 10%.

6.5 Results

Once the data have been integrated, background subtracted, calibrated, and corrected for the LTF, they are ready for fitting. At this point in the analysis some observations are worthwhile. The plotted fragment yields, see Fig. 6.4, are the first ever to be measured using both polarized and nearly-monoenergetic photon beams. The reader is cautioned about interpreting the details of the plots as resulting solely from the (γ, f) angular distribution, because the effects of fragment straggling are still present. The fitting procedure enables the proper accounting of the effects and recovery

of the underlying asymmetry that gives rise to these effects and will be discussed in Chapter 7.

With regard to Figs. 6.4 and 6.5, two clear, meaningful observations are limited to gross features. First, the asymmetries in the ϕ direction are substantially large, upwards of a factor of 6, and are clearly the result of beam polarization, see Fig. 6.5. This can be stated because of the difference between the circularly-polarized and linearly-polarized data sets acquired at $E_\gamma = 7.6$ MeV. The only difference between these was polarization of the photon beam. Secondly, the magnitude of the asymmetry increases with decreasing photon energy. It is not surprising that this is the case because the asymmetry with respect to the polar angle also exhibits the same behavior. One interesting feature, though, is that despite this trend, there is little change between the magnitude of the asymmetry at 6.2 MeV and 5.9 MeV photon energies.

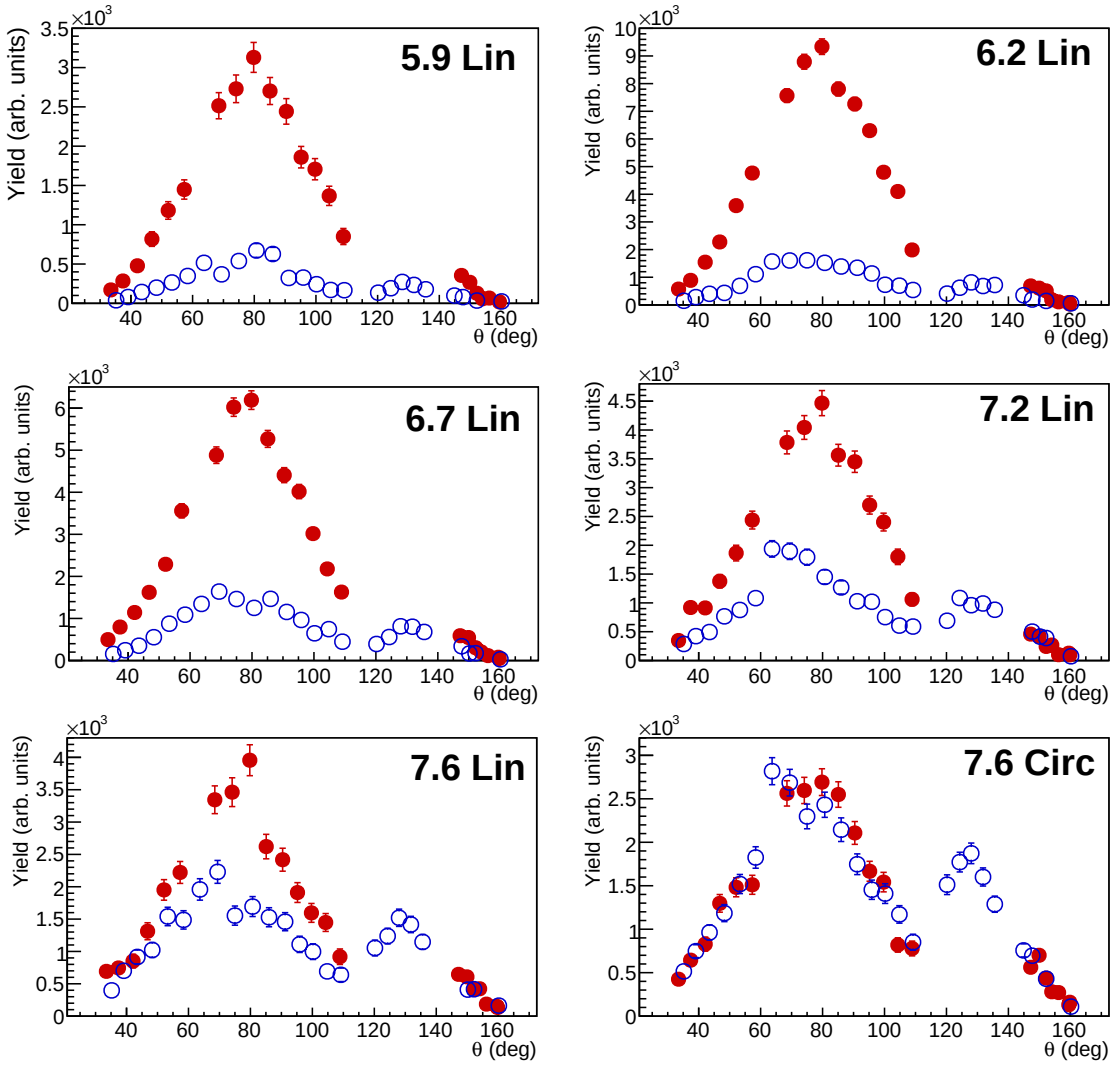

Figure 6.4: The corrected fragment yields from ^{232}Th at all energies measured. The yields detected by detectors positioned in the plane of polarization (solid circles) are compared to the yields detected by detectors positioned in the plane perpendicular to it (empty circles). The differences between the yields at each θ angle are direct indications of the large polarization-dependent asymmetry of photofission. The error bars plotted in the graph are the result of statistical uncertainties only. These are the yields that were fit for extraction of the FAD parameters using the procedure to be discussed in Sect. 7.2.

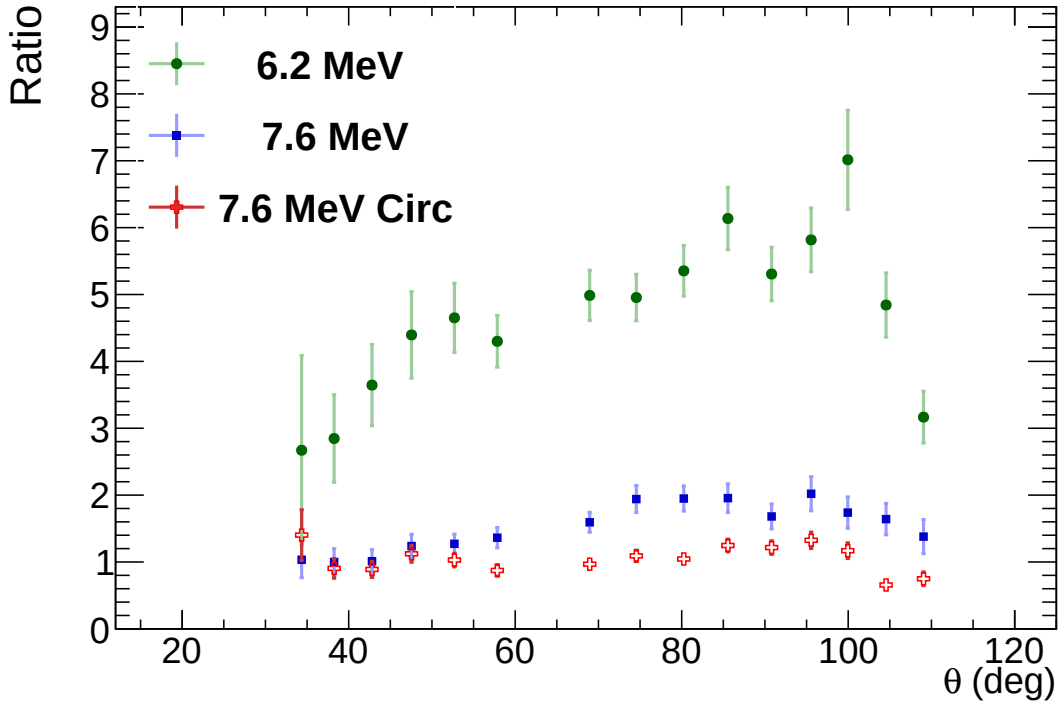

Figure 6.5: Ratios of fragment yields detected in paired Si strips as a function of the θ angle. These show the clear asymmetry with respect to ϕ that is present in the ^{232}Th angular distribution.

Chapter 7

Analysis II

7.1 Overview

The second integral component of the analysis procedure was the calculation of the effect on the angular distribution of fragment straggling within the target. Since the SSDs registered fragments following modification of their original trajectories by the energy loss process, it is imperative to have a good understanding of these effects. Computation of probability distributions describing these was heavily dependent upon the GEANT4 tool-kit and was geared toward producing results aimed for use in a fitting procedure. For the latter reason, the discussion of these calculations will be framed in the context of the fitting procedure. First, the fitting algorithm will be described in Sect. 7.2 to motivate the need for the probability distributions, and then the specifics of their calculation will be explained in the remainder of the chapter.

7.2 Fitting procedure

The experimental yields have been fit using a detailed χ^2-minimization procedure. For every strip, the observed yield is the result of the following integral

$$\mathcal{Y}_i = N_t \phi \epsilon_i \int_{4\pi} \frac{d\sigma}{d\Omega}(\theta, \phi) \Lambda_i(\theta, \phi) d\Omega, \tag{7.1}$$

where N_t is the number of target nuclei per unit area exposed to the photon beam; ϵ is the efficiency of detection, which is known to be 100%; $d\sigma/d\Omega$ is the differential cross section; and Λ_i is the marginal probability that a fission fragment is detected if its trajectory is defined by θ and ϕ. The differential cross section can be written in the form derived with the channel formalism, see Sect. 3.1, as

$$\begin{aligned} \frac{d\sigma}{d\Omega} &= \sigma_{tot}\, W(\theta, \phi) \\ &= \sigma_{tot}\, \left(a + b \sin^2(\theta) + c \sin^2(2\theta) + \omega \cos(2\phi) \left[d \sin^2(\theta) + c \sin^2(2\theta) \right] \right). \end{aligned} \tag{7.2}$$

An equivalent but different parameterization based on spherical harmonics, Y_{lm}, has been used as well since the orthonormality of these functions makes them optimal for fitting. It is expressed as

$$\frac{d\sigma}{d\Omega} = \sigma_{tot} \left(c_{00} Y_{00} + c_{20} Y_{20} + c_{40} Y_{40} + 2\omega \cos(2\phi) \left[c_{22} \sqrt{\frac{5}{96\pi}} P_2^2 - c_{40} \frac{1}{16\sqrt{\pi}} P_4^2 \right] \right), \tag{7.3}$$

where associated Legendre polynomials are indicated by P_l^m. Conversion from the pa-

rameters in Eq. 7.3 to the standard parameterization of Eq. 7.2 is through the following system of equations,

$$\begin{aligned} a &= \frac{1}{\sqrt{4\pi}}\left(c_{00} + \sqrt{5}c_{20} + 3c_{40}\right) \\ b &= -\frac{3}{16}\sqrt{\frac{5}{\pi}}\left(4c_{20} + \sqrt{5}c_{40}\right) \\ c &= -\frac{105}{64\sqrt{\pi}}c_{40} \\ d &= \frac{1}{16}\sqrt{\frac{15}{2\pi}}\left(8c_{22} + \sqrt{30}c_{40}\right) \end{aligned} \quad . \tag{7.4}$$

In Eqs. 7.2 and 7.3, the differential cross section has been separated into the total cross section σ_{tot} and a purely angle-dependent function. The Λ_i function in Eq. 7.1 is a strip specific probability distribution accounting for the escape probability of the fragment from the target and the finite geometry. The specific meaning of the integrand is as follows. The differential cross section is the probability density function that specifies the probability that a fragment is generated with a direction specified by θ and ϕ. The Λ_i function is the conditional probability density function for the event that a particle deposits at least an energy E_{min} in detector i given a specified trajectory. It can be decomposed as

$$\Lambda_i(\theta, \phi) = \eta(\theta, \phi)h_i(\theta, \phi), \tag{7.5}$$

where η is the probability that a fragment escapes the target with at least E_{min} and h is the conditional probability that a fragment stops in detector i. It is important to note that the θ and ϕ in these equations correspond to the initial trajectory of a fragment, i.e., before its trajectory can be altered by straggling. Given knowledge of

the Λ_i functions, the parameters of the angular distribution can be extracted from the fitting results.

The fitting routine sought to minimize the χ^2 value, which is defined as

$$\chi^2 = \sum_i \left(\frac{\mathfrak{Y}_i - Y_i}{\sigma_{Y_i}} \right)^2 . \tag{7.6}$$

Here the Y_i and σ_{Y_i} are the corrected fragment yields and their associated uncertainties formed in the first stage of the analysis, respectively. The calculated yields are indicated by $\mathfrak{Y}_i$ and are defined as

$$\mathfrak{Y}_i = \int_{4\pi} W(\theta, \phi) \Lambda_i d\Omega. \tag{7.7}$$

This is merely the integral portion of Eq. 7.1. The minimization of Eq. 7.6 is accomplished by varying the c_{lm} parameters in Eq. 7.3 so the result of this procedure is a set of parameters associated with the minimum χ^2 value. Ultimately, only the relative magnitude of these parameters is of interest for the present work.

7.3 Monte-Carlo Calculations

7.3.1 θ and ϕ Determinations

Determination of the solid angle acceptances for each strip was complicated for a few reasons. The first was the finite size of the intersection volume of the beam with the target. Fission events were able to occur at any point within this region and thus the acceptance region of a strip could vary significantly depending on the location

where the fission event occurred. This effect was accentuated by the close proximity of the beam axis to the detectors, which was 3.5 cm from the axis to the center of the active region of the detector. The second complication resulted from geometry of the strips themselves. The strip shapes were not optimized to be used in the target-detector geometry of the current project. The curvature of each strip introduced a ϕ dependence into the θ acceptance width. Finally, shadowing effects that resulted from the target mount effectively reduced the acceptance region of some strips in the downstream bottom detector.

A GEANT4 simulation was used to account for these effects as well as to compute an effective θ and ϕ for each strip. The original trajectory of each simulated particle, rather than the effective trajectory computed from its global displacement, was used in the calculation. For each strip, the calculation averaged the set of θ and ϕ values that produced an event and then assigned one standard deviation for the uncertainty. These values are tabulated in Appendix C.

7.4 Simulated Geometry Optimization

As discussed in Sect. 5.7, the straggling of fragments within the target prior to detection substantially distorts the form of the detected angular distribution. Knowledge of the precise geometry is essential to producing the proper corrections. But because the experimental geometry is complicated and the minimalistic design of the target mount introduces uncertainty to the target position, an optimization procedure was

carried out to ensure that the simulated geometry, with which the corrections were calculated, properly included all minor details of the actual geometry. The need for these optimizations was enhanced by the close target-detector geometry, which amplified the effect of any geometrical imperfections.

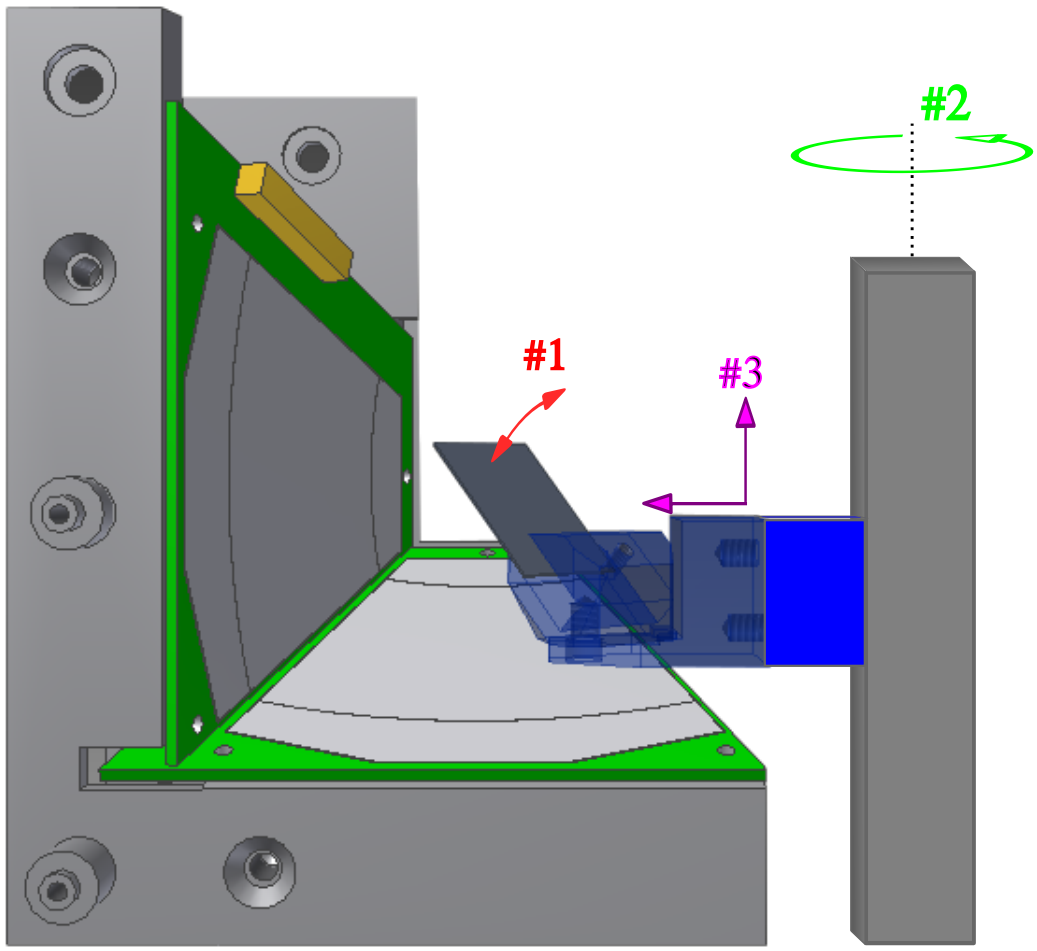

Figure 7.1: The three adjustments to improve the geometrical model of the experimental setup are numbered. Adjustment 1 is the inclination angle of the target, adjustment 2 is a rotation about the point the target mount assembly was affixed to the chamber, and adjustment 3 is the translation of the target relative to the SSDs.

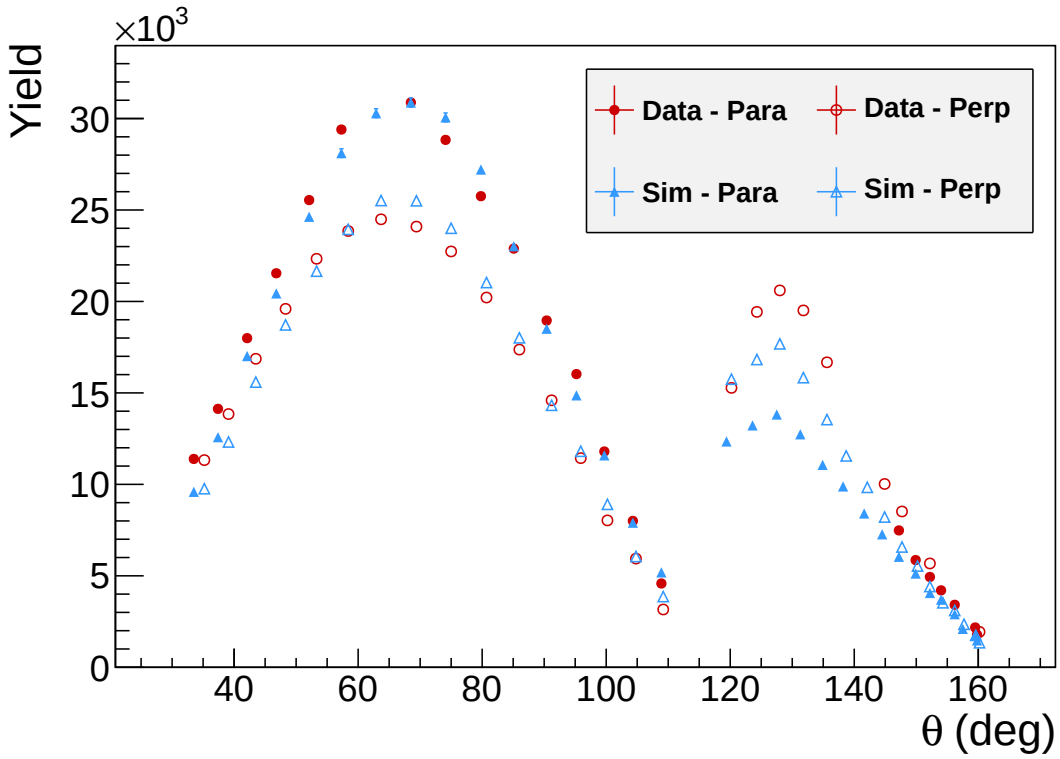

Figure 7.2: Comparison of alpha particle yields as a function of polar angle as predicted by GEANT4 and as measured in the absence of the photon beam. The data points labeled "para" are associated with the detectors at $\phi = 0°$ and $\phi = 180°$, because they lie in a plane parallel to the polarization plane. Those labeled "perp" are associated with the detectors lying in a perpendicular plane, $\phi = 90°$ and $\phi = 270°$. The target has been adjusted in the manner discussed in Sect. 7.4.1 to produce these results. The data associated with angles less than and greater than 110° correspond to the SSD pair at forward and backward angles, respectively.

7.4.1 Relative Target-to-Detector Position

The optimization was aimed at establishing the correct, relative target-to-detector position. In doing so, three real, physically-realizable adjustments, see Fig. 7.1, were employed as the parameters. The first and most sensitive was a variation in the inclination angle of the target. The second adjustable parameter was the rotation angle of the target about the symmetry axis of the bolt securing the target mount to the chamber;

this axis was parallel to the surface normal of the floor. The final parameter was a shift in the position of the target center of mass with respect to the detectors. As a guiding principle, adjustments were only varied within the uncertainty of the experimental geometry.

Any optimization requires a benchmark to use as a comparative reference. In this optimization, the experimentally measured yields for alpha particles that deposited energies between 7.1 and 9.0 MeV into a Si strip were used. In the experiment, these alpha particles were the result of ^{212}Po alpha decays that released 8.96 MeV of energy. The bounds of the integration region were chosen because the aforementioned decay was the only process that could generate alpha particles capable of depositing energy into the Si strips within the range it defined. A comparison could then be made between these data and the resulting yield shape produced by a simulated monoenergetic source of 8.96 MeV alpha particles. For the selection of the optimal geometry, the results of the simulation were scaled by a constant such that the summed, squared difference between the simulated yields and the data was minimized. The target geometry that minimized the difference was used in the analysis. In the simulation, as in the experiment, the alpha particles were emitted from all sides of a ^{232}Th target.

Good agreement was found with the benchmark data by increasing the inclination angle of the target in the simulation by 5°, rotating about the bolt by 1°, and shifting the target 1 mm towards beam-left, see Fig. 7.2. Adjustments were relative to the target orientation of a perfectly positioned target rotated twice by 45° and a holder that was perpendicular to the beam direction. These adjustments are well justified by

either photographic or written documentation of the experiment. In a sense, they are a measure of the ability of the experimenter to position the target using the current mounting system. The rotation about the bolt corresponds to a rotation that is in the same direction as is required to tighten the bolt. Given these adjustments, the agreement is within 10% at angles near $\theta = 90°$ and at most 30% for backward angles that were the most difficult to reproduce, see Fig. 7.2.

7.4.2 Λ probability distributions

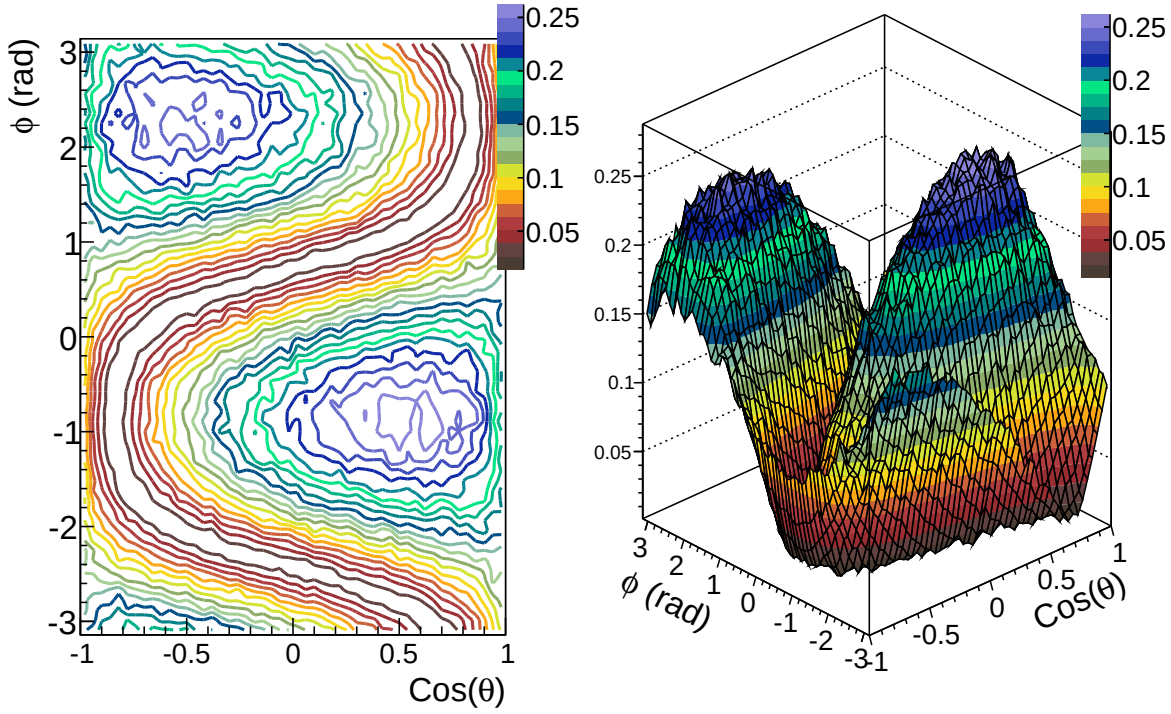

Figure 7.3: A contour plot (left) and surface plot (right) of the marginal η function corresponding to 75.0 MeV ^{130}Xe nuclei created in the ^{232}Th target. The z-axis is the probability per 5×10^{-4} sr that the particle escapes the target with energy greater than $E_{min} = 14.3$ MeV if it originated within less than 10 μm from the surface. The curved valley shape defines the plane of the target.

The pseudo-data produced by the GEANT4 simulations were exhaustive, and a detailed list of the information stored in a hit can be found in Appendix D. The η and h_i distributions comprised by Λ, as discussed in Section 7.2, were computed using these data. Both distributions are dependent upon the A and Z of the simulated particle and its detected energy. In essence, the computation of η and h amounts to a sorting process followed by proper normalization. The sorted data were stored in the ROOT file format in a directory structure whose major divisions were according to the A and Z of the simulated particle. Within each isotope directory, the remaining data were stored as multidimensional histograms to preserve their correlations.

The η function was stored as 3-dimensional histograms whose axes corresponded to the initial $\cos\theta$, ϕ, and depth from the closest surface of the target. The useful form of the η function is not in its most decomposed state, but rather as the marginal probability distribution following the summation over A, Z, and depth, since that is how it appears in Eq. 7.1. This was computed and normalized so that integration of the marginal η function over all solid angles yielded the total probability that any fragment generated within the target could escape with an energy greater than E_{min}. These energy thresholds were set to 7.9 MeV for ^{238}U and 14.3 MeV for ^{232}Th for reasons described in Section 6.3. The marginal η function, properly normalized and associated with a 75.0 MeV ^{130}Xe fragment, is shown in Fig. 7.3. The η function in Fig. 7.3 is representative for all fragments, since the major differences between them is the magnitude of the probability; the shape of the distributions does not vary.

The h_i functions were stored as 2-dimensional histograms with axes corresponding

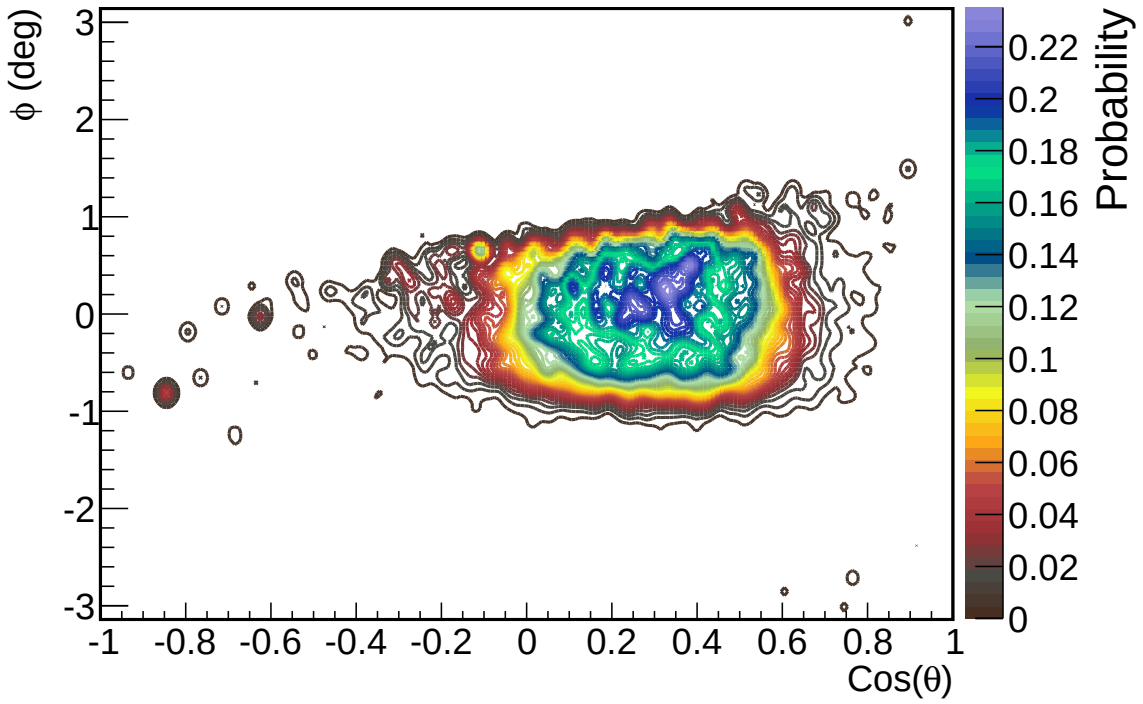

Figure 7.4: The h function for the Si strip located at $\theta = 72°$.

to $\cos\theta$ and ϕ. Because each histogram corresponded to a specific strip, 64 histograms were stored in each isotope directory. These defined the probability that a fragment deposits greater than E_{min} for the specified target. These probabilities are determined primarily by the geometry of the target-detector assembly and were calculable using an isotropic angular distribution. When included in the Λ function, they define the effective integration region for each strip, see Fig. 7.4.

7.4.3 Charged Particle Transport Validation

It was mentioned that the measured angular distributions were heavily influenced by the straggling of the fragments in the target. Corrections applied to account for this

effect depend heavily on the model of the charged particle energy loss. As described in the preceding section, GEANT4 has been chosen and used for this purpose. Another code called TRIM [67] traditionally has been considered the best tool available for computing the stopping of ions in matter. It was not chosen for this project because there is no way to provide it a geometry to track ions through as in GEANT4. However, a series of comparisons determined whether or not there were major differences between the two codes. Four representative fragments were chosen, two from the light group and two from the heavy group, as well as 9.0 MeV alpha particles. The fragments tracked through the simulation of the ^{232}Th were also given the same initial energy that would be assigned to them should they have been simulated. The simulation that calculated the Λ and h functions used the same GEANT4 physics list as these comparisons.

Even though calculation of energy loss for heavy ions is difficult, the two calculations predict the ranges to be at most different by 30%, see Fig. 7.5. The best agreement was found for the calculation of 9 MeV alpha particles for which there is essentially no difference between the two results in both the range calculation and the angular straggling, see Fig. 7.6. The reasonable agreement between the two calculations indicates that GEANT4 is equally capable of calculating the straggling effect as the traditionally accepted TRIM.

7.4.4 Robustness of Results

Section 7.4 discussed an effort to improve the fit results by making fine, physically-justified adjustments to the modeled geometry. An investigation of the robustness of the

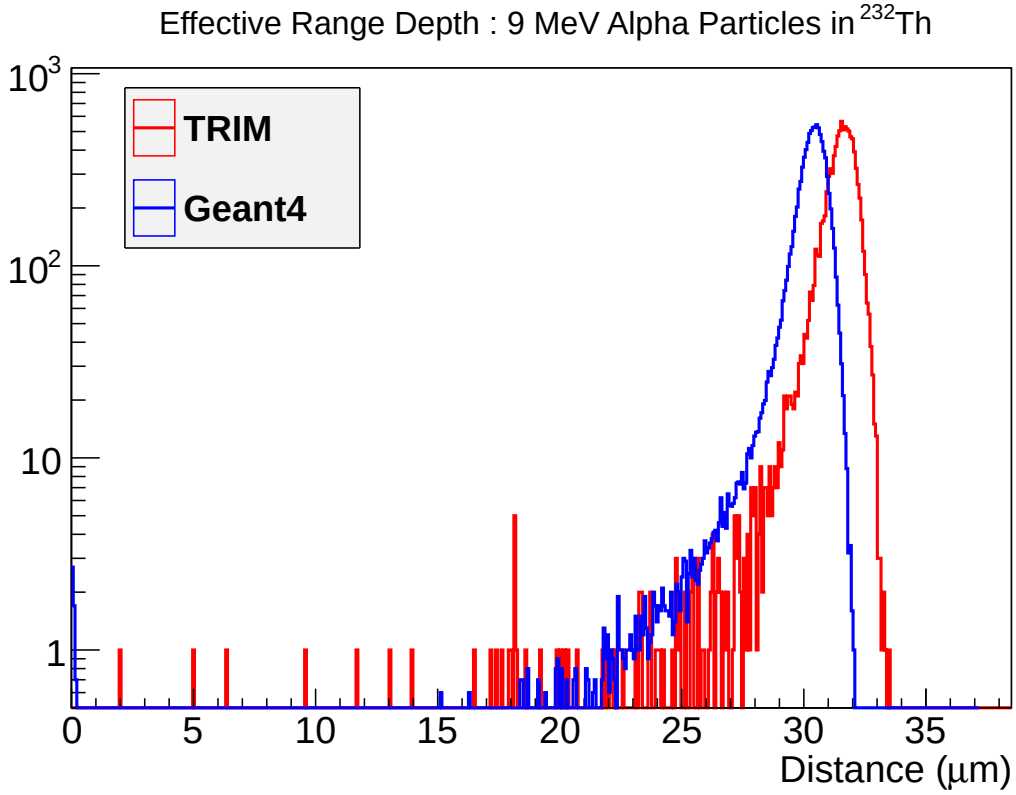

Figure 7.5: Comparison of the ranges of 9 MeV alpha particles in a block of ^{232}Th.

fitted parameters to these small changes in the geometry has been carried out. The two most sensitive adjustments, those being the two rotations of the target shown in Fig. 7.1, were varied to understand the effect on the resulting fit parameters. Table 7.1 provides quantified values of these variations. The Λ functions computed using these altered geometries were used to fit the data and the resulting parameter sets were compared. In all cases, the resulting parameters agreed within error bars. Furthermore, to ensure that the fitting algorithm found a unique minimum for each of the parameter sets, the initial parameter values were randomized. The series of fitting attempts using random initial parameter values always resulted in parameters that agreed within errors.

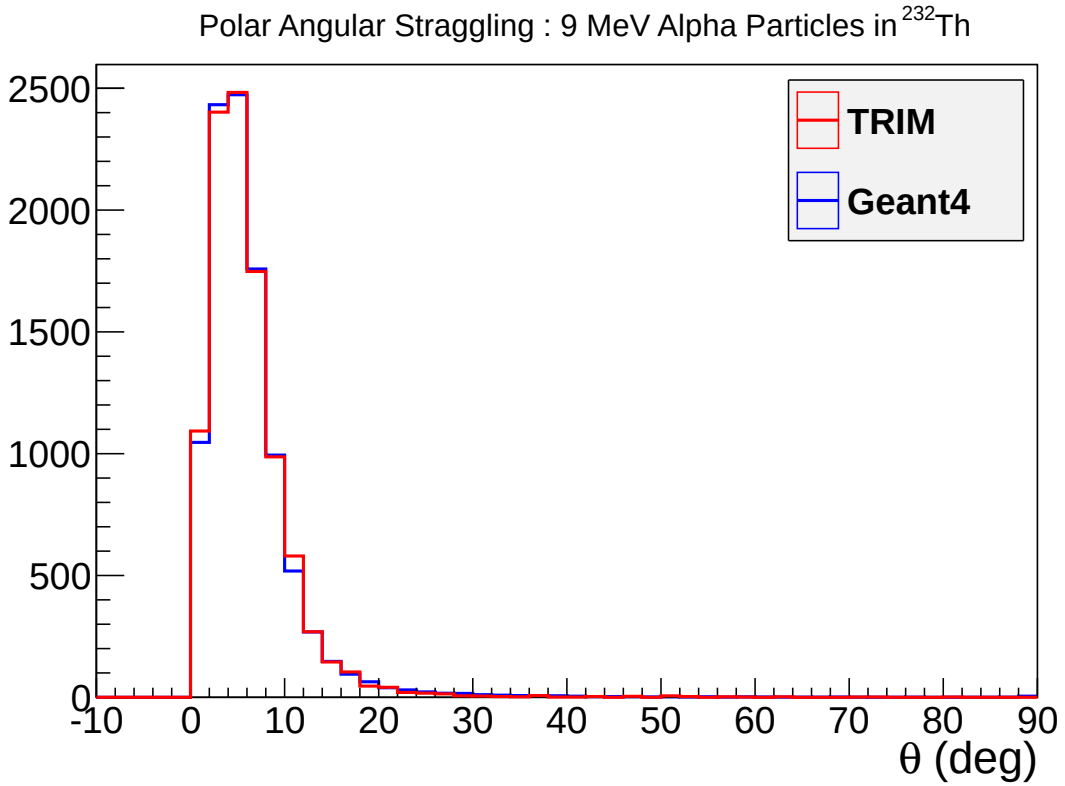

Figure 7.6: Comparison of the angular straggling of 9 MeV alpha particles in a block of ^{232}Th. The straggling is the defined as $\theta = \arctan d/L$, where d is the lateral straggling and L is the depth into the absorber that the particle travels. There is very little difference between TRIM and GEANT4.

Table 7.1: The geometry adjustments used for determining the robustness of the fit results. These variations concerned the most sensitive parameters in the geometry and are labeled #1 and #2 in Fig. 7.1.

Trial	Deviation from Final Geometry	
	rotation 1 (deg)	rotation 2 (deg)
1	+2	-2
2	+2	0

Chapter 8

Fit Results and Discussion

8.1 Fit Results for ^{232}Th

The data for ^{232}Th were fit using the procedure described in Sect. 7.2. The procedure removed finite-geometry and straggling effects that strongly influenced the form of the measured angular distribution. The resulting parameter sets therefore describe the angular distribution for point-like geometries. In this form, the parameters provide insight into the physics of the PFADs. A tabulation of the results is included for ^{232}Th as Table 8.1.

Some general features of the data will be presented before entering into more detailed discussions. These parameter sets define angular distributions characterized by large ϕ- and θ-dependent anisotropies, see Figs. 8.1 and 8.2. The largest asymmetries with respect to ϕ result from photon beams with energies below $E_\gamma = 7$ MeV. For the largest asymmetries, the yields are equivalent to zero at $\phi = 90°$ and $\phi = 270°$. As such there is at least a factor of 15 times greater emission probability for fragment trajectories lying in the plane of polarization than perpendicular to it. It is important to note that

Table 8.1: The parameter sets that resulted from the fitting procedure along with the associated reduced-χ^2 values, χ^2/ν. All parameters have been normalized such that $c_{00} = 1$. The asterisk indicates that the parameter set corresponds to data acquired with a circularly-polarized photon beam, in which case, the c_{22} parameter has been fixed to zero. Parameter errors are defined as deviations from parameter values at the minimum such that the χ^2 is increased by a value of 1.

E_γ (MeV)	c_{00}	c_{20}	c_{22}	c_{40}	χ^2/ν
5.9	1.00 ± 0.13	-0.55 ± 0.13	0.58 ± 0.10	0.13 ± 0.13	2.8
6.2	1.00 ± 0.06	-0.54 ± 0.06	0.58 ± 0.05	0.13 ± 0.06	8.1
6.7	1.00 ± 0.07	-0.47 ± 0.07	0.48 ± 0.06	0.09 ± 0.07	6.7
7.2	1.00 ± 0.09	-0.36 ± 0.09	0.33 ± 0.06	0.11 ± 0.09	5.1
7.6	1.00 ± 0.10	-0.18 ± 0.08	0.18 ± 0.08	0.10 ± 0.10	3.5
7.6*	1.00 ± 0.08	-0.17 ± 0.09	-	0.14 ± 0.12	7.5

the angular distribution is a probability distribution and is therefore only meaningful when positive, as is characteristic of the present results.

Another interesting aspect of the angular distributions is the wide minimum with respect to θ that exists at the extreme forward and backward angles, see Fig. 8.2. The angular distribution is relatively flat at these angles when the energy is low but develops a peak by the time the energy reaches $E_\gamma = 7.6$ MeV. On the other hand, the angular distribution is peaked strongly near $\theta = 90°$. The magnitude of this peak decreases with increasing photon energy and is accompanied by the rise in the aforementioned peak at extreme polar angles.

8.2 Dipole Photofission of ^{232}Th

The parameter sets resulting from this work are compared with those of previous measurements in Fig. 8.3. Because previous works reported results according to the

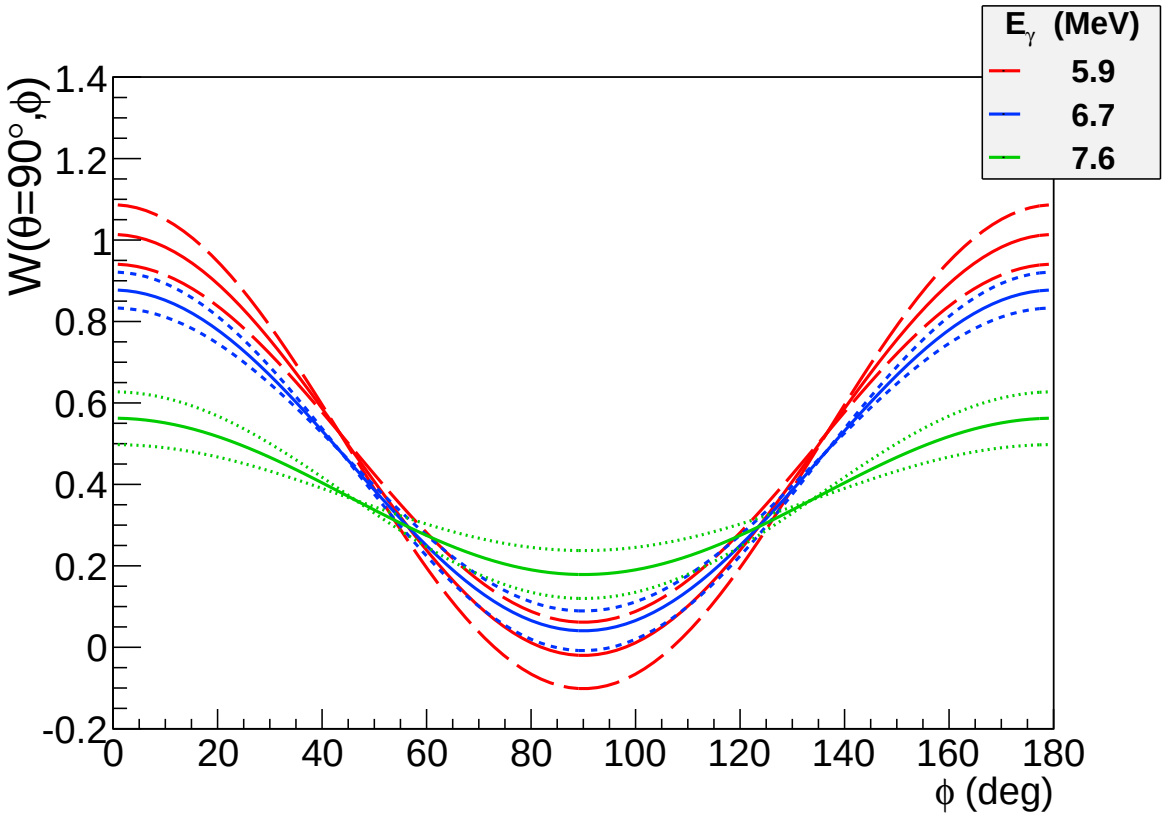

Figure 8.1: The ϕ dependence of the angular distribution is plotted for $\theta = 90°$ using data from Table 8.1. Three representative energies are included to show the decreasing magnitude of the asymmetry with increasing E_γ. For each energy plotted, there are three lines: two dashed and one solid. The dashed lines indicate the uncertainty band about the solid line.

parameterization of Eq. 7.2 and the present work used the parameterization of Eq. 7.3, the parameter values in Table 8.1 have been converted according to Eq. 7.4. It is clear that the results of the present work disagree with the previous data. However, it is stressed that this work employed monoenergetic photon beams whereas the others used bremsstrahlung beams. Consequently, the results from this thesis work are not expected to be in complete agreement with those previously measured. Furthermore, differences are expected to increase with energy because of the different energy profiles of the photon beams. The large error bars are caused by the large uncertainties of

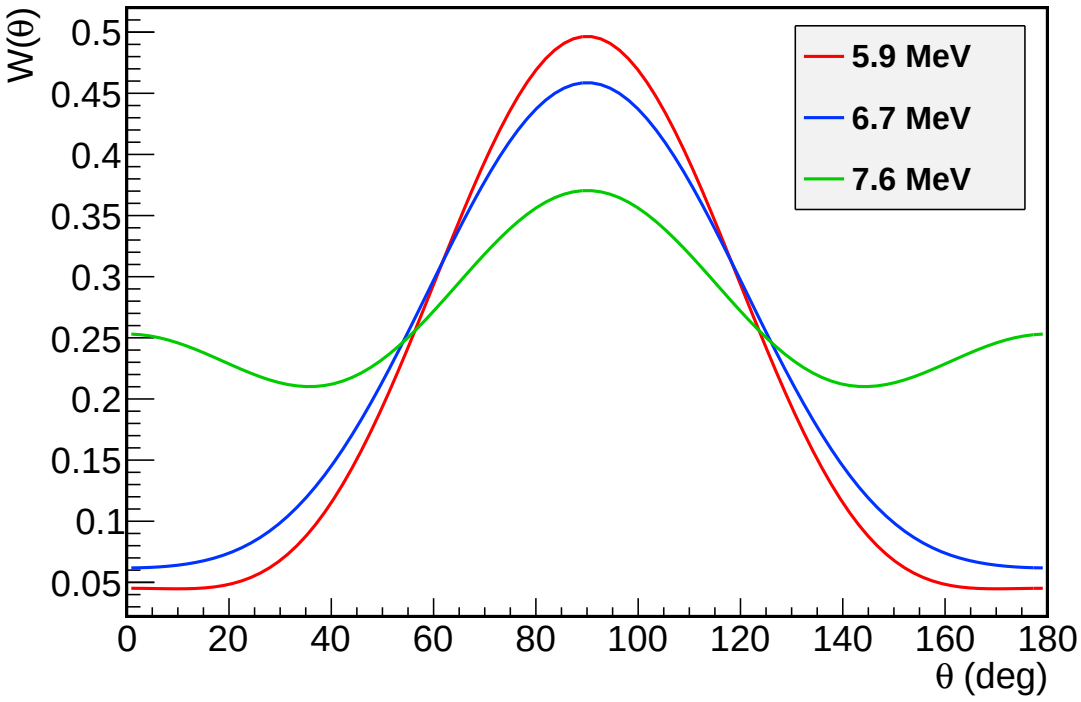

Figure 8.2: The θ dependence of the angular distribution is plotted. The ϕ dependence has been removed by integration so that this is equivalent to the angular distribution in the absence of photon beam polarization. The same parameters are used as in the Fig. 8.1.

the c_{40} parameters. According to Eq. 7.4, the c_{40} parameter errors contribute with the same significance to the a, b, and d parameters. Furthermore, the formation of ratios of values with already large uncertainties only serves to magnify the uncertainty.

It is also important to bear in mind the sensitivity of the b/a ratio to the values of the individual parameters. The large values of b/a measured by Rabotnov *et al.* [43] are the result of division by an a parameter that is nearly zero. As a approaches zero, the ratio becomes unbounded. An alternative, well-behaved value useful for comparison

is the θ-dependent asymmetry, Σ_θ, which is obtained from the b/a ratio as

$$\Sigma_\theta = \frac{W(\theta = 90°) - W(\theta = 0°)}{W(\theta = 90°) + W(\theta = 0°)} = \frac{b/a}{2 + b/a}. \tag{8.1}$$

The comparison is included as Fig. 8.4 and shows that the results are not quite as discrepant below 7 MeV as the b/a ratio might suggest. At energies above 7 MeV, the trending of the present data appears to be more consistent with the results of Winhold *et al.* [24, 36].

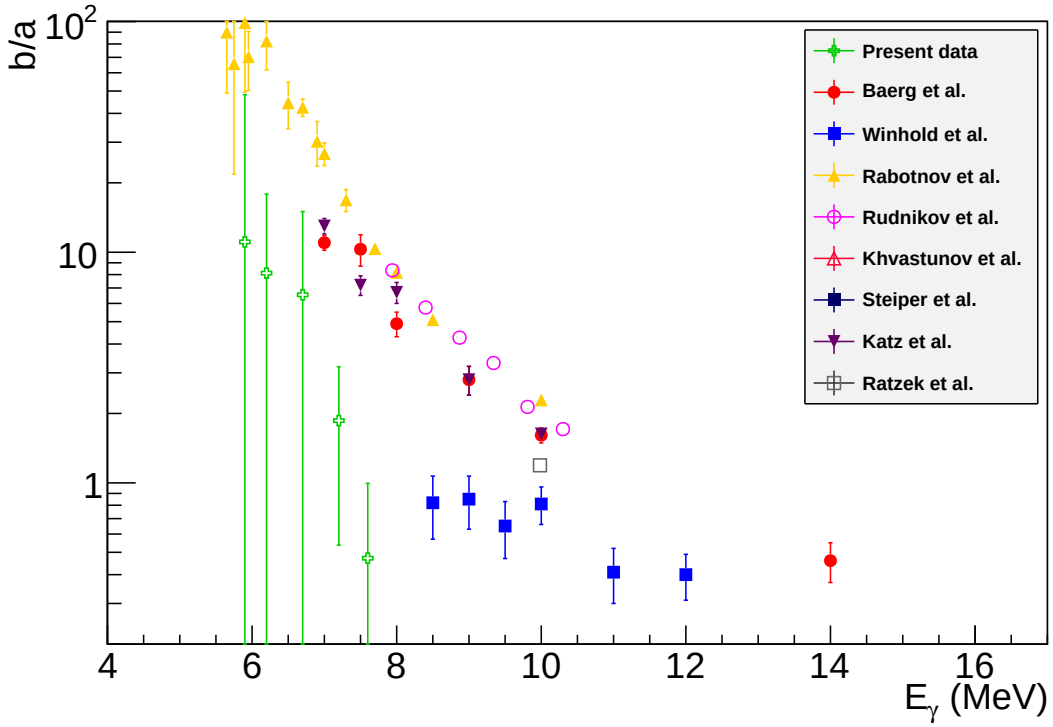

Figure 8.3: The converted b/a values of the present work are compared to previous data [24, 36, 39, 43, 48]. The results of this work (green) are the only included values that result from a nearly-monoenergetic photon beam. The others employed bremsstrahlung beams.

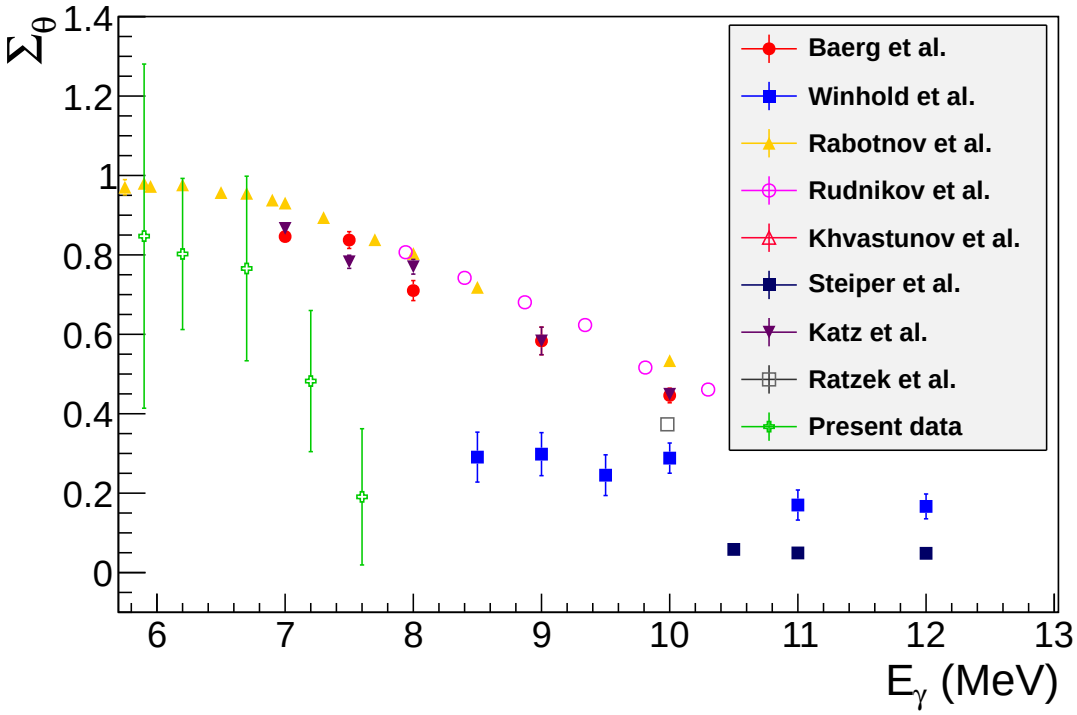

Figure 8.4: The asymmetry with respect to θ of the present work is compared to previous measurements.

8.3 Quadrupole Photofission of ^{232}Th

Previous measurements of the photofission of ^{232}Th are few, and of these, only two [43, 48] have considered the contributions of the quadrupole component, see Sect. 4.4. Both conclude from their measured c/b ratios that the quadrupole contribution to the angular distribution is small but statistically significant. The present work finds an equivalent result but cast in terms of the c_{40} parameter, which contains all of the quadrupole contributions to the angular distributions. Its energy dependence is shown in Fig. 8.5. The measured values are 10 times smaller than the c_{00} term and are characterized by large uncertainties. Further, there is little variation in the value with

respect to energy. The average value obtained by these measurements is 0.11 ± 0.04.

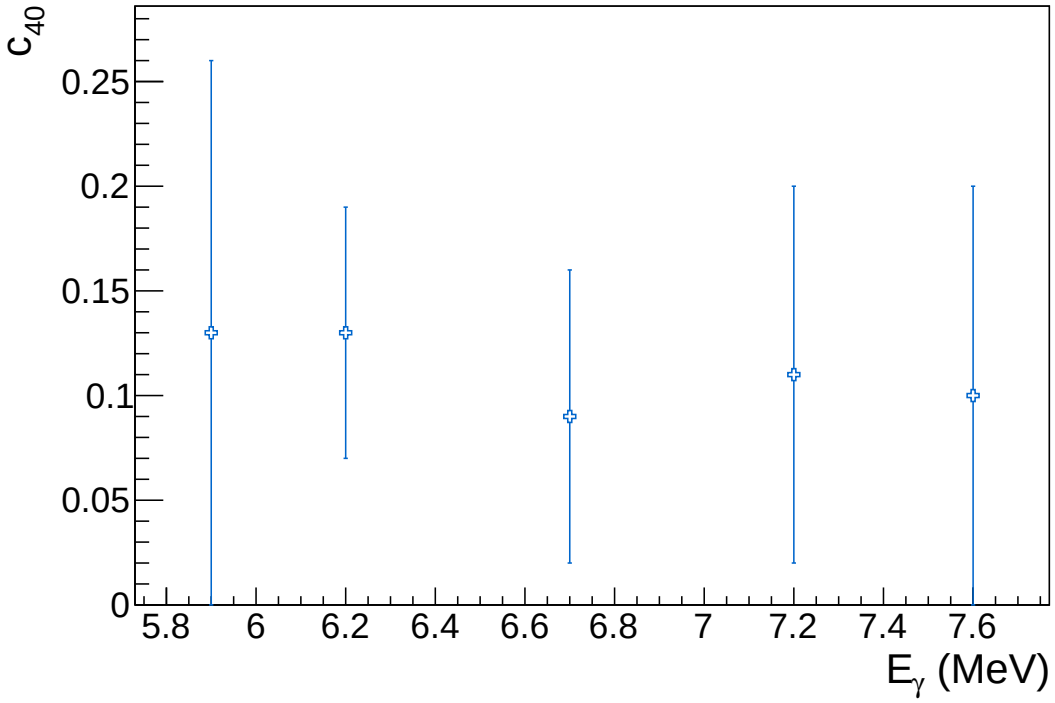

Figure 8.5: The c_{40} parameter as a function of E_γ.

8.4 Energy Dependence of Angular Distribution Parameters

As was discussed in Chapters 3 and 4, the energy dependence of the parameters contains information about the fission channels involved. The vast majority of the existing data sets were acquired using bremsstrahlung sources rather than a quasi-monoenergetic beam as was used in this work. Their sensitivity to resonant structures was, therefore, limited by comparison. Fission resonances arising from super- and

hyperdeformed states in the second and third minima have already been observed in the ^{232,234,236}U [68–70] and ^{240}Pu [71]. Their existence in ^{232}Th and ^{238}U is expected, especially for ^{232}Th for which a deep third minimum is predicted [18, 34].

Despite expectations for the existence of fission resonances in ^{232}Th, the PFAD characteristics defined by the present results do not show any strong energy dependence in the energy range between 5.9 MeV and 7.6 MeV that would be a clear indication of a resonance. The 0.5 MeV energy intervals between measurements were comparable to the full width at half maximum of the photon beam, which was approximately 400 keV. This work therefore forms a coarse scan of the energy range between 5.7 MeV and 7.9 MeV for ^{232}Th. However, this observation does not preclude the existence of a resonance, because the intensity distribution of photons has the shape of a Gaussian with skewed low-energy tail. As such, the photon beam intensity decreases away from the energy centroid, and the ability of the photon beam to excite a resonance centered at an energy intermediate to those measured during this work, for example 6.4 MeV, is correspondingly reduced. The conclusions of this work are therefore that no evidence has been found to claim the existence of fission resonances with spin 1^-, 2^+, or 1^+ between 5.9 and 7.6 MeV in ^{232}Th.

8.5 Comparison of ^{232}Th and ^{238}U

Large asymmetries with respect to the photon beam polarization were measured for both the ^{232}Th and ^{238}U . In the case of ^{232}Th, parameters capable of describing

the angular distribution were determined well by the fitting procedure with reasonable χ^2 values. The process for extracting the same quantitative information from the ^{238}U data was less successful. The fitting routine was able to produce parameter sets that minimized the reduced-χ^2 value to, at best, around a value of 30. For this reason, a qualitative comparison of the asymmetry present in the ^{238}U data is made to the ^{232}Th data by means of a ratio of ratios. The ratio of corrected yields corresponding to paired Si strips was formed independently for the FADs obtained with linearly- and circularly-polarized photon beams. Subsequently, these ratios were combined to form yet another ratio. In this way, the relative efficiencies and flux cancel to make this a comparison of like values. The only difference is the geometry of the targets which can be seen in the slight differences in the θ values to which each Si strip was sensitive. It is clear that the polarization asymmetry present in the ^{232}Th FAD is larger than the asymmetry of ^{238}U by approximately a factor of two, see Fig. 8.6.

8.6 Polarity

As was discussed in Chapter 4, this project was distinguished from all previous experiments because the photon beams it used were both polarized and nearly-monoenergetic. The fitting procedure that obtained the results contained in Table 8.1 assumed that the absorption of photons was electric in nature. This is a very reasonable assumption for a few reasons. First, the nature of electromagnetic interactions makes the probability for an M1 transition comparable to the probablity for an E2 transition. Since there is

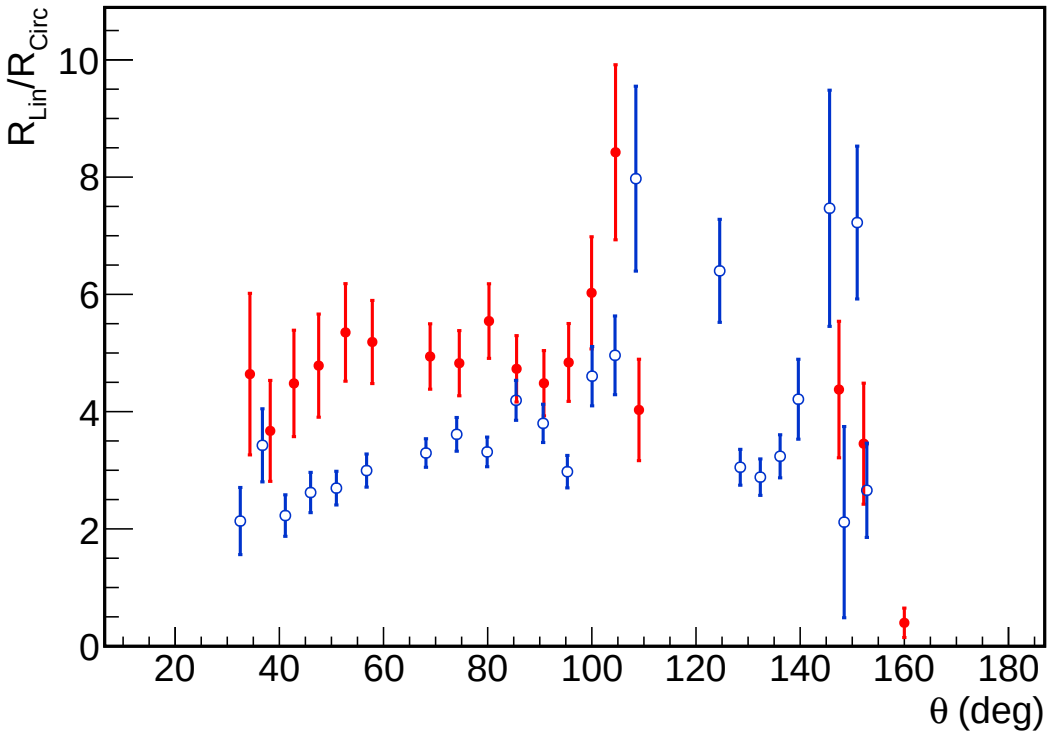

Figure 8.6: The asymmetry with respect to ϕ is shown by the ratio of ratios, R_{Lin}/R_{Circ}, described in Sect. 8.5. These are corrected yields that have not undergone the fitting process to remove the effects of finite geometry and straggling. It is clear that the ^{232}Th data (solid circles) has a larger polarization asymmetry than in ^{238}U (empty circles) at the same energy. The straggling effect at forward angles is significantly less complicated than at backward angles. The difference, therefore, is most clearly seen at forward angles.

very little quadrupole contribution in the angular distribution, one might infer that the M1 transition is also small. Secondly, the concepts presented by Bohr, see Sect. 3.1 and Fig. 3.3, advocate that 1^+ transition states do not become important until energies well above the fission barrier. In the case of ^{232}Th, the highest saddle point is computed to be between 7 and 8 MeV. The existence of a 1^+ state would then necessarily be tied to the first saddle point. Using the concepts presented by Vandenbosch [57], such a state is not expected to dictate the characteristics of the angular distribution.

8.7 Implications to Prompt-Fission Neutron Polarization Asymmetries

A major motivation for this work was the recent measurement of polarization-dependent asymmetries in the prompt-neutron angular distributions, see Sect. 4.6. A kinematical model of the prompt-neutron emission from fully-accelerated fission fragments [1] predicts the magnitude of the polarization asymmetry for neutrons if the corresponding fragment asymmetry is known. Prior to this work, the model has used the results of unpolarized PFAD measurements [43] to understand the neutron polarization asymmetry that results when a 100% linearly-polarized, quasi-monoenergetic photon beam is incident on ^{232}Th and ^{238}U. With the assumption that photofission proceeds via a pure E1 transition, the trends of the neutron polarization asymmetry as a function of E_γ have been successfully reproduced.

The scatter-plot in Fig. 8.7 compares measured neutron asymmetries [1] with the fragment asymmetries measured in this work and the work of Ref. [43]. The asymmetry is defined in terms of the b parameter following the normalization of $a + b = 1$ and the assumption of purely E1 absorption. The results of the present experiment along with the model present a consistent picture of the correlation between the neutron and fragment asymmetries, b_n and b_f. The current understanding encapsulated in the simple model is therefore a reasonably accurate description of the phenomenon. It ascribes the origin of the neutron asymmetry to the underlying anisotropic FAD. Neutrons are evaporated isotropically in the rest frame of the fully-accelerated fission

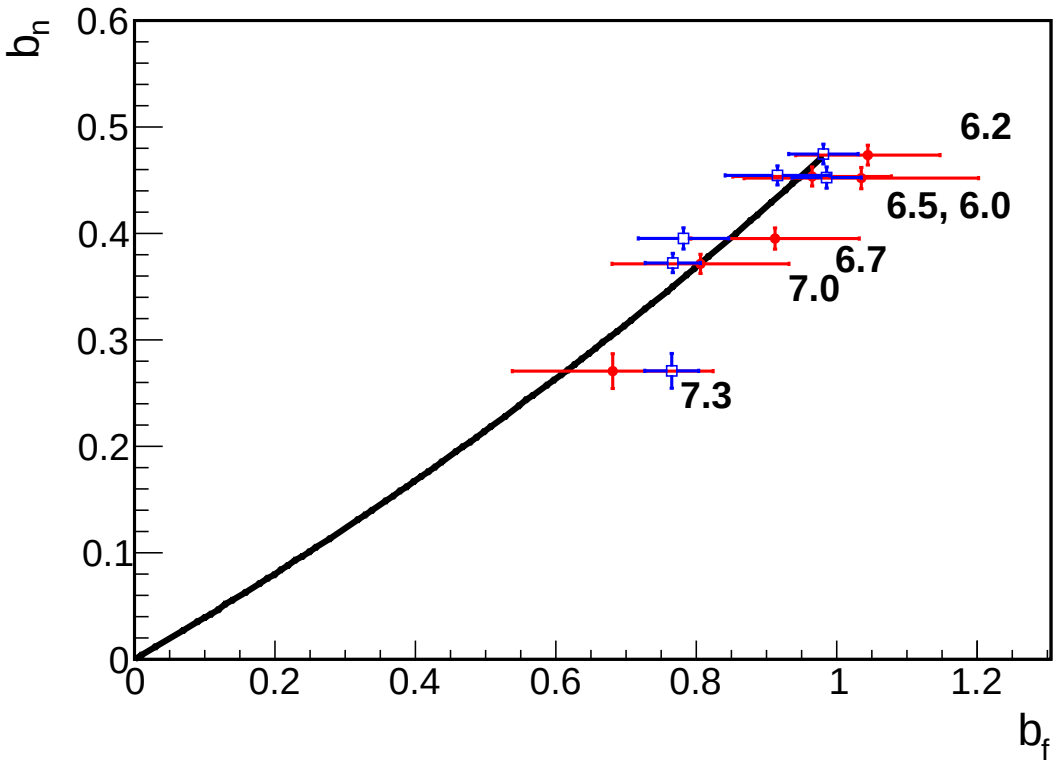

Figure 8.7: A scatter plot of the b parameters, see Eq. (7.2), characterizing the neutron and fragment asymmetries, b_n and b_f. A normalization of $a+b = 1$ was employed as was the assumption that the process is purely E1. The b_n values from Ref. [1] are combined separately with the b_f of the present data (solid circles) and the unfolded results of Ref. [43] (open squares). The energy of the photon beam corresponding to each data point is printed nearby in units of MeV. The prediction of the simple kinemetical model [1] (solid line) is also plotted.

fragments as an efficient means for deexcitation. The kinematical boost given to the neutrons from the fragment rest frame to the laboratory frame causes the neutrons to reflect the underlying fragment anistropy.

8.8 Considerations for Future Experimental Investigation

The work presented in this thesis is the first photofission experiment of its kind at the TUNL HIγS facility. It is expected that the progress made and knowledge gained during this work will assist future experiments. A few considerations are presented in this spirit.

The first and primary suggestion is to simplify the geometry of the system. There are a number of ways this could be done, and it is up to the experimenter to determine which is optimal for their experiment; each is accompanied by drawbacks. The first method, which requires the least change to the system, is to decrease the diameter of the collimator. A narrower beam would be produced that would reduce the volume in which the fragments could originate and thereby the magnitude of the finite-geometry corrections needed. The drawback would be a reduction of equal magnitude in the flux. For example, the use of a collimator with 1 cm diameter would decrease the area of the beam-target intersection by 72% and would be accompanied by the the same reduction in flux. A better-defined region in which the fragments originate would, therefore, come at the cost of increasing the time to acquire the same counting statistics by four.

The reduction of the beam-target intersection area addresses the sub-millimeter-scale sensitivity that results from the close geometry. An alternative method would be to increase the distance between the target and detectors. Such a solution requires a major modification to the existing geometry but would have a larger effect than changing the diameter of the collimator. The drawback here is a reduced detection rate caused by the smaller fractional solid-angle coverage associated with each strip. If the experimenter were interested in a smaller range of angles, the detectors could then be arranged to improve the associated counting statistics. Alternatively, more detectors would alleviate this problem at the cost of added complexity to the DAQ.

A third improvement to the existing geometry would be to engineer a more robust mount for the target. As was mentioned in Sect. 7.4, the minimalistic design made it necessary to optimize the simulated geometry. During the experiment, it was not fully appreciated that the uncertainty in the target position would influence the detected yields as much as it did. Such a procedure could be avoided entirely by improving the mounting system so that the orientation of the target is known precisely.

In a world with unlimited resources, an experiment devoid of finite-geometry corrections and minimal straggling effects could be devised and executed. However, scarcity exists and presents the great challenge of extracting meaningful information from real-world data. As such, decisions on how to use the above suggestions must be based on the available resources and goal of the experiment attempted.

Chapter 9

Conclusions

The first-ever measurements of the photofission fragment angular distributions of ^{232}Th and ^{238}U have been completed using photon beams of 100% linear polarization and a narrow energy spread. The work presented here is therefore also the first experiment of its kind completed at TUNL. The experiment was laden with significant challenges that were present at all stages. Multiple data collection efforts were completed that were each accompanied by the management of a complicated detector system and its equally complicated DAQ. In fact, the number of data channels digitized utilized a significant fraction of the communal electronics pool at TUNL. Being the first experiment of its kind, the DAQ was assembled from scratch. The data acquired were angle-dependent fission fragment yields from a thick target. To understand these, detailed modeling of the experimental geometry to calculate the large effects introduced by the energy and angular straggling of the fission fragments in the target was carried out. The results of these simulations were then subsequently used to recover the true fragment angular distributions at each energy from the raw fragment yields.

The scope of the project included various subjects of fission research of interest

today. The first of these was the investigation of fission resonances expected to exist in ^{232}Th as a result of hyperdeformed states in the third potential well. This work performed a coarse scan of the energy range between 5.9 and 7.6 MeV for observation of such phenomena in ^{232}Th. The energy dependence of the present results, however, does not suggest the enhancement of specific fission channels caused by resonant processes. Another important subject investigated is the mechanism responsible for producing polarization asymmetries in the prompt-neutron angular distributions. Using the assumption of purely dipole fission, the results of this work have been combined with the results of previously measured neutron angular distributions to compare with a kinematical model developed at TUNL. This comparison strengthens the claims that the asymmetry of the neutrons is the result of the underlying fission fragment asymmetry that accompanies it. These results provide further evidence of the large asymmetries in both θ and ϕ that increase with decreasing E_γ. These asymmetries are unambiguously the result of dipole fission events. It was observed, however, that a statistically significant contribution of quadrupole fission events is present for energies between 6.2 and 7.2 MeV. The analysis has assumed that all measured fragments have originated following an electromagnetic transition of electric character, as is customary, and has been based on the form of the angular distribution as presented in Ref. [30]. Finally, a comparison of the results of ^{232}Th and ^{238}U made at 6.2 MeV indicates the polarization asymmetry is larger in ^{232}Th than in ^{238}U, as is expected.

Appendix A

Electromagnetic Coupling to Matter

A more detailed explanation of the following can be found in Ref. [12], upon which the author has based his explanation. The transition rate between an initial state $|i\rangle$ and final state $\langle f|$ is given by Fermi's golden rule

$$\omega_{f\to i} = \frac{2\pi}{\hbar}|\langle f|\hat{H}_{int}|i\rangle|^2, \tag{A.1}$$

where $\hat{H}_{int}$ is the electromagnetic interaction Hamiltonian density. It is composed of the nuclear current density operator, $\hat{\mathbf{j}}$, and the electromagnetic field operator associated with the absorption of a photon, $\hat{\mathbf{A}}$ such that

$$\hat{H}_{int} = -\frac{1}{c}\int d\mathbf{r}\,\hat{\mathbf{j}}(\mathbf{r})\cdot\hat{\mathbf{A}}(\mathbf{r},t). \tag{A.2}$$

The field operator is expressed as

$$\hat{\mathbf{A}}(\mathbf{r},t) = \sqrt{\frac{2\pi\hbar c^2}{\omega V}}\sum_{\mathbf{k},\mu}\hat{\beta}^{\dagger}_{\mathbf{k},\mu}\mathbf{e}_{\mu}e^{-i\mathbf{k}\cdot\mathbf{r}+i\omega t}. \tag{A.3}$$

The normalization factor is for an electromagnetic field consisting of one photon with energy $E_\gamma = \hbar\omega$. The field operator connects a field $|0,0\rangle$ corresponding to zero photons to a field $|\mathbf{k},\mu\rangle$ of one photon whose wave vector and polarization are described by $\mathbf{k}$ and μ, respectively. This is accomplished by a creation operator $\hat{\beta}^\dagger_{\mathbf{k}\mu}$ whose non-diagonal matrix elements are of the form

$$\langle \mathbf{k},\mu|\beta^\dagger_{\mathbf{k},\mu}|0,0\rangle = 1. \tag{A.4}$$

Without loss of generality, the direction of the wave vector can be chosen parallel to the z-axis. With that choice, the polarization vector $\mathbf{e}_\mu$ and plane wave in Eq. A.3 can be expanded together in multipole fields of magnetic and electric nature as

$$\mathbf{e}_\mu e^{ikr} = -\mu\sqrt{2\pi}\sum_l \sqrt{2l+1}i^l \left(\mathbf{A}_{l\mu}(\mathbf{r};M) + i\mu\mathbf{A}_{l\mu}(\mathbf{r};E)\right). \tag{A.5}$$

Substitution of the expansion of Eq. A.5 into Eq. A.3 yields an extra summation over l. To simplify the notation, the treatment will focus on specific terms corresponding to $\mathbf{k}$ and μ such that

$$\hat{\mathbf{A}}(\mathbf{r},t)_{\mathbf{k}\mu} = -\beta^\dagger_{\mathbf{k},\mu}\mu\sqrt{2\pi}\sum_l \sqrt{2l+1}i^l \left(\mathbf{A}_{l\mu}(\mathbf{r};M) + i\mu\mathbf{A}_{l\mu}(\mathbf{r};E)\right). \tag{A.6}$$

Proceeding, the initial and final states are expressed in the uncoupled basis formed by the product of the nuclear wave function and the electromagnetic field. The initial and final wavefunctions are thus $|i\rangle = |\alpha\rangle|0,0\rangle$ and $|f\rangle = |\beta\rangle|\mathbf{k}\mu\rangle$ where $|\alpha\rangle$ and $|\beta\rangle$

are the initial and final states of the nucleus. It is now possible to evaluate the matrix elements of Eq. A.2 corresponding to $\mathbf{k}$ and μ, $M_{\beta\alpha}(\mathbf{k}\mu)$, using Eq. A.6 to find

$$M_{\beta\alpha}(\mathbf{k}\mu) = -\frac{\mu\sqrt{2\pi}}{c}\sum_{l}\sqrt{2l+1}i^{l}\int d\mathbf{r}\langle\beta|\hat{\mathbf{j}}(\mathbf{r})|\alpha\rangle\cdot\left(\mathbf{A}_{l\mu}(\mathbf{r};M)+i\mu\mathbf{A}_{l\mu}(\mathbf{r};E)\right). \quad \text{(A.7)}$$

In order for the integral to evaluate to a nonzero value, the current density operator and the multipole field must couple together to zero angular momentum. This implies that transitions between states are only possible when the multipole field and the current density operator are tensors of the same rank. The multipole field is a spherical tensor of rank l, and therefore, $\tilde{\mathbf{j}}$ must then be a tensor of rank l. Given this fact, the Wigner-Eckhart theorem [28] states that the triangle relation,

$$|J_\alpha - l| \leq J_\beta \leq J_\alpha + l, \quad \text{(A.8)}$$

must be satisfied if the matrix element can be nonzero. Selection rules associated with parity can also be derived from Eq. A.7. To state the results simply, for given parities of π_α and π_β for the initial and final states, transitions involving the electric multipole fields must satisfy $\pi_\alpha\pi_\beta = (-1)^l$, whereas the magnetic transitions must satisfy $\pi_\alpha\pi_\beta = (-1)^{(l+1)}$.

Furthermore, the long-wavelength approximation can be applied for low energy transitions in nuclei. By definition, the long wavelength approximation is defined by $kR \ll 1$ or equivalently $E_\gamma \ll \hbar c/R$. The nuclear radius is roughly $R = (1.2fm)A^{1/3}$ and the constant $\hbar c = 197$ MeV fm such that the long-wavelength limit holds for

$E_\gamma \ll 164 MeV/A^{1/3}$. For the case of ^{238}U, this is satisfied for photons of energy much less than 26 MeV. In the long-wavelength approximation, estimates of the transition rates can be made. As is evident in Eq. A.7, this requires knowledge of the nuclear wavefunction before and after the absorption. It is nevertheless illustrative to understand the dependence of the transition rate without considering this matrix element.

The multipole fields in Eq. A.7 are composed of terms of the form

$$\mathbf{A}_{lm}(\mathbf{r}, \Pi) = b_l j_l(kr) \mathcal{Y}_{lm,l}, \tag{A.9}$$

where Π denotes the electric of magnetic nature of the transition, $j_l(kr)$ is a spherical bessel function, and $\mathcal{Y}_{lm,l}$ is a vector spherical harmonic. In the long-wavelength limit, the asymptotic form of the spherical bessel function,

$$\lim_{x \to 0} j_l(x) \to \frac{x^l}{(2l+1)!!}, \tag{A.10}$$

is justified. Further simplification is achieved through the invocation of Siegert's Theorem [72] that both simplifies the evaluation of the integral and justifies the substitution of the charge density for the current density [12]. Substitution of all these simplifications into Eq. A.7, subsequently into Eq. A.1, and then summing over all possible orientations of $\mathbf{k}$ yields [73],

$$T_{fi}(l; \Pi) = \frac{8\pi(l+1)}{l[(2l+1)!!]} \frac{k^{2l+1}}{\hbar} |\langle f | \hat{\Omega}_{l\mu}(\Pi) | i \rangle|^2, \tag{A.11}$$

where the matrix element contains the entire dependence of the nuclear wave functions.

Appendix B

Relevant Equations

B.1 Wigner d functions

The lowest order $d^j_{m,m'}(\theta)$ functions that contribute to the PFADs presented in Ch. 3 are:

$$\begin{aligned}
d^1_{1,0}(\theta) &= -\frac{1}{\sqrt{2}}\sin\theta \\
d^1_{1,\pm1}(\theta) &= \frac{1 \pm \cos\theta}{2} \\
d^2_{1,0}(\theta) &= -\sqrt{\frac{3}{2}}\sin\theta\cos\theta \\
d^2_{1,\pm1}(\theta) &= \left(\frac{1 \pm \cos\theta}{2}\right)(2\cos\theta \mp 1) \\
d^2_{2,0}(\theta) &= \frac{\sqrt{6}}{4}\sin^2\theta \\
d^2_{2,\pm1}(\theta) &= -\left(\frac{1 \pm \cos\theta}{2}\right)\sin\theta \\
d^2_{2,\pm2}(\theta) &= \left(\frac{1 \pm \cos\theta}{2}\right)^2
\end{aligned} \tag{B.1}$$

Any of the necessary d functions can be obtained from these using the following identities [74]

$$d^j_{m,m'} = (-1)^{m'-m} d^j_{m',m} = d^j_{-m',-m}. \tag{B.2}$$

Appendix C

Tabulation of Strip Angles

Table C.1: Table of angular positions sorted by detector position and relative strip number.

Detector Location	Strip	$\bar{\theta} \pm \sigma_\theta$ (deg)	$\bar{\phi} \pm \sigma_\phi$ (deg)
Upstream - Vertical	0	160.2 ± 18.9	76.6 ± 66.2
	1	159.6 ± 15.8	78.7 ± 64.3
	2	157.7 ± 16.2	80.7 ± 58.5
	3	156.2 ± 15.4	83.7 ± 53.6
	4	154.3 ± 14.6	85.3 ± 52.6
	5	152.2 ± 14.0	87.1 ± 49.4
	6	150.2 ± 13.4	89.5 ± 45.3
	7	147.7 ± 13.0	89.2 ± 45.1
	8	144.9 ± 12.7	90.9 ± 41.9
	9	142.1 ± 12.8	91.3 ± 40.5
	10	138.7 ± 12.9	93.0 ± 37.9
	11	135.6 ± 12.3	93.7 ± 34.7
	12	131.8 ± 12.4	94.3 ± 34.2
	13	128.0 ± 12.3	94.1 ± 32.4
	14	124.3 ± 12.3	93.5 ± 28.9
	15	120.2 ± 12.1	92.5 ± 25.2
Downstream - Horizontal	0	33.5 ± 13.9	-12.0 ± 35.4
	1	37.4 ± 13.4	-11.0 ± 33.7
	2	42.1 ± 13.6	-11.1 ± 31.1
	3	46.8 ± 13.5	-10.8 ± 30.0
	4	52.1 ± 13.8	-10.5 ± 28.5
	5	57.3 ± 13.8	-10.3 ± 27.7
	6	62.9 ± 13.9	-10.3 ± 26.8
	7	68.5 ± 13.7	-10.7 ± 26.1
	8	74.1 ± 13.5	-11.2 ± 25.4
	9	79.8 ± 13.2	-12.0 ± 24.7
	10	85.1 ± 12.9	-13.0 ± 24.1
	11	90.4 ± 12.5	-14.6 ± 23.4

	12	95.2 ± 12.1	-15.8 ± 22.9
	13	99.7 ± 11.8	-16.3 ± 22.4
	14	104.3 ± 11.4	-14.8 ± 20.2
	15	108.9 ± 11.0	-12.7 ± 18.5
Upstream - Horizontal	0	159.8 ± 20.1	178.8 ± 71.1
	1	159.5 ± 14.6	178.0 ± 66.7
	2	157.5 ± 15.1	178.4 ± 66.6
	3	156.2 ± 15.2	179.2 ± 64.3
	4	154.0 ± 15.3	177.5 ± 63.2
	5	152.2 ± 13.9	177.4 ± 61.7
	6	149.9 ± 13.1	175.4 ± 59.0
	7	147.2 ± 13.3	175.9 ± 56.7
	8	144.5 ± 12.5	177.5 ± 56.9
	9	141.6 ± 12.3	174.6 ± 52.8
	10	138.2 ± 12.3	173.8 ± 51.0
	11	134.9 ± 12.2	174.8 ± 50.5
	12	131.3 ± 11.7	172.8 ± 48.2
	13	127.5 ± 11.5	172.9 ± 46.7
	14	123.6 ± 12.0	173.6 ± 44.7
	15	119.4 ± 11.9	175.5 ± 40.4
Downstream - Vertical	0	35.2 ± 14.5	279.2 ± 37.4
	1	39.1 ± 13.7	278.4 ± 33.9
	2	43.5 ± 13.5	277.9 ± 32.2
	3	48.3 ± 13.8	277.9 ± 31.6
	4	53.3 ± 13.7	277.6 ± 29.0
	5	58.4 ± 13.7	277.6 ± 28.0
	6	63.7 ± 13.7	278.0 ± 27.4
	7	69.4 ± 13.6	278.4 ± 26.3
	8	75.0 ± 13.4	278.9 ± 25.9
	9	80.7 ± 12.8	280.2 ± 24.7
	10	86.0 ± 12.5	281.2 ± 23.9
	11	91.2 ± 12.2	283.2 ± 23.4
	12	95.9 ± 11.8	284.9 ± 22.2
	13	100.2 ± 11.5	285.8 ± 21.4
	14	104.8 ± 11.3	284.3 ± 19.5
	15	109.2 ± 11.1	281.8 ± 18.2

Appendix D

Geant4 Code

D.0.1 Stored Straggling Data

The straggling of the fission fragments through the target was the most important aspect of the GEANT4 simulation. While these particles were transported through the target material, specific information was stored for later use in the calculation of Λ functions. The information recorded for a fragment while traveling through the target is listed below:

- Initial trajectory as θ and ϕ
- Initial global position of fragment
- Position relative to target volume
- Displacement in target volume
- Initial momentum vector
- Change in momentum vector
- Initial kinetic energy
- Change in kinetic energy

- Total energy deposited in target
- Total non-ionizing energy deposited in target
- Name of the fragment, *i.e.*, the isotope
- Fragment mass
- Fragment charge
- Length of path traveled in the target
- Average path length traveled in the target

D.0.2 The Si Strip Detector Model

In any model, the accurate description of all components in an experimental geometry is requisite for agreement to be achieved with experimental data. Because there is no limit to the complexity of these geometries, care must be taken to simplify the model whenever possible without sacrificing quality. Doing so allows the modeler to work with simpler components that behave as one entity. One way to accomplish this is by forming composite objects. In the present project, the SSDs were excellent candidates for this technique.

GEANT4 is written in such a way that the details of detector geometry and functionality are decoupled to make use of the benefits of object-oriented software design. In reality, though, such a separation is unnatural because the geometry is inseparable from the functionality. For this reason, the SensitiveSSD class was written to couple

the two components together. It contains both SSDBuilder class object that defines the detector geometry and also an SSDSensitivity object that defines the functionality. The SSDBuilder groups all of the components of the detector so the user can place a detector as a whole entity without concern for the placement of the subcomponents that define it. The SSDSensitivity class builds SSDHit objects that store all of the information that is useful for understanding the interaction of the particles with the detector itself. This software alleviates much of the work that would be required to model future experiments involving these detectors. For that reason, the full code is included below with comments.

```
// SSDBuilder.hh
//
// Jeromy Tompkins
//
//

#include "globals.hh"
#include "G4String.hh"
#include "G4ThreeVector.hh"
#include <map>
#include <exception>

#ifndef SSDBUILDER_H
#define SSDBUILDER_H

class G4LogicalVolume;
class G4AssemblyVolume;
class G4VSensitiveDetector;
class G4Trap;
class G4SubtractionSolid;
class G4Material;
class G4PVPlacement;

class SSDBuilderException : public std::exception
{};
```

```
//! Assembles SSD components into G4AssemblyVolumes
/*!
 * A class that builds the Si Strip Detectors (SSD) utilized in
 * the Photofission Fragment Angular Distribution measurements.
 * It defines the geometry and also gives the user
 * the option of passing an G4VSensitiveDetector, i.e., the
 * detector's sensitivity, to the detector externally. Only
 * one of these can be set at a time and no attempt
 * is made by this class to own the various objects that
 * are passed to it. The GetADetector() function
 * returns a fully built detector as a G4AssemblyVolume that
 * is placeable using the G4AssemblyVolume::MakeImprint method.
 */
class SSDBuilder
{
public:
    //! Default constructor
    /*!
   * Initializes all of the member variables to NULL values.
   */
    SSDBuilder(void);
    //! Copy constructor
    /*!
   * @param obj is the address of the const SSDBuilder object to copy
   */
    SSDBuilder(SSDBuilder const& obj);
    //! Destructor
    /*!
   * This is an empty function that doesn't deallocate any
   * memory allocated by the class since I believe all of the
   * logical and physical volumes created on the heap are
   * owned by the mother volume, the ultimate being the root
   * volume.
   */
    ~SSDBuilder(void);
    //! Equals operator
    /*!
   * @param obj is the address of the const SSDBuilder object
   *        to make equal to
   * @return address of this object (ie. return *this;)
   */
    SSDBuilder& operator=(SSDBuilder const& obj);
```

```
    //! Normal method
    /*!
   * Allows the setting of a G4VSensitiveDetector to the silicon
   * logical volume ONLY. No history of arguments pass is kept
   * by this class. Calling this
   * method will cause the immediate assignment of the argument
   * to the silicon logical volume if the Assemble() function has
   * already been called. If not, it is stored until a later
   * call to Assemble() is made. The SSDSensitivity class is a
   * concrete class of G4VSensitiveDetector to be used with this
   * class.
   *
   * @param sens is a pointer to a G4VSensitiveDetector object
   */
    void  SetSensitivity(G4VSensitiveDetector *sens);

    //! Normal method
    /*!
   * Gets the currently assembled detector. The Assemble() method is
   * called if it has not been done previously. Otherwise, the
   * object pointed to by ssd_assembly is returned. @see Assemble()
   *
   * @return a pointer to the built SSD
   */
    G4AssemblyVolume* GetADetector(void);

    const G4ThreeVector GetSiOffset(void) const
    { return fsiOffset;};
    const G4ThreeVector GetDielectricOffset(void) const
    { return fDielectricOffset;};

    void     PrintGeometryInfo (void);

protected:
    //! A normal method
    /*!
   * Assembles the logical volumes for the Si ("silicon_log") and the
   * green dielectric board ("dielectricBoard_log") into a
   * G4AssemblyVolume whose address is stored by the ssd_assembly
   * pointer of this class.
   */
    void              Assemble (void);
```

```
    //! A normal method
    /*!
   * Defines the materials used in the SSD. These are G4_Si (Si),
   * G4_PLEXIGLASS (green dielectric board), and G4_Galactic.
   */
    void       DefineMaterials (void);
    void          BuildSilicon (void);
    void  BuildDielectricBoard (void);

private:
    // Maximum dimensions of the detector
    static const G4double        flongWidth;
    static const G4double       fshortWidth;
    static const G4double        fthickness;
    static const G4double           flength;
    static const G4double      fobtuseAngle;
    static const G4double       facuteAngle;

    static const G4double fdielectricBoardOffset_X;
    static const G4double fdielectricBoardOffset_Y;
    static const G4double fdielectricBoardOffset_Z;

    // Dimensions for the cutout in the green dielectric
    static const G4double     fcutoutLength;
    static const G4double  fcutoutLongWidth;
    static const G4double fcutoutShortWidth;
    static const G4double   fcutoutOffset_X;
    static const G4double   fcutoutOffset_Y;
    static const G4double   fcutoutOffset_Z;

    // Dimensions for construction and placement
    // of Si insert
    static const G4double   fsiliconThickness;
    static const G4double   fsiliconLongWidth;
    static const G4double   fsiliconShortWidth_0;
    static const G4double   fsiliconShortWidth_1;
    static const G4double   fsiliconLength_0;
    static const G4double   fsiliconLength_1;
    static const G4double   fbottomSiliconOffset;
    static const G4double   fsiliconOffset_X;
    static const G4double   fsiliconOffset_Y;
    static const G4double   fsiliconOffset_Z;
```

```
public:
    /*!
   * The strip_arc_center is computed as
   *       center_z = L_0/2 - a - L = -9.367 cm
   * where
   *       L   = SSDBuilder::flength = 9.27 cm
   *       L_0 = SSDBuilder::fsiliconLength_0 = 7.36 cm
   *       a   = 1.487 in = 3.777 cm
   *       d   = 0.250 in = 0.635 cm
   */
    static const G4ThreeVector     strip_arc_center;
    static const G4double   radius_first_strip_edge;
    static const G4double                strip_width;


private:
    G4ThreeVector     fsiOffset;
    G4ThreeVector     fDielectricOffset;

    std::map<G4String,G4Material*>     fmaterials;
    //!< Map of the materials used

    G4VSensitiveDetector     *fsensitivity;

    // Begin declarations of logical volumes
    G4LogicalVolume          *fsilicon_log;
    //!< Logical volume for Silicon backing

    G4LogicalVolume  *fdielectricBoard_log;
    //!< Logical volume for green dielectric board

    G4AssemblyVolume        *ssd_assembly;
    //!< Logical volume for the entire SSD

    // Begin declarations of physical solid
    G4Trap                       *fsilicon_solid;
    //!< Phys. solid for Silicon backing

    G4SubtractionSolid  *fdielectricBoard_solid;
    //!< Phys. solid for green dielectric board

    //  G4Trap                     *fssd_solid;
    //!< Phys. solid for the assembled detector
```

```
    // Begin declarations of physical volumes
    G4PVPlacement          *fsilicon_phys;
    //!< Phys. solid for Silicon backing

    G4PVPlacement  *fdielectricBoard_phys;
    //!< Phys. solid for green dielectric board

};
#endif

// SSDBuilder.cc
//
// Jeromy Tompkins
// 8/17/2011
//
//

#include <iostream>
#include <iomanip>
#include <map>
#include "globals.hh"
#include "G4String.hh"
#include "G4Material.hh"
#include "G4NistManager.hh"
#include "G4SubtractionSolid.hh"
#include "G4UnionSolid.hh"
#include "G4ThreeVector.hh"
#include "G4RotationMatrix.hh"
#include "G4Trap.hh"
#include "G4PVPlacement.hh"
#include "G4LogicalVolume.hh"
#include "G4AssemblyVolume.hh"
#include "G4VisAttributes.hh"
#include "SSDBuilder.hh"

const G4double SSDBuilder::flongWidth   =  11.59*cm;
const G4double SSDBuilder::fshortWidth  =   4.40*cm;
const G4double SSDBuilder::fthickness   =   0.24*cm;
const G4double SSDBuilder::flength      =   9.27*cm;
const G4double SSDBuilder::fobtuseAngle = 110.85*deg;
const G4double SSDBuilder::facuteAngle  =  69.15*deg;
```

```
const G4double SSDBuilder::fdielectricBoardOffset_X = -0.704*cm;
const G4double SSDBuilder::fdielectricBoardOffset_Y =  0.00*cm;
const G4double SSDBuilder::fdielectricBoardOffset_Z =  0.00*cm;

const G4double SSDBuilder::fcutoutLength      = 5.0*cm;
const G4double SSDBuilder::fcutoutLongWidth   = 5.0*cm;
const G4double SSDBuilder::fcutoutShortWidth  = 3.0*cm;

const G4double SSDBuilder::fcutoutOffset_X    = -1.41*cm;
const G4double SSDBuilder::fcutoutOffset_Y    =  0.43*cm;
const G4double SSDBuilder::fcutoutOffset_Z    =  0.00*cm;

const G4double SSDBuilder::fsiliconThickness     = 0.03*cm;
const G4double SSDBuilder::fsiliconLongWidth     = 8.26*cm;
const G4double SSDBuilder::fsiliconShortWidth_0  = 3.37*cm;
const G4double SSDBuilder::fsiliconShortWidth_1  = 4.60*cm;
const G4double SSDBuilder::fsiliconLength_0      = 6.37*cm;
const G4double SSDBuilder::fsiliconLength_1      = 2.18*cm;
const G4double SSDBuilder::fbottomSiliconOffset  = 0.659*cm;

const G4double SSDBuilder::fsiliconOffset_X = 0.00*cm;
const G4double SSDBuilder::fsiliconOffset_Y = fthickness/2.
                                            + fsiliconThickness/2.;
const G4double SSDBuilder::fsiliconOffset_Z
          = 0.5*(fsiliconLength_0-flength)+fbottomSiliconOffset;

const G4ThreeVector
SSDBuilder::strip_arc_center(0,
                        0,
                       -0.5*fsiliconLength_0
                          -fbottomSiliconOffset
                          -3.51*cm+fsiliconOffset_Z);

//const G4ThreeVector SSDBuilder::strip_arc_center(0,0,-6.324*cm);
const G4double SSDBuilder::radius_first_strip_edge = 5.387*cm;
const G4double SSDBuilder::strip_width             = 0.502*cm;

SSDBuilder::SSDBuilder()
    :
      fsiOffset(fsiliconOffset_X,
                fsiliconOffset_Y,
                fsiliconOffset_Z),
      fDielectricOffset(fdielectricBoardOffset_X,
```

```
          fdielectricBoardOffset_Y,
          fdielectricBoardOffset_Z),
      fmaterials(),
      fsensitivity(NULL),
      fsilicon_log(NULL),
      fdielectricBoard_log(NULL),
      ssd_assembly(NULL),
      fsilicon_solid(NULL),
      fdielectricBoard_solid(NULL),
      fsilicon_phys(NULL),
      fdielectricBoard_phys(NULL)
{
}

SSDBuilder::SSDBuilder(SSDBuilder const& obj)
    :
      fsiOffset(fsiliconOffset_X,
                fsiliconOffset_Y,
                fsiliconOffset_Z),
      fmaterials(obj.fmaterials),
      fsensitivity(obj.fsensitivity),
      fsilicon_log(obj.fsilicon_log),
      fdielectricBoard_log(obj.fdielectricBoard_log),
      ssd_assembly(obj.ssd_assembly),
      fsilicon_solid(obj.fsilicon_solid),
      fdielectricBoard_solid(obj.fdielectricBoard_solid),
      fsilicon_phys(obj.fsilicon_phys),
      fdielectricBoard_phys(obj.fdielectricBoard_phys)
{}

SSDBuilder::~SSDBuilder()
{}

SSDBuilder&
SSDBuilder::operator=(SSDBuilder const& obj)
{
    if (this!=&obj)
    {
        fsiOffset              = obj.fsiOffset;
        fmaterials             = obj.fmaterials;
        fsensitivity           = obj.fsensitivity;
        fsilicon_log           = obj.fsilicon_log;
        fsilicon_solid         = obj.fsilicon_solid;
```

```
        fdielectricBoard_log   = obj.fdielectricBoard_log;
        fdielectricBoard_solid = obj.fdielectricBoard_solid;
        ssd_assembly           = obj.ssd_assembly;
        fsilicon_phys          = obj.fsilicon_phys;
        fdielectricBoard_phys  = obj.fdielectricBoard_phys;
    }
    return *this;
}

void
SSDBuilder::SetSensitivity(G4VSensitiveDetector *sens)
{
    fsensitivity = sens;
    if (fsilicon_log!=NULL)
        fsilicon_log->SetSensitiveDetector(fsensitivity);
}

G4AssemblyVolume*
SSDBuilder::GetADetector()
{
    if (ssd_assembly==NULL)
        Assemble();

    return ssd_assembly;
}

void
SSDBuilder::Assemble ()
{
    DefineMaterials();
    BuildSilicon();
    BuildDielectricBoard();

    ssd_assembly = new G4AssemblyVolume;

    G4RotationMatrix rot;
    ssd_assembly->AddPlacedVolume(fdielectricBoard_log,
                                  fDielectricOffset,
                                  &rot);
    ssd_assembly->AddPlacedVolume(fsilicon_log,
                                  fsiOffset, &rot);
}
```

```
void
SSDBuilder::DefineMaterials(void)
{

    G4String name;
    G4Material* mat;

    G4NistManager *man = G4NistManager::Instance();

    mat = man->FindOrBuildMaterial("G4_Si");
    fmaterials[name="Si"] = mat;

    mat = man->FindOrBuildMaterial("G4_PLEXIGLASS");
    fmaterials[name="Plexi"] = mat;

    mat = man->FindOrBuildMaterial("G4_Galactic");
    fmaterials[name="Vacuum"] = mat;

}

void
SSDBuilder::BuildSilicon (void)
{
    G4VisAttributes attr(true);

    G4Trap *solid_0 = new G4Trap("solid_0",
                                 fsiliconLength_0/2.,
                                 0, 0,
                                 fsiliconThickness/2.,
                                 fsiliconShortWidth_0/2.,
                                 fsiliconShortWidth_0/2.,
                                 0,
                                 fsiliconThickness/2.,
                                 fsiliconLongWidth/2.,
                                 fsiliconLongWidth/2.,
                                 0);

    G4Trap *solid_1 = new G4Trap("solid_1",
                                 fsiliconLength_1/2.,
                                 0, 0,
                                 fsiliconThickness/2.,
                                 fsiliconLongWidth/2.,
                                 fsiliconLongWidth/2.,
```

```
                                0,
                                fsiliconThickness/2.,
                                fsiliconShortWidth_1/2.,
                                fsiliconShortWidth_1/2.,
                                0);

    G4RotationMatrix rot;
    G4ThreeVector v(0.,
                    0.,
                    fsiliconLength_0/2.+fsiliconLength_1/2.);

    G4UnionSolid *fsilicon_solid
              = new G4UnionSolid("silicon_solid",
                                 solid_0,
                                 solid_1,
                                 &rot,
                                 v);


    fsilicon_log   = new G4LogicalVolume(fsilicon_solid,
                                         fmaterials["Si"],
                                         "silicon_log");
    attr.SetColor(192.0/256.0, 192.0/256.0, 192.0/256.0);
    // silver
    //  attr.SetForceSolid(true);

    fsilicon_log->SetVisAttributes(attr);
    fsilicon_log->SetSensitiveDetector(fsensitivity);
}

void
SSDBuilder::BuildDielectricBoard (void)
{
    G4VisAttributes attr(true);
    attr.SetColor(0,1,0);   // green
    //  attr.SetForceSolid(true);

    G4Trap *wholeboard = new G4Trap("whole_board",
                                    flength/2.,
                                    0, 0,
                                    fthickness/2.,
                                    fshortWidth/2.,
                                    fshortWidth/2.,
```

```
                                    0,
                                    fthickness/2.,
                                    flongWidth/2.,
                                    flongWidth/2.,
                                    0);

    fdielectricBoard_log
              = new G4LogicalVolume(wholeboard,
                                    fmaterials["Plexi"],
                                    "dielectricBoard_log");
    fdielectricBoard_log->SetVisAttributes(attr);
}

void
SSDBuilder::PrintGeometryInfo(void)
{
    using std::setw;
    using std::right;
    using std::setprecision;

    std::cout << right << setw(6) << "Strip"
              << right << setw(12) << "Low Bound"
              << right << setw(12) << "Up Bound"
              << std::endl;
    std::cout << setw(30) << std::setfill('-') << '-' << std::endl;
    std::cout << std::setfill(' ');
    for (G4int i=0; i<16; i++)
    {
        std::cout << right << setw(6) << i
                  << right << setw(12) << setprecision(3)
                  << (radius_first_strip_edge+i*strip_width)/cm
                  << right << setw(12) << setprecision(3)
                  << (radius_first_strip_edge+(i+1)*strip_width)/cm
                  << std::endl;
    }

}

//// SSDSensitivity.h //////
#include "G4VSensitiveDetector.hh"
#include "SSDHit.hh"
#include "G4ThreeVector.hh"
```

```
#include <stdio.h>
#include <stdlib.h>
#include <iostream>

#ifndef SSDSENSITIVITY_H
#define SSDSENSITIVITY_H 1

class G4Step;
class G4HCofThisEvent;
class G4TouchableHistory;


//! Concrete implementation of G4VSensitiveDetector class for SSD
/*!
 * A class that concretely implements the G4SensitiveDetector class.
 * In essence, this provides the sensitivity of the logical volume
 * that defines the silicon detector itself (@see SSDBuilder). The
 * name passed into the constructor names the detector and will
 * also be used to name the SSDHitsCollection object that is
 * created by this object. In this way, the various detectors can
 * be differentiated from each other. In addition, an ID number is
 * assigned to the detector to be used for the same purpose.
 *
 * An important task that is completed by this class is the
 * determination of the Si strip that was hit, which is done by
 * geometrical considerations after coordinated transformation to
 * the local reference frame of the Si logical volume.
 *
 * This class also acts to filter out hits not located on the Si.
 * If it occurred outside of the Si volume then it is not stored as
 * an SSDHit.
 */
class SSDSensitivity : public G4VSensitiveDetector
{
public:
  //! Constructor
  /*!
   * Initializes all of the data members.
   * @param name is the name of the detector
   * @param detID is a numerical ID for the detector
   */
  SSDSensitivity(G4String name, G4int detID);
  //! Deconstructor
```

```
~SSDSensitivity();

//! Normal member function
/*!
 * Sets the center of the circle that defines the arcs
 * separating
 * the Si strips. This shouldn't need to be called because
 * the default center coordinates are set by the constructor.
 *
 * @param x is the x position
 * @param y is the y position
 * @param z is the z position
 */
void SetCenter(const G4double x,
               const G4double y,
               const G4double z);

//! Virtual member function
/*!
 * The SSDHitsCollection to be associated with this for
 * the entire simulation is generated and inserted into the
 * parameter's collection of collections.
 *
 * @param HCE is a pointer to a G4HCofThisEvent
 *                 ("G4 Hit Collection of This Event")
 */
virtual void   Initialize(G4HCofThisEvent* HCE);

//! Virtual member function
/*!
 * Computation of the strip number involved is done in
 * this function. Further the new SSDHit object is created
 * and stored inserted into the class's SSDHitCollection.
 *
 * @param aStep is the the current G4Step
 * @param ROHist is the G4TouchableHistory of the Readout
 *        Geometry (must be specified to be used)
 */
virtual G4bool ProcessHits(G4Step* aStep,
                           G4TouchableHistory* ROHist);

//! Virtual member function
/*!
```

```
   * An empty function that doesn't do anything.
   *
   * @param HCE is a pointer to a G4HCofThisEvent
   */
  virtual void   EndOfEvent(G4HCofThisEvent* HCE);

  //! Normal member function
  /*!
   * @return the detector name
   */
  G4String GetDetName(void) const {return fdetName;};

private:
  SSDHitsCollection *hitsCollection;
  //!< a pointer to the hit collection passed by the event

  G4int      fcollectionID;
  //!< the id number for hit collections produced by objects
       of this class

  const G4String        fdetName;

  G4int             fdetID;
  //!< the id number of the detector associated with this
  G4ThreeVector    fcenter;
  //!< the coordinate of the arc center describing strip boundaries
  G4bool              fhit;
  //!< a flag to filter out false hits
        (ie. no strip was hit --> no SSDHit object produced)
};
#endif

//// SSDSensitivity.cc
#include <iostream>
#include <iomanip>
#include <cmath>
#include "G4VSensitiveDetector.hh"
#include "SSDSensitivity.hh"
#include "SSDHit.hh"
#include "SSDBuilder.hh"

SSDSensitivity::SSDSensitivity(G4String detLocation, G4int detID)
    : G4VSensitiveDetector(detLocation),
```

```
      fcollectionID(detID),
      fdetName(detLocation),
      fdetID(detID),
      fcenter(SSDBuilder::strip_arc_center)
{
    G4String warnd;
    collectionName.insert(warnd=detLocation+"/SSDHitCollection");
}

SSDSensitivity::~SSDSensitivity(){;}

void
SSDSensitivity::SetCenter(const G4double x,
                          const G4double y,
                          const G4double z)
{
    fcenter.set(x,y,z);
}

void
PrintVComp(G4ThreeVector v1,
           G4ThreeVector v2,
           G4ThreeVector v3)
{
    using std::setw;
    using std::setprecision;
    std::cout << std::setiosflags(std::ios::fixed)
              << std::left
              << setprecision(1);
    std::cout << setw(8) << v1.x()
              << setw(8) << v1.y()
              << setw(8) << v1.z()
              << "|";
    std::cout << setw(8) << v2.x()
              << setw(8) << v2.y()
              << setw(8) << v2.z()
              << "|";
    std::cout << setw(8) << v3.x()
              << setw(8) << v3.y()
              << setw(8) << v3.z();
    std::cout << std::resetiosflags(std::ios::fixed)
              << std::right
              << setprecision(6)
```

```
              << std::endl;

}

G4bool
SSDSensitivity::ProcessHits(G4Step* aStep, G4TouchableHistory*)
{
    // Processes the hits for a given step and touchable history
    // Identifies the strip based on simple geometrical
    // considerations.
    G4double r=0.5;
    G4double theta=0;
    G4int    strip=-1;
    const G4TouchableHistory* theTouchable;

    G4StepPoint*  preStepPoint = aStep->GetPreStepPoint();
    theTouchable =
       static_cast<const G4TouchableHistory*>(
                                       preStepPoint->GetTouchable());
    G4ThreeVector worldPos = preStepPoint->GetPosition();
    G4ThreeVector localPos =
theTouchable->GetHistory()->GetTopTransform().TransformPoint(worldPos);
    G4ThreeVector offsetPos = localPos - fcenter;
    r = sqrt(offsetPos.z()*offsetPos.z() + offsetPos.x()*offsetPos.x());
    theta = atan(offsetPos.x()/offsetPos.z());

    fhit = true;
    G4double r_first_strip = SSDBuilder::radius_first_strip_edge;
    G4double strip_width   = SSDBuilder::strip_width;
    // if ((r/cm) > 4.718)
    if (r > r_first_strip && offsetPos.z()>0)
    {
        if ((r < r_first_strip+strip_width*13)
              && abs(theta) < 20.0*deg)
        {
            strip =
               static_cast<G4int>((r-r_first_strip)/strip_width);
        }
        else if ((r < r_first_strip+strip_width*14)
                    && abs(theta) < 17.555*deg)
        {
            strip = 13;
        }
```

```
        else if ((r < r_first_strip+strip_width*15)
                   && abs(theta) < 14.03*deg)
        {
            strip = 14;
        }
        else if ((r < r_first_strip+strip_width*16)
                   && abs(theta) < 9.14*deg)
        {
            strip = 15;
        }
        else
            fhit = false;
    }
    else
        fhit = false;

    if (fhit == true)
    {
        SSDHit*  newHit
            = new SSDHit(fdetName,aStep,fcollectionID,strip);
        newHit->SetLocalPos(localPos);
        hitsCollection->insert( newHit );
    }

#ifdef DEBUG_Sensitivity
    if ((hitsCollection->entries()-1)%20==0 && fhit && strip<2)
    {
        std::cout << "Processing hit " << hitsCollection->entries()
                  << std::endl;
        std::cout << "touchableVolume = "
                  << theTouchable->GetVolume()->GetName().data()
                  << std::endl;
      std::cout << "TopVolume = "
      << theTouchable->GetHistory()->GetTopVolume()->GetName().data()
                  << std::endl;
      std::cout << "world pos (cm) \n"
                << "x="
                << std::setprecision(3) << std::setw(8) << std::left
                << worldPos.getX()/cm
                << "y="
                << std::setprecision(3) << std::setw(8) << std::left
                << worldPos.getY()/cm
                << "z="
```

```
                << std::setprecision(3) << std::setw(8) << std::left
                << worldPos.getZ()/cm
                << std::endl;
        std::cout << "local pos (cm) \n"
                  << "x="
                << std::setprecision(3) << std::setw(8) << std::left
                << localPos.getX()/cm
                << "y="
                << std::setprecision(3) << std::setw(8) << std::left
                << localPos.getY()/cm
                << "z="
                << std::setprecision(3) << std::setw(8) << std::left
                << localPos.getZ()/cm
                << std::endl;
         std::cout << "offset pos (cm) \n"
                << "x="
                << std::setprecision(3) << std::setw(8) << std::left
                << offsetPos.getX()/cm
                << "y="
                << std::setprecision(3) << std::setw(8) << std::left
                << offsetPos.getY()/cm
                << "z="
                << std::setprecision(3) << std::setw(8) << std::left
                << offsetPos.getZ()/cm
                << std::endl;
         std::cout << "offset   = " << r_first_strip/cm << " cm"
                   << std::endl;
         std::cout << "Strip id = " << strip << std::endl;
    }
#endif


    return fhit;
}

void
SSDSensitivity::Initialize(G4HCofThisEvent* HCE)
{
    hitsCollection
        = new SSDHitsCollection(fdetName,
                                G4String() = fdetName+"collection");

    HCE->AddHitsCollection(fcollectionID,hitsCollection);
```

```
}

void
SSDSensitivity::EndOfEvent(G4HCofThisEvent*)
{
}

#include <algorithm>
#include "G4VHit.hh"
#include "G4ThreeVector.hh"
#include "G4THitsCollection.hh"
#include "G4VHitsCollection.hh"
#include "G4ThreeVector.hh"

#ifndef SSDHIT_H
#define SSDHIT_H

class G4Step;

//! A class to be used in debugging the initialization list
//! of SSDHit
class SSDDebugMsg
{
public:
  //! Constructor
  /*!
   * Prints the message that the SSDHit is being constructed
   * @param id is the detector id
   */
  SSDDebugMsg(G4int id)
  {
    std::cout << "Constructing SSDHit in det#" << id << std::endl;
  };
  //! Constructor
  /*!
   * Prints the message that the SSDHit is being constructed
   * @param name is the detector name
   */
  SSDDebugMsg(G4String name)
  {
    std::cout << "Constructing SSDHit in " << name.data()
              << std::endl;
  };
```

```
};

//! A class that stores the data generated by SSDSensitivity
/*!
 * This class is the concrete definition of the G4VHit class. It
 * is produced by SSDSensitivity objects when a step results in a
 * position located on one of the Si strips.
 */
class SSDHit : public G4VHit
{

public:
  //! Default constructor
  SSDHit(void);

  //! Constructor
  /*!
   * This constructor provides the ability to set the name to
   * any value
   * @param idetName is the name of the SSD associated with
           the SSDSensitivity creating this
   * @param aStep is the current G4Step that is used to get
           information from
   * @param idetector is the id of the SSD associated with the
           SSDSensitivity creating this
   * @param iSistrip is the strip number that was hit.
   */
  SSDHit(G4String idetname, G4Step *aStep,
         G4int idetector, G4int iSistrip);


  SSDHit(const SSDHit& obj);
  SSDHit& operator=(SSDHit obj);
  friend void swap(SSDHit& lhs, SSDHit& rhs);

  //! Deconstructor
  /*!
   * An empty function
   */
  ~SSDHit(void);
```

```
  SSDHit& operator+=(SSDHit& obj);

private:
  G4int                 fdetID;
  //!< Detector ID
  G4int               fsiStrip;
  //!< Strip ID
  G4double             feffPhi;
  //!< Angle phi
  G4double           feffTheta;
  //!< Angle theta
  G4ThreeVector      fworldPos;
  //!< Initial world position of particle
  G4ThreeVector fdeltaWorldPos;
  //!< Final world position particle
  G4ThreeVector      flocalPos;
  //!< Final local position particle
  G4ThreeVector  fmomentum;
  //!< Initial particle velocity
  G4ThreeVector fdeltaMomentum;
  //!< Final particle velocity
  G4double             finitKE;
  //!< Initial particle kinetic energy
  G4double            fdeltaKE;
  //!< Final particle kinetic energy
  G4double            ftotDepE;
  //!< Total deposited energy
  G4double    fnonIonizingDepE;
  //!< Total non-ionizing deposited energy
  G4String            fdetName;
  //!< A prestring for use in CSV output
  G4String       fparticleName;
  //!< Particle name
  G4double               fmass;
  //!< Mass of the particle
  G4double             fcharge;
  //!< Charge of the particle


  std::map<G4int, G4String> fdetLocationMap;
  //!< Maps the detectorID to the name

  //! Normal member function
```

```
  /*!
   * Sets up the internal map for identifying the
   * detectorID with the appropriate name
   */
  void SetupDetLocationMap(void);

public:
  void SetEffPhiTheta(G4double iphi,G4double ithe);
  void SetEffPhiTheta(G4Step *aStep);
  void SetDetName(G4String name);
  void SetLocalPos(const G4ThreeVector& avec);

  G4int    GetDetID(void) const {return fdetID;};
  G4int    GetStripID(void)    const {return fsiStrip; };
  //! Normal member function
  /*!
   * Returns the azimuthal angle in units of degrees
   */
  G4double GetPhi(void)      const {return feffPhi;};
  //! Normal member function
  /*!
   * Returns the polar angle in unis of degrees
   */
  G4double GetTheta(void) const
  {return feffTheta;   };

  G4ThreeVector GetWorldPos(void) const
  {return fworldPos;};

  G4ThreeVector GetDeltaPosition(void) const
  {return fdeltaWorldPos;};

  G4ThreeVector GetFinalLocalPos(void) const
  {return flocalPos;};

  G4ThreeVector GetMomentum(void) const
  {return fmomentum;};

  G4ThreeVector GetDeltaMomentum(void) const
  {return fdeltaMomentum;};

  G4double GetKineticEnergy(void) const
  {return finitKE;};
```

```
  G4double GetDeltaKineticEnergy(void) const
  {return fdeltaKE;      };

  G4double GetTotalEnergyDeposit(void) const
  {return ftotDepE;}

  G4double GetNonIonizingEnergyDeposit(void) const
  {return fnonIonizingDepE; }

  G4String GetParticleName(void) const
  {return fparticleName;};

  G4double GetMass(void) const
  {return fmass;};

  G4double GetCharge(void) const
  {return fcharge;};
};

inline void swap(SSDHit &lhs, SSDHit &rhs)
{
    using std::swap;
    swap(lhs.fdetID, rhs.fdetID);
    swap(lhs.fsiStrip, rhs.fsiStrip);
    swap(lhs.feffPhi, rhs.feffPhi);
    swap(lhs.feffTheta, rhs.feffTheta);
    swap(lhs.fworldPos, rhs.fworldPos);
    swap(lhs.fdeltaWorldPos, rhs.fdeltaWorldPos);
    swap(lhs.flocalPos, rhs.flocalPos);
    swap(lhs.fmomentum, rhs.fmomentum);
    swap(lhs.fdeltaMomentum, rhs.fdeltaMomentum);
    swap(lhs.finitKE, rhs.finitKE);
    swap(lhs.fdeltaKE, rhs.fdeltaKE);
    swap(lhs.ftotDepE, rhs.ftotDepE);
    swap(lhs.fnonIonizingDepE, rhs.fnonIonizingDepE);
    swap(lhs.fdetName, rhs.fdetName);
    swap(lhs.fparticleName, rhs.fparticleName);
    swap(lhs.fmass, rhs.fmass);
    swap(lhs.fcharge, rhs.fcharge);
}

typedef G4THitsCollection<SSDHit> SSDHitsCollection;
```

```
#endif

// SSDHit.cc
//
// Jeromy Tompkins
// 9/16/2011
//
// This class is the "package" that will be implemented
// for storing
// data by the SSDSensitivity class.
//

#include <cstring>
#include "G4Step.hh"
#include "G4Track.hh"
#include "G4ThreeVector.hh"
#include "SSDHit.hh"

SSDHit::SSDHit()
  : G4VHit(),
    fdetID(-1),
    fsiStrip(-1),
    feffPhi(0),
    feffTheta(0),
    fworldPos(),
    fdeltaWorldPos(),
    flocalPos(),
    fmomentum(),
    fdeltaMomentum(),
    finitKE(0),
    fdeltaKE(0),
    ftotDepE(0),
    fnonIonizingDepE(0),
    fdetName(""),
    fparticleName(""),
    fmass(0),
    fcharge(0),
    fdetLocationMap()
{
  SetupDetLocationMap();
  fdetName = fdetLocationMap[fdetID];
}
```

```
SSDHit::SSDHit(G4String detName, G4Step *aStep,
               G4int idetector, G4int iSistrip)
: G4VHit(),
fdetID(idetector),
fsiStrip(iSistrip),
feffPhi(0),
feffTheta(0),
fworldPos(aStep->GetPreStepPoint()->GetPosition()),
fdeltaWorldPos(aStep->GetDeltaPosition()),
flocalPos(),
fmomentum(aStep->GetPreStepPoint()->GetMomentum()),
fdeltaMomentum(aStep->GetPostStepPoint()->GetMomentum()-fmomentum),
finitKE(aStep->GetPreStepPoint()->GetKineticEnergy()),
fdeltaKE(aStep->GetPostStepPoint()->GetKineticEnergy() - finitKE),
ftotDepE(aStep->GetTotalEnergyDeposit()),
fnonIonizingDepE(aStep->GetNonIonizingEnergyDeposit()),
fdetName(detName),
fparticleName(aStep->GetTrack()/* delete this comment to use code
                  */->GetParticleDefinition()->GetParticleName()),
fmass(aStep->GetTrack()->GetParticleDefinition()->GetPDGMass()),
fcharge(aStep->GetTrack()->GetDynamicParticle()->GetCharge()),
fdetLocationMap()
{
  SetupDetLocationMap();
  SetEffPhiTheta(aStep);
}

SSDHit::SSDHit(const SSDHit& obj)
    : G4VHit(obj),
    fdetID(obj.fdetID),
    fsiStrip(obj.fsiStrip),
    feffPhi(obj.feffPhi),
    feffTheta(obj.feffTheta),
    fworldPos(obj.fworldPos),
    fdeltaWorldPos(obj.fdeltaWorldPos),
    flocalPos(obj.flocalPos),
    fmomentum(obj.fmomentum),
    fdeltaMomentum(obj.fdeltaMomentum),
    finitKE(obj.finitKE),
    fdeltaKE(obj.fdeltaKE),
    ftotDepE(obj.ftotDepE),
    fnonIonizingDepE(obj.fnonIonizingDepE),
    fdetName(obj.fdetName),
```

```
    fparticleName(obj.fparticleName),
    fmass(obj.fmass),
    fcharge(obj.fcharge),
    fdetLocationMap(obj.fdetLocationMap)
{
}

SSDHit& SSDHit::operator=(SSDHit obj)
{
    swap(*this, obj);
    return *this;
}

SSDHit::~SSDHit(){;}

SSDHit& SSDHit::operator+=(SSDHit& obj)
{
   // sum up the summable objects...
   fdeltaKE += obj.GetDeltaKineticEnergy();
   ftotDepE += obj.GetTotalEnergyDeposit();
   fnonIonizingDepE += obj.GetNonIonizingEnergyDeposit();

   fdeltaWorldPos += obj.GetDeltaPosition();
   fdeltaMomentum += obj.GetDeltaMomentum();

   return *this;
}

void
SSDHit::SetupDetLocationMap(void)
{
  fdetLocationMap[0] = "UpStreamTop";
  fdetLocationMap[1] = "DownStreamLeft";
  fdetLocationMap[2] = "UpStreamRight";
  fdetLocationMap[3] = "DownStreamBottom";
}


void
SSDHit::SetDetName(G4String name)
{
  fdetName = name;
}
```

```
void
SSDHit::SetEffPhiTheta(G4double iphi,G4double ithe)
{
  feffPhi = iphi;
  feffTheta = ithe;
}

void
SSDHit::SetEffPhiTheta(G4Step *aStep)
{
  G4ThreeVector vec =
       aStep->GetTrack()->GetVertexPosition();

  G4ThreeVector finalWorldPos = fworldPos + fdeltaWorldPos;
  // theta() returns atan2(perp(),dz)
  // perp() is sqrt(dx*dx+dy*dy)
  // and dz is the z component. This is the proper
  // definition of the polar angle
  feffTheta = (finalWorldPos - vec).theta();
  // Phi = atan2(dy,dx) where dx and dy are the components
  // this is the proper definition of the azimuthal angle
  feffPhi   = (finalWorldPos - vec).phi();
}

void
SSDHit::SetLocalPos(const G4ThreeVector& avec)
{
  flocalPos = avec;
}

// SensitiveSSD
// SensitiveSSD.hh
//
// Jeromy Tompkins
// 9/20/2011
//
// A class that constructs an SSD with an associated
// SSDSensitivity object.

#include "SSDBuilder.hh"
#include "SSDSensitivity.hh"
```

```
#ifndef SENSITIVESSD_HH
#define SENSITIVESSD_HH 1

//! A class that combines the functionality of the Sensitive
//! Detector and the geometry
/*!
 * This class groups together the SSDBuilder functionality and its
 * sensitivity, encapsulated in SSDSensitivity.
 *
 */
class SensitiveSSD
{

public:
  //! Constructor
  /*!
   * Constructs the SSDBuilder on the stack and
   * the SSDSensitivity on the heap. Following construction
   * the SSDSensitivity is passed to the SSDBuilder via the
   * SSDBuilder::SetSensitivity() method.
   *
   * @param name is the name of the SSDSensitivity object
   *        (the sensitive detector)
   * @param detID is the id number to be associated with the
   *        SSDSensitivity object
   */
  SensitiveSSD(const G4String name, const G4int detID);

  //! Deconstructor
  /*!
   * The SSDSensitivity object originally constructed by this class
   * is not deleted because it is eventually deleted by the SDManager
   */
  ~SensitiveSSD(void);

  //! Normal member function
  /*!
   * @return the builder object
   */
  SSDBuilder        GetBuilder(void)  const {return ftheBuilder;};
  //! Normal member function
  /*!
```

```
   * @return a point to the SSDSensitivity object created
   *         by this class
   */
  SSDSensitivity*   GetSensitivity(void) const
  {return ftheSensitivity;};

  //! Normal member function
  /*!
   * A convenience function that calls SSDBuilder::GetADetector()
   */
  G4AssemblyVolume* GetADetector(void);

private:
  SSDBuilder            ftheBuilder;
  SSDSensitivity   *ftheSensitivity;

};

#endif


#include <iostream>
#include "SSDBuilder.hh"
#include "SSDSensitivity.hh"
#include "SensitiveSSD.hh"

SensitiveSSD::SensitiveSSD(const G4String name,
       const G4int detID)
  : ftheBuilder(),
    ftheSensitivity(new SSDSensitivity(name,detID))
{
  ftheBuilder.SetSensitivity(ftheSensitivity);
  std::cout << "Instance of SensitiveSSD constructed : "
  << name.data() << std::endl;
}

SensitiveSSD::~SensitiveSSD()
{
  // Do not delete the sensitivity b/c it is owned by
  // the SDManager!!
  //  delete ftheSensitivity;
  std::cout << "Instance of SensitiveSSD destructed : "
  << ftheSensitivity->GetDetName().data() << std::endl;
```

```
}

G4AssemblyVolume*
SensitiveSSD::GetADetector(void)
{
  return ftheBuilder.GetADetector();
}
```

Bibliography

[1] J.M. Mueller, M.W. Ahmed, B. Davis, J.M. Hall, S.S. Henshaw, M.S. Johnson, H.J. Karwowski, D. Markoff, L.S. Myers, B.A. Perdue, S. Stave, J.R. Tompkins, M.J. Tuffley, and H.R. Weller. *Phys. Rev. C*, 85:014605, 2012.

[2] H. Goutte, J. F. Berger, P. Casoli, and D. Gogny. *Phys. Rev. C*, 71:024316, 2005.

[3] *Scientific Grand Challenges: Forefront Questions in Nuclear Science and the Role of Computing at the Extreme Scale*, 2009. D.O.E. Office of Nuclear Physics.

[4] E. Fermi. *Nature(London)*, 133:898, 1934.

[5] E. Fermi, E. Amaldi, B. Pontecorvo, F. Rasetti, and E. Segré. *Ricerca Scientifica*, 5:282, 1934.

[6] L.A. Turner. *Rev. Mod. Phys.*, 12:1, 1940.

[7] O. Hahn and F. Strassman. *Naturwiss.*, 27:89, 1939.

[8] L. Meitner and O.R. Frisch. *Nature(London)*, 143:239, 1939.

[9] O.R. Frisch. *Nature(London)*, 143:276, 1939.

[10] N. Bohr and J.A. Wheeler. *Phys. Rev.*, 56:426, 1939.

[11] A. Göök, M. Chernykh, C. Eckardt, J. Enders, P. von Neumann-Cosel, A. Oberstedt, S. Oberstedt, and A. Richter. *Nucl. Phys. A*, 851:1, 2011.

[12] W. Greiner and J.A. Maruhn. *Nuclear Models*. Springer, New York, 1996.

[13] K.S. Krane. *Introductory Nuclear Physics*. John Wiley and Sons, 1988.

[14] V.M. Strutinsky. *Nucl. Phys. A*, 95:420, 1967.

[15] C.F.v. Weizsacker. *Z. Phys.*, 96:431, 1935.

[16] H.A. Bethe and R.F. Bacher. *Rev. Mod. Phys.*, 8:82, 1936.

[17] H.J. Krappe and K. Pomorski. *Theory of Nuclear Fission*, volume 838. 2012.

[18] S. Cwiok, W. Nazarewicz, J.X. Saladin, W. Plociennik, and A. Johnson. *Phys. Lett. B*, 322:304, 1994.

[19] K. Pomorski and J. Dudek. *Phys. Rev. C*, 67:044316, 2003.

[20] C. Gustafsson, P. Möller, and S.G. Nilsson. *Phys. Lett. B*, 34:349, 1971.

[21] V. Metag, D. Habs, and H.J. Specht. *Phys. Rep.*, 65:1, 1980.

[22] P. Fong. *Phys. Rev.*, 135:B1338, 1964.

[23] S.G. Kadmensky. *Phys. of Atom. Nucl.*, 68:1968, 2005.

[24] E.J. Winhold, P.T. Demos, , and I. Halpern. *Phys. Rev.*, 87:1139, 1952.

[25] M. Goldhaber and E. Teller. *Phys. Rev.*, 74:1046, 1948.

[26] A. Bohr. *Proc. U.N. Int. Conf. Peaceful Uses At. Energy*, 2:151, 1956.

[27] S.G. Kadmensky and L.V. Titova. *Bull. Russ. Acad. Sci.: Phys.*, 72:324, 2008.

[28] J. J. Sakurai. *Modern Quantum Mechanics (Revised Edition).* Addison-Wesley Publishing Co., New York, 1994.

[29] V. Bellini, M. Di Toro, S. Lo Nigro, and G.S. Pappalardlo. *Lett. al Nuovo Cimento*, 26:173, 1979.

[30] R. Ratzek, W. Wilke, J. Drexler, R. Fischer, R. Heil, K. Huber, U. Kneissl, H. Ries, H. Ströher, R. Stock, and K. Wienhard. *Z. Phys. A*, 308:63, 1982.

[31] S.G. Kadmensky. *Phys. of Atom. Nucl.*, 65:1390, 2002.

[32] S.G. Kadmensky and L.V. Rodionova. *Phys. of Atom. Nucl.*, 66:1219, 2003.

[33] A.V. Ignatyuk, N.S. Rabotnov, G.N. Smirenkin, A.S. Soldatov, and Yu. M. Tsipenyuk. *Sov. Phys. JETP*, 61:684, 1971.

[34] A. Krasznahorkay. *Handbook of Nucl. Chem.*, volume 1. Springer US, 2 edition, 2011.

[35] Y.B. Ostapenko, G.N. Smirenkin, and A.S. Soldatov. *Sov. J. Part. Nucl.*, 12:6, 1981.

[36] E.J. Winhood and I. Halpern. *Phys. Rev.*, 103:990, 1956.

[37] *Second U.N. Intern. Conf. on the Peaceful Uses of Atomic Energy*, Geneva, 1958. United Nations.

[38] *Second U.N. Intern. Conf. on the Peaceful Uses of Atomic Energy*, Geneva, 1958. United Nations.

[39] A. P. Baerg, R. M. Bartholomew, F. Brown, L. Katz, , and S. B. Kowalski. *Can. Journ. Phys.*, 37:1418, 1959.

[40] B. Forkman and S.A.E. Johansson. *Nucl. Phys.*, 20:136, 1960.

[41] H.G. de Carvalho, A.G. da Silva, and J. Goldemberg. *Il Nuovo Cimento*, 19:1131, 1961.

[42] A.S. Soldatov, G.N. Smirenkin, S.P. Kapitza, and Y.M Tsipeniuk. *Phys. Lett.*, 14: 217, 1965.

[43] N.S. Rabotnov, G.N. Smirenkin, A.S. Soldatov, L.N. Usachev, S.P. Kapitza, and Yu.M. Tsipenyuk. *Sov. Journ. Nucl. Phys.*, 11:285, 1970.

[44] A. Mandredini, L. Fiore, C. Ramorino, H.G. de Carvalho, , and W. Wolfi. *Nucl. Phys. A*, 123:664, 1969.

[45] E.J. Dowdy and T.L. Krysinski. *Nucl. Phys. A*, 175:501, 1971.

[46] S. Nair, D.B. Gayther, B.H. Patrick, and E.M. Bowey. *J. Phys. G*, 3:965, 1977.

[47] L.J. Lindgren, A. Alm, and A. Sandell. *Nucl. Phys. A*, 298:43, 1978.

[48] V. E. Rudnikov, G. N. Smirenkin, A. S. Soldatov, and S. Juhasz. *Sov. Journ. Nucl. Phys.*, 48:414, 1988.

[49] F. Steiper, Th. Frommhold, W. Henkel, A. Jung, U. Kneissl, and R. Stock. *Nucl. Phys. A*, 563:252, 1993.

[50] V.M. Khvastunov, V.V. Denyak, I.G. Evseev, L.M. Zavada, V.I. Kasilov, N.I. Lapin, V.P. Likhachev, S.A. Pashchuk, V.M. Sanin, and S.F. Shcherbak. *Phys. Atom. Nucl.*, 57:1858, 1994.

[51] V.M. Khvastunov and V.V. Denyak. *Phys. of Atom. Nucl.*, 64:1269, 2001.

[52] R. Vandenbosch and J.R. Huizenga. *Nuclear Fission*. Academic Press, New York, 1973.

[53] R.A. Schmitt and R.B. Duffield. *Phys. Rev.*, 105:1277, 1957.

[54] A.W. Fairhall, I. Halpern, and E.J. Winhold. *Phys. Rev.*, 94:733, 1954.

[55] J.J. Griffin. *Phys. Rev.*, 116:107, 1959.

[56] D.L. Hill and J.A. Wheeler. *Phys. Rev.*, 89:1102, 1953.

[57] R. Vandenbosch. *Phys. Lett. B*, 45:207, 1973.

[58] W.A. Watson III, J. Chen, G. Heyes, E. Jastrzembski, and D. Quarrie. A scalable data acquisition system for cebaf: architecture and status. *Conf. Record of IEEE Nucl. Sci. Symp. and Med. Imaging Conf.*, 1:543, 1992.

[59] S. Anilkumar, A. K. Deepa, K. Narayani, A. K. Rekha, P. V. Achuthan, G. Krishnamachari, and D. N. Sharma. *Journal of Radioanalytical and Nuclear Chemistry*, 274:161–166, 2007.

[60] A.H. Wuosmaa, P. Wilt, B.B. Back, R.R. Betts, M. Freer, B.G. Glagola, Th. Happ, D.J. Henderson, I.G. Bearden, R.W. Zurmühle, D.P. Balamuth, S. Barrow, D. Benton, Q. Li, Z. Liu, , and Y. Miao. *Nucl. Instr. Meth. in Phys. Res. A*, 345: 482, 1994.

[61] M.A. Howe, G.A. Cox, P.J. Harvey, F. McGirt, K. Rielage, J.F. Wilkerson, and J.M. Wouters. *IEEE Trans. Nucl. Sci.*, 51:878, 2004.

[62] S. Agostinelli et al. *Nucl. Instr. Meth. in Phys. Res. A*, 506:250, 2003.

[63] Intl. Comm. on Rad. Units and Meas. *Journal of the ICRU*, 5:1, 2005.

[64] M. Piessens, E. Jacobs, S. Pommé, and D. De Frenne. *Nucl. Phys. A*, 556:88, 1993.

[65] J. Randrup and R. Vogt. *arXiv*, 0906.1250v1:1, 2009.

[66] I. Antcheva et al. *Comp. Phys. Comm.*, 180:2499, 2009.

[67] J.F. Ziegler. *Nucl. Instr. Meth. in Phys. Res. B*, 219-220:1027, 2004.

[68] L. Csige, M. Csatlós, T. Faestermann, Z. Gácsi, J. Gulyás, D. Habs, R. Hertenberger, A. Krasznahorkay, R. Lutter, H.J. Maier, P.G. Thirolf, and H.-F. Wirth. *Phys. Rev. C*, 80:011301, 2009.

[69] A. Krasznahorkay, D. Habs, M. Hunyadi, D. Gassmann, M. Csatlós, Y. Eisermann, T. Faestermann, G. Graw, J. Gulyás, R. Hertenberger, H.J. Maier, Z. Máté, A. Metz, J. Ott, P. Thirolf, and S.Y. van der Werf. *Phys. Lett. B*, 461:15, 1999.

[70] M. Csatlós, A. Krasznahorkay, P.G. Thirolf, D. Habs, Y. Eisermann, T. Faestermann, G. Graw, J. Gulyás, M.N. Harakeh, R. Hertenberger, M. Hunyadi, H.J. Maier, Z. Máté, O. Schaile, and H.-F. Wirth. *Phys. Lett. B*, 615:175, 2005.

[71] M. Hunyadi, D. Gassmann, A. Krasznahorkay, D. Habs, P.G. Thirolf, M. Csatlós, Y. Eisermann, T. Faestermann, G. Graw, J. Gulyás, R. Hertenberger, H.J. Maier, Z. Máté, A. Metz, and M.J. Chromik. *Phys. Lett. B*, 505:27, 2001.

[72] A.J.F. Siegert. *Phys. Rev.*, 52:787, 1937.

[73] P. Ring and P. Schuck, editors. *The Nuclear Many-Body Problem*. Springer-Verlag, New York, 1980.

[74] V. Devanathan. *Angular Momentum Techniques in Quantum Mechanics*. Kluwer Academic Publishers, Boston, 1999.